Physical modelling and validation of a mono-tube hydraulic shock absorber

J. de Blok

D&C 2016.053

Master's thesis

Coach(es):   dr.ir. I.J.M. Besselink [a]
               H.D. Fischer [b]
               drs. A. Meijs [b]

Supervisor: prof.dr. H. Nijmeijer [a]

[a] Eindhoven University of Technology
   Department of Mechanical Engineering
   Dynamics & Control

[b] TFX Suspension Technology
   Weert, The Netherlands

Eindhoven, September, 2016

Abstract

Shock absorber manufacturer TFX Suspension Technology wants to predict and analyse shock absorber characteristics with the help of computer models. A mono-tube emulsion damper that fits a BMW R1200 GS motorcycle is used as a baseline for testing and for the development of the physical damper model. The aim is to accurately measure and model damping characteristics in terms of force as a function of damper excitation and other factors having an influence. This is done using the hydraulically actuated shock absorber test rig, developed by the Dynamics and Control group of the Eindhoven University of Technology.

The simulation model that is developed in this study assumes incompressible flow of oil through the valves, but assumes compressible oil in each container. Mechanical friction forces are assumed to be negligible. Most model parameters, such as geometries and properties of the oil, follow from data provided by TFX Suspension Technology. Four flow resistance coefficients that relate flow of oil to pressure losses are obtained from a least-squares parameter optimization algorithm. This algorithm minimizes the error between measurements and model results. The flow resistance coefficients are related to viscous and component friction of the corresponding orifices.

The model is capable of predicting damping forces within 7% accuracy for excitation frequencies in excess of 0.5 Hz. Friction forces dominate damping forces below this frequency, neglecting mechanical friction therefore yields larger prediction errors below 0.5 Hz.

The user-friendliness of the shockabsorber test rig has been enhanced by implementing a Graphical User Interface, additionally making it possible to built-in some automatic safety measures to prevent the operator from injuries. Operation- and safety procedures relating to rig operation are documented. Furthermore, an approach to reduce high-frequent measurement noise from measurement data is presented and validated by means of a low-pass Butterworth filter in combination with a time-domain averaging method.

The damper model that has been developed in this study has been compared in a simulation environment to a linear- and look-up table damper model. A half motorbike model is derived to predict the vertical dynamic behaviour of the BMW motorcycle. Performance assessment criteria are: tire compression, suspension travel and ISO 2631-1 sprung accelerations. The simulation results show that the newly developed physical damper model tends to show less suspension travel, RMS tire compression and RMS weighted sprung acceleration in comparison to linear- and look-up table damper models. Furthermore, simulations results with the new damper model show up to 13% less weighted sprung accelerations in comparison to the conventional look-up table damper model, demonstrating that implementation of a physical damper model is essential when predicting comfort levels.

i

Samenvatting

Schokdemperfabrikant TFX Suspension Technology is geïnteresseerd in het voorspellen en analyseren van schokdemperkarakteristieken met behulp van computer modellen. Een monotube emulsie demper voor een BMW R1200 GS motorfiets wordt gebruikt als basis voor het testen en ontwikkelen van een fysisch dempermodel. Het doel van dit onderzoek is om de dempingskarakteristiek van de schokdemper accuraat te meten en te voorspellen, in termen van dempingskracht als functie van demper excitatie en andere factoren die een invloed hebben op de dempingskarakteristiek. Hierbij wordt gebruik gemaakt van de hydraulisch geactueerde schokdemper testbank, ontwikkeld door de Dynamics and Control group binnen de Technische Universiteit Eindhoven.

Het simulatiemodel dat is ontwikkeld tijdens dit onderzoek veronderstelt een incompressibele oliestroming door de kleppen in de demper, maar veronderstelt compressibele olie in de kamers. Mechanische wrijving wordt verwaarloosd. De geometrie van de demper en de specificaties van de olie worden verstrekt door TFX Suspension Technology. Vier stromingsweerstandcoëfficiënten die de drukverliezen aan de stroming van olie relateren zijn verkregen door het toepassen van een kleinste-kwadraten optimalisatiealgoritme. Dit algoritme minimaliseert de fout tussen voorspellingen en metingen aan de demper. De stromingsweerstandcoëfficiënten zijn afhankelijk van viskeuze en component wrijvingen van de bijbehorende kanalen.

Het simulatiemodel is in staat om dempingskrachten met een nauwkeurigheid van 7% te voorspellen voor excitaties boven 0.5 Hz. Mechanische wrijving lijkt de dempingskracht te domineren voor excitaties lager dan 0.5 Hz, het verwaarlozen van wrijving resulteert hierdoor in een lagere nauwkeurigheid van het model.

De gebruiksvriendelijkheid van de testbank is verbeterd door implementatie van een gebruikersinterface. Deze interface maakt het mogelijk om gebruiksveiligheid maatregelen te implementeren. Veiligheids- en bedieningsprocedures van de testbank zijn gedocumenteerd. Een Butterworth laag-doorlaat filter wordt beschreven om meetruis te reduceren. Tijdsdomeinmiddeling van de metingen onderdrukt meetruis die niet door het Butterworth filter word weggefilterd.

Simulaties met het dempermodel worden vergeleken met een lineair model en look-up table demper model. Een zogenaamd half motorfiets model is afgeleid om de verticale dynamica van een motorfiets te beschrijven. De beoordelingscriteria om de drie modellen te vergelijken zijn: bandindrukking, verticale acceleratie en veerweg. Simulaties met het fysische demper model voorspellen minder veerweg, bandindrukking en verticale acceleraties ten opzichte van de lineaire en look-up table demper modellen. Verder tonen de simulaties dat het fysische model een 13% lagere ISO 2631-1 gefilterde verticale acceleratie voorspelt ten opzichte van het conventioneel gebruikte look-up table demper model. Dit demonstreert dat de implementatie van het fysische demper model essentieel is wanneer voorspellingen gedaan worden die betrekking hebben op comfort niveaus.

Acknowledgements

Nomenclature

List of symbols

Symbol	Description	Unit
a	Orifice cross-sectional area	[m^2]
A	Cross-sectional area	[m^2]
β	Bulk modulus	[Pa]
d_s	Damping constant	[Ns/m]
D	Diameter	[m]
ζ	Flow resistance coefficient	[$-$]
f	Darcy friction factor	[$-$]
f_{co}	Cut-off frequency	[Hz]
f_m	Mass fraction	[$-$]
F	Force	[N]
g	Gravitational constant acceleration	[m/s^2]
h	Stepsize	[s]
k_s	Suspension spring stiffness	[N/m]
k_t	Vertical tire spring stiffness	[N/m]
κ	Polytropic coefficient	[$-$]
l	Suspension length	[m]
L	Length	[m]
m	Mass	[kg]
m_s	Sprung mass	[kg]
m_u	Unsprung mass	[kg]
μ	Dynamic viscosity	[Ns/m^2]
N_{avg}	Amount of cycle averages	[$-$]
p	Pressure	[Pa]
Q	Volumetric flow	[m^3/s]
ρ	Density	[kg/m^3]
S	Stroke	[m]
t	Time	[s]
$\bar{v}$	Flow velocity	[m/s]
V	Volume	[m^3]
x	Damper rod position	[m]

Symbol	Description	SI Unit
x_r	Road position	[m]
y	Shim tip deflection	[m]
z_r	Road vertical displacement	[m]
z_s	Sprung mass vertical displacement	[m]
z_u	Unsprung mass vertical displacement	[m]
Re	Reynolds number	$[-]$

Contents

Chapter 1

Introduction

Vehicle dynamics, a specific field within automotive research, studies the motion of vehicles for different driving conditions. Aspects that play an important role in this field are ride comfort, vehicle stability and vehicle handling. The characteristics of suspension components, such as dampers, springs and shock absorbers, are known to influence all three of these aspects. Continued research is conducted to optimize these components. The process of component optimization has formerly been done by test engineers that subjectively rated the performance of a vehicle on a track. Nowadays, this process is supported by test rigs to qualitatively measure the performance of the suspension components.

1.1 Project background

Using available components from a former hydraulics lab, a hydraulically actuated shock absorber test rig has been created. Student Nick Feijen [1] has developed the control laws and did the first successful tests on a shock absorber. Whereas regular electro-mechanical actuated test rigs only allow sinusoidal tests, the hydraulically actuated TU/e test rig allows flexible control of the hydraulic actuator. This implies the possibility to excite a shock absorber with all sorts of signals. Although some first tests with the hydraulic test rig have shown promising results, it still lacks user-friendliness and clarity of the operation- and safety procedures, hence it should be made suitable for production work.

TFX Suspension Technology [2] is a small high-end shock absorber manufacturer. Examples of some of their products are displayed in Figure 1.1. To distinguish themselves from competition and speed up the development process, TFX Suspension Technology is interested in analysing shock absorber characteristics with the help of a predictive computer model. Predicting and analysing shock absorber characteristics before manufacturing minimizes the number of prototypes, hereby reducing the overall production costs. The demand for a computer model capable of predicting damping characteristics based on the geometries and physics of a shock absorber marks the start of a collaboration between the Vehicle Dynamics group of Eindhoven University of Technology and TFX Suspension Technology.

1.2 Aim and objectives

This study advances the development of the TU/e hydraulic shock absorber test rig and marks the start of physical modelling a hydraulic shock absorber. *The aim is to accurately measure*

(a)   (b)
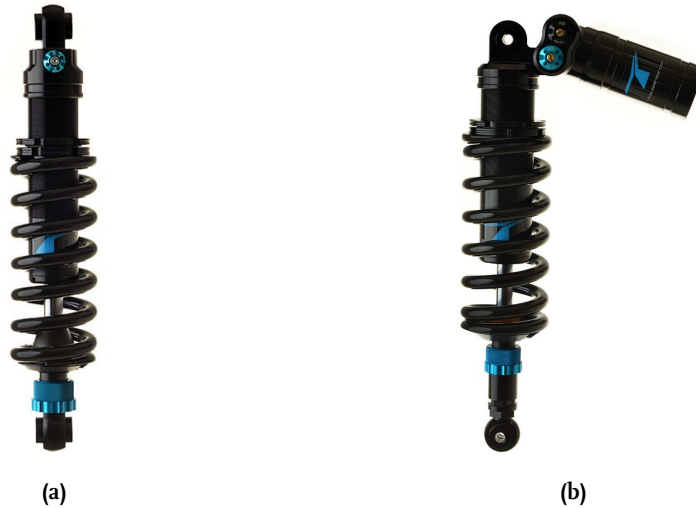
Figure 1.1: TFX Suspension Technology's mono-tube shock absorber (left) and dual-tube shock absorber (right)

and model the damping characteristics in terms of force as function of the damper velocity and other factors that have an influence. To do so, the following objectives have to be fulfilled:

- Improve the TU/e shock absorber test rig by making it more suitable for 'production' work. This implies improvements with respect to user-friendliness of the control software, definition of a measurement protocol and clarity of operating- and safety procedures.

- Review the state of art in shock absorber modelling, in which both 'black box' empirical models as well as physical models will be reviewed.

- Given the damper's geometries, develop a simulation model capable of calculating the force response as a result of damper excitation.

As this study aims to develop a physical damper model capable of calculating damping force as function of damper excitation, an additional objective can be defined:

- Examine by means of simulations the benefits of a physical damper model in comparison to existing models, such as look-up tables or linear dampers.

The rear damper of a BMW R1200 motorcycle, which will be used by TU/e's STORM electric motorcycle team [3], will be used as a baseline for testing and modelling the damping characteristics.

1.3   Outline of the thesis

Chapter 2 reviews the state of art in predicting and measuring shock absorber damping characteristics by means of a literature study. This literature study will be used as a starting point for physical damper model development.

Chapter 3 discusses the TU/e shock absorber test rig and proposes improvements to the test rig. It starts with an introduction to the TU/e test rig and continuous with improvements to user-friendliness of the control software and definition of operating- and safety procedures. A strategy to reduce measurement noise is proposed as well.

Having a fully operational test rig as discussed in Chapter 3, Chapter 4 continuous with the definition of a predictive physical shock absorber model. It starts with the introduction of TFX Suspension Technology's BMW R1200 shock absorber and continuous with the equations governing the shock absorber behaviour. Chapter 5 estimates parameters that are re-

quired by the model, but that can not be provided by TFX Suspension Technology. A measure to quantify the predictive quality of the damper model is presented as well.

The predictive damper model, that has been derived in Chapters 4 and 5, is implemented in a simulation environment in Chapter 6. This chapter discusses the benefits of using the physical damper model over conventional damping models. This report ends with conclusions and recommendations in Chapter 7.

Chapter 2

Literature review

The development of automotive suspension dampers has begun as early as 1900 and still continues today. The first automotive patent on a telescopic hydraulic unit dates back to 1901, hereby laying the foundation of the shock absorber still in use today. Ever since, research is conducted in damper adjustment and methods to measure its characteristics. A general introduction to shock absorbers is presented in Section 2.1, Section 2.2 introduces shock absorber test rigs and damping characteristics. Earlier related work on shock absorber modelling is presented in Section 2.3, reviewing both 'black box' (semi-) empirical- as well as physical models.

2.1 Shock absorber designs

The actual shock due to road irregularities is absorbed by the suspension spring, thus the word 'shock absorber' may be construed as a misconception. The spring is an integral part of the suspension, the other part is the damper that damps the relative motion by converting kinetic energy to thermal energy. In this study, the terms damper and shock absorber will both be used, both referring to the damper part generating the primarily velocity dependent damping force.

A telescopic shock absorber connects the sprung mass to the unsprung mass. It damps the relative motion between the two masses by generating a velocity dependent force. The relative motion between the sprung- and unsprung mass will extent or compress the shock absorber, in literature referred to as rebound- and compression motion respectively. Many different types of dampers exist. A major distinction is the feature of external adjustment to the damping behaviour after the damper has been manufactured. Automotive dampers generally can not be adjusted, in contrast to race- and high-end dampers that include some degree of external adjustment. Shock absorbers come in several variants, two categories can be clearly distinguished: mono-tube and dual-tube shock absorbers. Mono-tube and dual-tube shock absorbers are elaborately described by Dixon [4], a brief description of these types of shock absorbers is presented in the following subsections.

2.1.1 Mono-tube shock absorbers

The mono-tube shock absorber, as displayed in Figure 1.1a on page 2 and schematically represented in Figure 2.1, has two oil-filled chambers separated by a piston. A rod is connected to the piston at one end. Damper compression yields inward motion of the piston rod into

the shock absorber, hereby reducing the volume of one oil-filled chamber. This chamber is re-ferred to as the compression chamber. The other oil-filled chamber, referred to as the rebound chamber, experiences a volume increase and oil will flow through a set of orifices and valves in the piston from the compression- to the rebound chamber. Extending the damper yields an outward motion of the piston rod of the shock absorber, hereby decreasing the rebound chamber's volume and increasing the compression chamber's volume. Oil will flow via the piston orifices and valves from the rebound- to the compression chamber, hereby creating a damping force. A third gas-charged chamber accounts for the volume changes caused by the motion of the piston rod in the shock absorber during shock absorber compression. Since oil is nearly incompressible and the piston rod enters the damper's shell during compres-sion, thus occupying space, gas in the gas chamber will be compressed by an amount that is approximately equal to the volume of the inserted rod. If no gas chamber is present, it will be practically impossible to move the piston rod in the damper. This is shown in Figure 2.1. Some mono-tube dampers are equipped with a free floating gas piston preventing gas in the gas chamber to mix with oil in the compression chamber. Mono-tube dampers that do not have such a separation piston are also known as emulsion dampers [4].
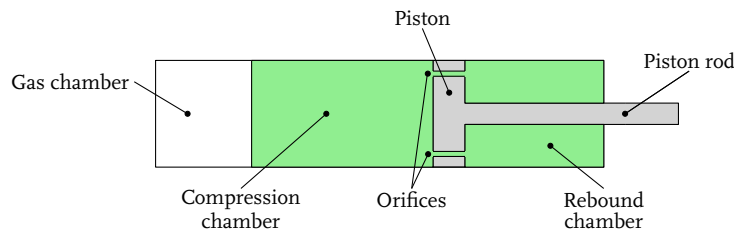
Figure 2.1: Mono-tube shock absorber, adapted from [4]

2.1.2   Dual-tube shock absorbers

Dual-tube shock absorbers, as displayed in Figure 1.1b on page 2 and schematically repre-sented in Figure 2.2, come in two variants. The first variant uses two concentric tubes, see Figure 2.2. The second variant uses a secondary tube outside the shock absorber, see Figure 1.1b and is known as a piggyback damper. Dual-tube dampers have, similar to the mono-tube damper, two oil-filled chambers separated by a piston in the primary tube, a valve assembly connects the primary tube to the secondary tube. Compression will not only force oil to flow from the compression chamber via the piston orifices and valves to the rebound chamber, it will also force oil to flow from the compression chamber, via the base valve assembly, into the secondary tube, also known as the reserve chamber. In reverse, rebound motion forces oil to flow from the rebound chamber to the compression chamber, as well as oil to flow from the reserve chamber via the valve assembly to the compression chamber. The secondary tube is partially gas-charged to account for changes in volume due to motions of the piston rod in the shock absorber. This is shown in Figure 2.2. A major advantage of dual-tube over mono-tube dampers is the base valve assembly, creating more possibilities for the manufacturer to control and adjust the damping characteristics [4].
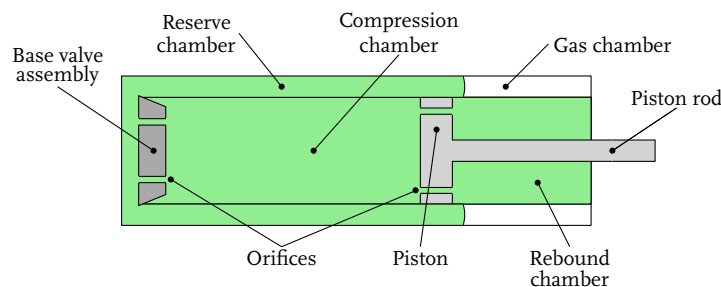
Figure 2.2: Dual-tube shock absorber, adapted from [4]

2.2 Shock absorber testing

According to Dixon [4], testing of shock absorbers can be categorized under three headings which are rig testing, road testing and annual vehicle safety certification. Rig testing may be subdivided in:

- Performance measurements

- Durability checking

- Theoretical model verification

This section provides a general introduction to shock absorber test rigs and test results. A brief introduction to TU/e's shock absorber test rig is presented in Section 3.1, for a detailed description of this test rig is referred to [1].

2.2.1 Testing facilities

Two types of test rigs exist and are categorized by the way they are actuated: electromechanical testers and hydraulic testers. Early electromechanical damper testers use a slider-crank mechanism connected by a connection rod where the inclination of the connection rod introduced a higher harmonic oscillation in the damper motion [4], see Figure 2.3a. This oscillation is removed from the excitation by replacing the connection rod with a Scotch-Yoke driving mechanism, see Figure 2.3b. This mechanism yields a true sinusoidal excitation. Most test rigs measure force by a load cell at the end of the damper not being excited. The crank is actuated by an electric motor mounted on the drive axle, which will always induce some variation in the crank's angular velocity. Control of the excitation speed is enabled by adjusting the excitation frequency by making use of a variable speed motor or gearbox. Variation of the stroke may be possible by disassembly of the tester, setting the stroke to provide a desired maximum speed within limits of the damper and test rig.

Electromechanical testers are usually limited to low-powered units, suitable for low-speed testing. For high-speed testing, thus demanding high-power inputs, hydraulically driven shock absorber testers are preferred [4]. Some additional advantages of a hydraulically actuated test rig exist over electromechanical testers, which can all be assigned to the medium inside the hydraulic system. This medium, also known as the hydraulic fluid, is capable of both transferring heat to a heat exchanger and lubricating the system, both increasing component life of the test rig. Hydraulic actuators may be operated under all kinds of continuous, transient, reversing and stalled conditions. Moreover, closed-loop positioning systems yield less positioning error with respect to electromechanical testers due to high system stiffness [4]. Some disadvantages of hydraulic actuation do exist and are:

- Temperature is an important factor when dealing with hydraulic fluids as fluid properties are highly temperature dependent

- Contaminated oil can clog valves and actuators, maintenance and reliability are therefore strongly related

- Hydraulic devices are more expensive and less accurate in comparison to electronic devices when dealing with low-power input signals

- Small allowable tolerances in the hydraulic system will increase component costs

Furthermore, the bandwidth of electrically actuated damper test rigs is significantly better in comparison to hydraulically actuated rigs. The type of test equipment therefore depends on

test requirements and budget. Although hydraulic rigs are preferred in industry, Roehrig Engineering [5], a leading manufacturer of shock absorber test rigs, only has electromechanical actuated test rigs in their product range.
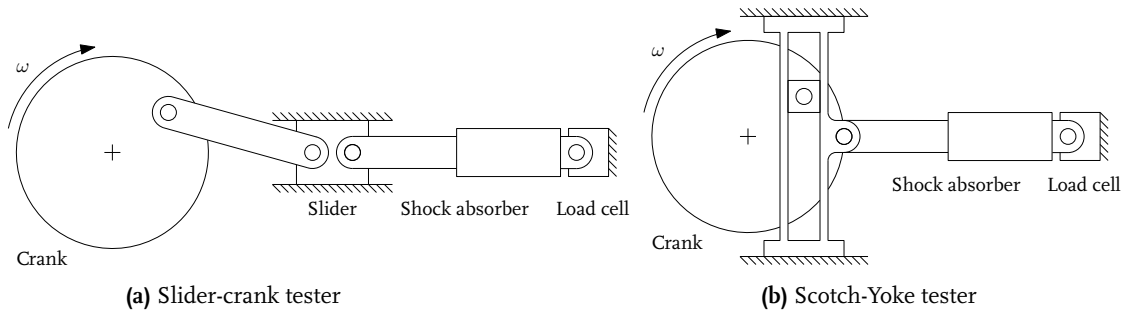

(a) Slider-crank tester

(b) Scotch-Yoke tester

Figure 2.3: Electromechanical shock absorber testers, adapted from [4]

2.2.2 Test results

Several measurements can be made during a shock absorber test. A load cell measures damping force generated by the shock absorber, a position sensor measures damper rod position. Damper-rod velocity can be derived from the change of the damper-rod position over time. A thermocouple can measure shock absorber housing temperature and pressure sensors can measure pressures inside the damper, however, it is unlikely for test rig manufacturers to equip their test rig with such sensors. Based on these measurements, force versus velocity or force versus displacement plots are produced, which both display characteristics of the damper being tested. Two different types of displaying these tests exist and are known as Continuous Velocity Plot (CVP) and Peak Velocity Plot (PVP).

PVP
Peak Velocity Plot, sometimes interchanged with Peak Velocity Pick-off, only measures damping force when the damper velocity is at its maximum when actuated sinusoidally. This peak speeds occurs two times in a cycle, both during mid-stroke position of the actuating ram. They have the same magnitude but are opposite in sign: $\dot{x}_{max} = \pm 2\pi f A$, with f the excitation frequency and A the amplitude. A positive peak speed corresponds to compression, the negative peak speed refers to rebound damping. The creation of a PVP-diagram implies exciting the shock absorber at several frequencies to vary the peak velocity while keeping the amplitude constant. These type of tests are mainly used by mass manufacturers when knowing the general behaviour of the damper is sufficient. An example of a PVP-diagram is presented in Figure 2.4, where it is common for PVP-diagrams to display damping force as function of absolute damper velocity to show differences between rebound- and compression damping.

CVP
Whereas PVP only picks damping force at peak velocity, CVP collects data over a complete cycle. A CVP sinusoidal cycle can be subdivided in four sections as depicted in Figure 2.5. Starting with the hydraulic ram at Bottom Dead Centre (BDC), thus having a fully extended damper, the first quarter of the cycle is compression until peak velocity is reached at midstroke. The second quarter of the cycle is still compressing the damper, however the hydraulic ram is decelerated from peak speed to zero velocity at Top Dead Centre (TDC). Once at zero velocity in TDC, thus having a fully compressed damper, the hydraulic ram keeps decelerating, therefore extending the shock absorber, known as rebound motion, until negative peak velocity is reached mid-stroke. The last quarter of the cycle, which is still rebound motion, accelerates the hydraulic ram until zero velocity is reached in BDC. Note the hysteresis in the velocity plot in Figure 2.5 that is typical for hydraulic dampers. This hysteresis is a result of

the compressibility of the oil inside the damper. A CVP plot contains much more information with respect to a PVP plot, thus CVP is more beneficial when detailed information on damper performance is required.
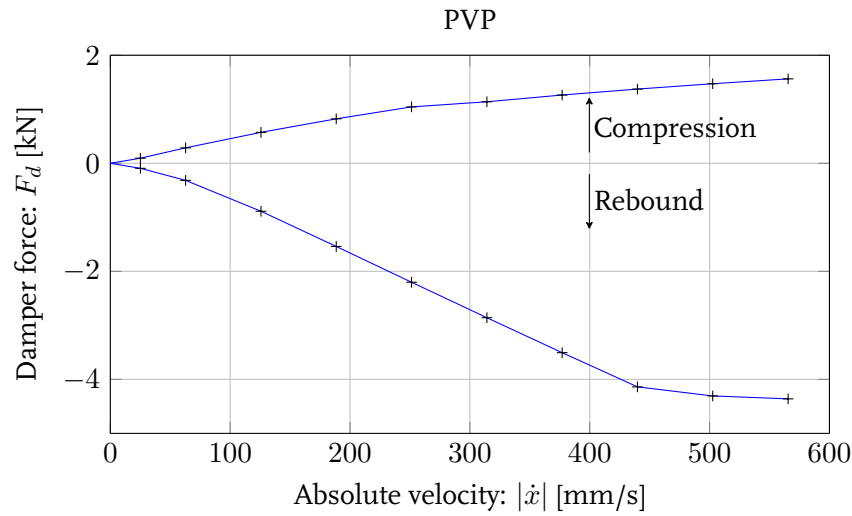
Figure 2.4: TFX Suspension Technology's mono-tube damper PVP-diagram
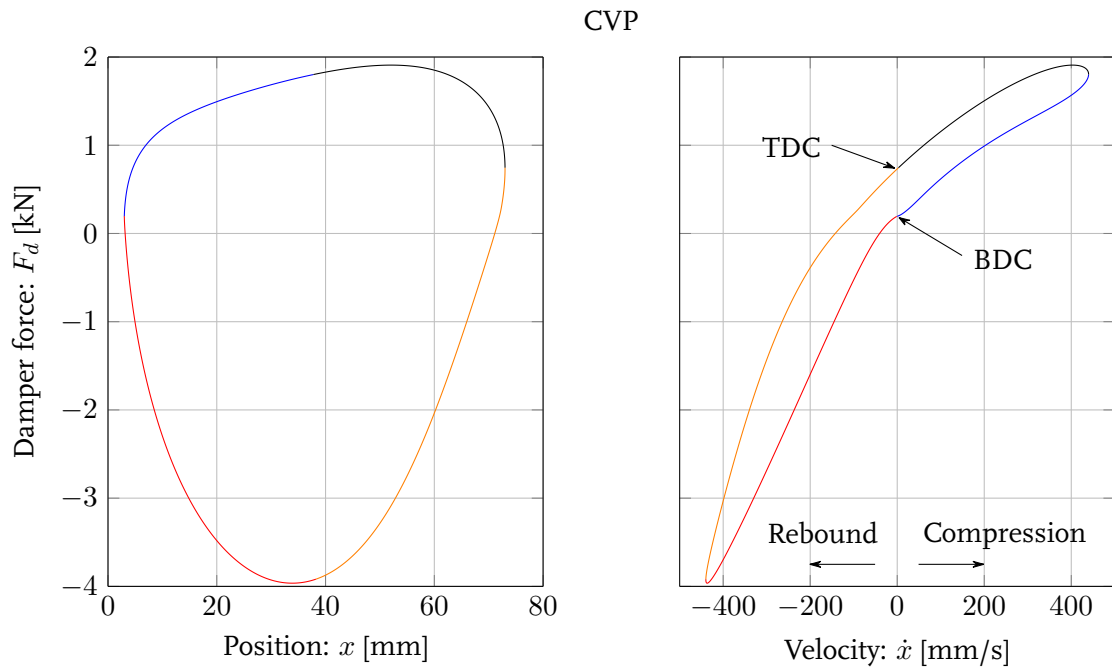
Figure 2.5: TFX Suspension Technology's mono-tube damper CVP-diagram. Compression motion: BDC to mid-stroke in blue and mid-stroke to TDC in black. Rebound motion: TDC to mid-stroke in orange and mid-stroke to BDC in red

2.3 Shock absorber modelling

The earliest, and still one of the most comprehensive and accepted, predictive computer model has been proposed in 1981 by Segel and Lang [6], based on Lang's PhD dissertation in 1977. The model has 82 parameters and gives acceptable agreement with experiments up to excitation frequencies of 1 Hz. Hysteresis at higher frequencies has been attributed to not incorporating fluid compressibility in the model. Lang's model estimates pressure differences over

the piston by correcting Bernoulli's principle with a constant orifice-flow discharge coefficient. Valve opening forces and flow discharge coefficients are determined experimentally.

Reybrouck [7] and Duym [8] both developed parametric models to predict the characteristics of automotive dampers. Both use empirical relations that relate pressure drop to fluid flow by means of an empirical flow restriction equation and a corresponding flow restriction stiffness K:

$$\Delta p\left(Q\right) = KQ^{1.75} \tag{2.1}$$

Reybrouck and Duym both claim that their models are accurate over a wide range of frequencies, however, the use of an empirical flow restriction equation is questionable.

Audenino and Belingardi [9] developed a model to calculate damping characteristics of a dual-tube shock absorber. They were the first to determine that compressibility of the oil and entrained gas in oil is very important when investigating the hysteric behaviour that is typical for hydraulic dampers. Compressibility of the oil and air entrapment in oil is taken into account in their model. Friction has been found to be a secondary effect and is therefore neglected.

In 2002 Talbott and Starkey [10] published a physical model that applies to all types of dampers. Talbott and Starkey aimed to describe the internal physics of a shock absorber to calculate damping characteristics, without making use of empirical relations. Similar to Lang and Segel in 1981, Talbott and Starkey model the flow through piston orifices using Bernoulli's principle to estimate pressure drop across an orifice. Their paper presents two significant contributions to damper modelling: the first one is the derivation of an analytical model to predict valve opening, based on the plate bending equations from *Formulas for Stress and Strain* (Roark & Young, 1975). These so-called shim stack equations are able to predict stack opening for stacks containing 3 to 10 shims of different thickness and diameter. The second contribution of their paper on damper modelling is the relation of gas chamber pressure to compression chamber pressure. The model is able to show good correlation to experimental testing at high velocities, it is however unable to correlate at low test velocities as it does not take compressibility of the oil in consideration. Parametric studies on shim stack stiffness and orifice areas were also performed during this study, providing insights in how hydraulic dampers work as well as guidelines in damper tuning to achieve desired characteristics.

Ferdek and Luczko [11] have claimed the proposition of the first physics based model, capable of predicting damping forces of a dual-tube hydraulic shock absorber in 2012. They have taken compressibility of the oil into account and have incorporated a method of numerical integration to solve the model equations. Although Ferdek and Luczko claim that their model is only based on the internal physics, they incorporate empirical relations to predict the valve opening, which rejects their claim of proposing a full physical model.

Empirical models are based on observations rather than on physics to describe a system. The empirical models that are used to model damper response often use coefficients that relate to state variables of the system, such as position or velocity. These coefficients do not have a distinct meaning, but only correlate to measurements. Furthermore, these type of models are only valid within the range where experimental data has been gathered to obtain the model coefficients. An example of a non-physical empirical damper model is proposed by Belingardi et al. [12], modelling the damper force as function of damper-position and -velocity as a polynomial. This type of polynomial model is known as a restoring force function and is described by:

$$F_d(x, \dot{x}) = \sum_{i,j} a_{ij} x^i \dot{x}^j \qquad (2.2)$$

with F_d the damper force as function of damper-rod velocity $\dot{x}$ and -position x. Coefficients a_{ij} are obtained by a least-squares fitting algorithm. An alternative restoring force model uses damper-rod velocity and -acceleration as independent state variables instead of displacement and velocity. It is claimed that this model may give better results at higher stroking velocities due to an improved representation of inertia of the oil inside the shock absorber:

$$F_d(\dot{x}, \ddot{x}) = \sum_{i,j} a_{ij} \dot{x}^i \ddot{x}^j \qquad (2.3)$$

The main advantages of these restoring force models are that these non-linear models are linear in its parameters. Furthermore, parameter estimation is straight-forward using a least-squares algorithm, making it fast in both parameter estimation as well as computational effort during simulations.

Other simple and fast computing models are proposed by Karadayi and Masada [13], later followed by Besinger et al. [14]. Both have proposed models composed from serial- and parallel combinations of elementary elements, such as springs, dash-pots, friction elements and backlashes. Both claim the creation of simple and computationally fast damper models that are suitable for a full vehicle simulation environment. It is claimed that these models are capable of capturing directional asymmetry, friction, hysteresis, and compressibility of oil.

Furthermore, the study by Pracny et al. [15] is a recent study to propose a Neural Network based approach to model shock absorber response. This study uses a spline approach for the basic force-velocity response, which can easily be changed to modify the main characteristics of the shock absorber. A Neural Network is wrapped around the spline function to model all other effects occurring during shock absorber excitation, such as temperature- and frequency dependent hysteric effects.

2.4 Summary and conclusions

Section 2.1 introduces the mono- and dual-tube shock absorbers and briefly describes their working principles, Section 2.2 presents shock absorber testers and their test results. Section 2.3 reviews earlier work on shock absorber models capable of predicting damping responses as function of damper excitation.

This study aims to develop a model capable of calculating damping forces of a mono-tube damper given its geometries and other factors that may have an influence. Several studies have proposed such models, but none of them appear to incorporate all internal effects. Studies that come close are the work by Ferdek and Luczko [11] and Talbott and Starkey [10]. The first study focussed on a dual-tube damper that may provide a basis for the development of a physical model of the BMW R1200's mono-tube damper, however it lacks an accurate description of the valving. The study by Talbott and Starkey focusses on a mono-tube damper and incorporates an accurate description of the shim stack valves, but does not take compressibility of the oil into account. Furthermore, both studies assume constant pressure loss coefficients. Combining the studies [10] and [11] may provide a good starting point for the development of a physical model for the BMW R1200's damper provided by TFX Suspension Technology.

Chapter 3

TU/e hydraulic shock absorber test rig

The conversion of a Zwick/Rel 1852 series material tester, formerly used by the Materials Department at TU/e, to a functional shock absorber test rig is described by Feijen [1]. A brief summary of the hydraulically actuated shock absorber test rig, which is displayed in Figure 3.1, is presented in Section 3.1. Although the test rig is fully functional, it lacks user-friendliness and clarity on operation- and safety procedures. The implementation of a Graphical User Interface (GUI) is presented in Section 3.2, operation- and safety procedures are presented in Section 3.3. Section 3.4 presents an approach to reduce measurement noise from the load cell that measures the damper force.

(a) Overview   **(b)** Detailed
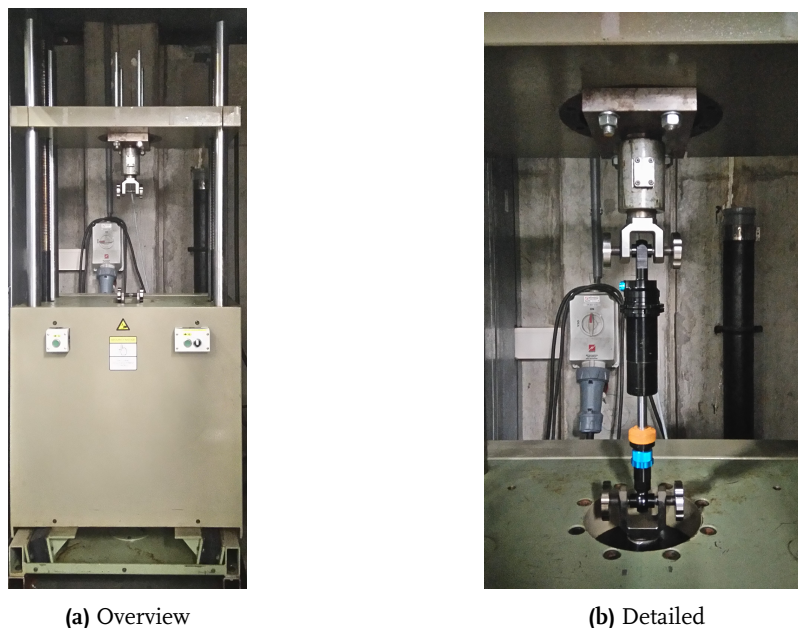
Figure 3.1: TU/e's shock absorber test rig

3.1   Specifications

The material tester's hardware is adapted to enable flexible control of the hydraulic ram by means of a control-loop and data-acquisition to measure the characteristics of the shock absorber under test. The hydraulic power supply is a hydraulic pump with an oil cooler, capable of pumping 28.5 L/min and capable of generating a pressure of 210 bar. The system contains two DOWTY 4551 servo valves to control the flow of oil and two bladder-accumulators

that store energy for transient cases where the hydraulic pump lacks power to actuate the hydraulic cylinder. The hydraulic cylinder is a so-called double-acting, double-rod cylinder. Its most important parameters as specified by its manufacturer [16], are listed in Table 3.1. For hydraulic schemes is referred to [1].

Table 3.1: Data of the Zwick/Rel's hydraulic cylinder [16]

Parameter	Value	Unit
Piston diameter	54	[mm]
Piston rod diameter	45	[mm]
Maximum tensile/compression force	10	[kN]
System pressure for max. force	160	[bar]
Cylinder test pressure	300	[bar]
Maximum stroke	250	[mm]

A rod-eye clamp has been added at one end of the actuated piston rod, dedicated to fix the bottom-end of a shock absorber to the hydraulic ram. Another rod-eye clamp has been added to the fixed force-transducer. This keeps the top-end of the shock absorber in place, allowing to measure the damping force generated by the damper. Control of the hydraulic ram position is done by making use of *MATLAB xPC Target*, enabling the execution of real-time *MATLAB Simulink* models. xPC Target serves real-time testing applications such as hardware-in-the-loop and rapid control prototyping, making it suitable to control the hydraulic test rig. MATLAB's xPC Target needs two computers: one computer is designated for the real-time testing environment, in this case the test rig. This computer is referred to as target computer and runs the Simulink model. An other computer is needed to create the Simulink model, this computer is referred to as host computer and it is connected to the target computer by means of an Ethernet communication cable. The host PC can also serve as a control interface for the target PC. The Simulink model created on the host computer is transferred to the target computer. Real-time tests use the memory and computing power of the target computer.

Two data acquisition cards are installed in the target PC. One card is a PCI-DDA04/12 card and is used to sent control signals to the servo valves in the test rig. The other card is a PCI-DAS1200/JR card and is used for receiving signals from the two sensors installed on the test rig. The first sensor is a 5000 HR Linear Variable Differential Transformer (LVDT) in combination with a LDM-1000 LVDT conditioner to measure the hydraulic ram position, the other sensor is an IWECO ED 517 strain gauges-based force transducer to measure the damper force. The force transducer maximum permissible force is ± 10 kN. A schematic overview of the hardware connections is presented in Figure 3.2.
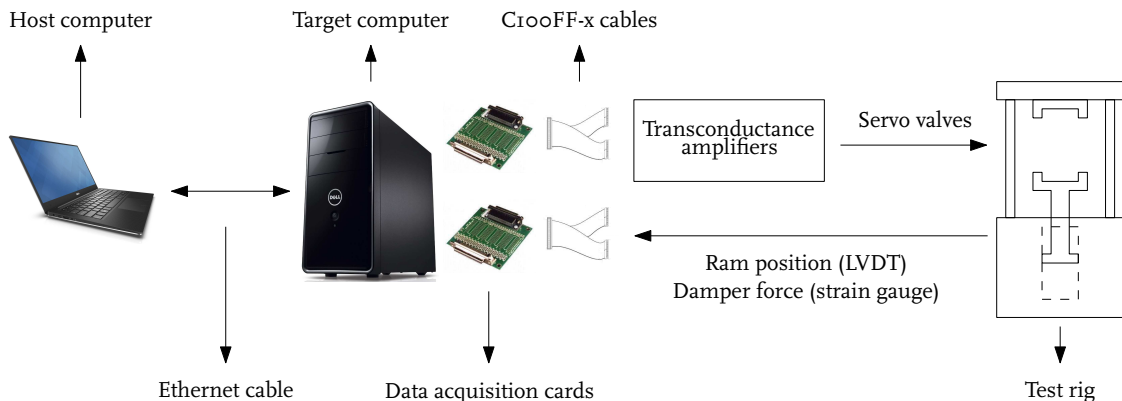
Figure 3.2: Components of the xPC Target real-time testing environment, adapted from [1]

Feijen designed a closed-loop controller for the test rig consisting of a PI-feedback controller, claiming 32 Hz bandwidth. Feed-forward control is added to enhance system performance. The test rig has some limitations: the limited capacity of the hydraulic power supply in combination with the servo valves are limiting the test rig's maximum excitation speed to 0.58 m/s. This implies that increasing the excitation frequency decreases the excitation amplitude. Maximum attainable stroke as function of excitation frequency is presented in Figure 3.3. A detailed description of the feedback- and feed-forward control-loop is provided by Feijen [1].
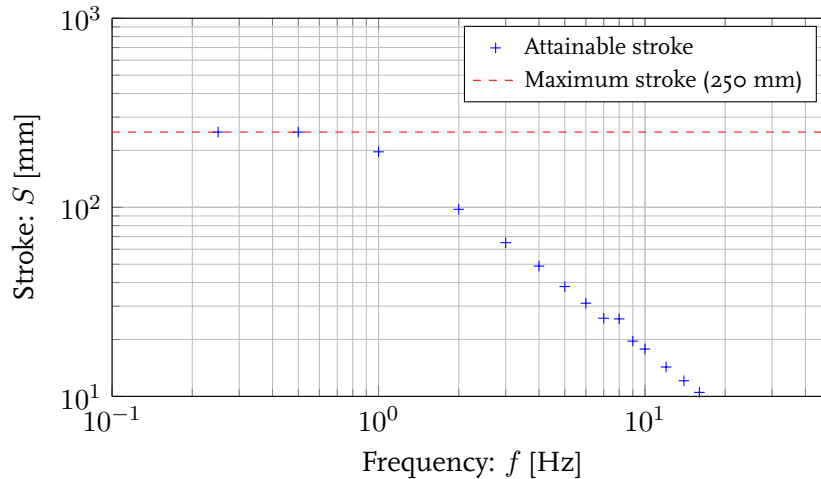

Figure 3.3: Attainable hydraulic ram displacement as function of excitation frequency [1]

Safety measures are introduced to guarantee user-safety when operating the test rig. These measures consist of a combination of two emergency stops that can be pressed any time the rig is operated. Pushing one of these emergency stops will immediately switch off the hydraulic aggregate. Additionally, a two-hand switch to adjust placement of the upper clamping block is implemented to avoid severe injuries to the operator when installing a shock absorber in the test rig. A state flow model is incorporated in the control software to ensure correct execution of a test procedure as introduced in Section 3.3.

3.2 Improving user-friendliness

The initialization of a test, as it was designed by Feijen, was originally done by entering hard coded test parameters in the source code that actuates the test rig. This makes the use of the test rig prone to errors, which may lead to dangerous situations. To increase user safety and enhance the ease of using the test rig, a Graphical User Interface (GUI) is designed with the help of MATLAB's built-in Graphical User Interface Development Environment (GUIDE). This GUI enables the selection of test specifications, such as signal type, excitation frequency and amplitude, and includes some safety measures, for instance to avoid stroking the shock absorber beyond it's maximum allowable stroke or protect the operator from injuries during test execution by providing the status of the test.

The GUI that has been developed is displayed in Figure 3.4. It allows the user to specify the Target PC Settings and connect to the Target PC indicated with panel (1). Shock absorber dimensions should be entered in panel (2), entries in this panel are used to prevent the damper being stroked beyond it's maximum allowable stroke both during damper compression and extension. The real-time measurements of the LVDT and load cell are displayed in panel (3). Control of the motion is enabled in panel (4), allowing the user to select the preferred motion from a drop-down list and specify the amplitude and period of the signal. Specification of the

start position of the test is possible as well. The motion is displayed in panel (5), serving to visually check the preferred trajectory for a specific amount of periods. The group of buttons indicated with (6) allows the user to control the progress of the test and save data afterwards, status bar (7) informs the user with the current status of the test rig.
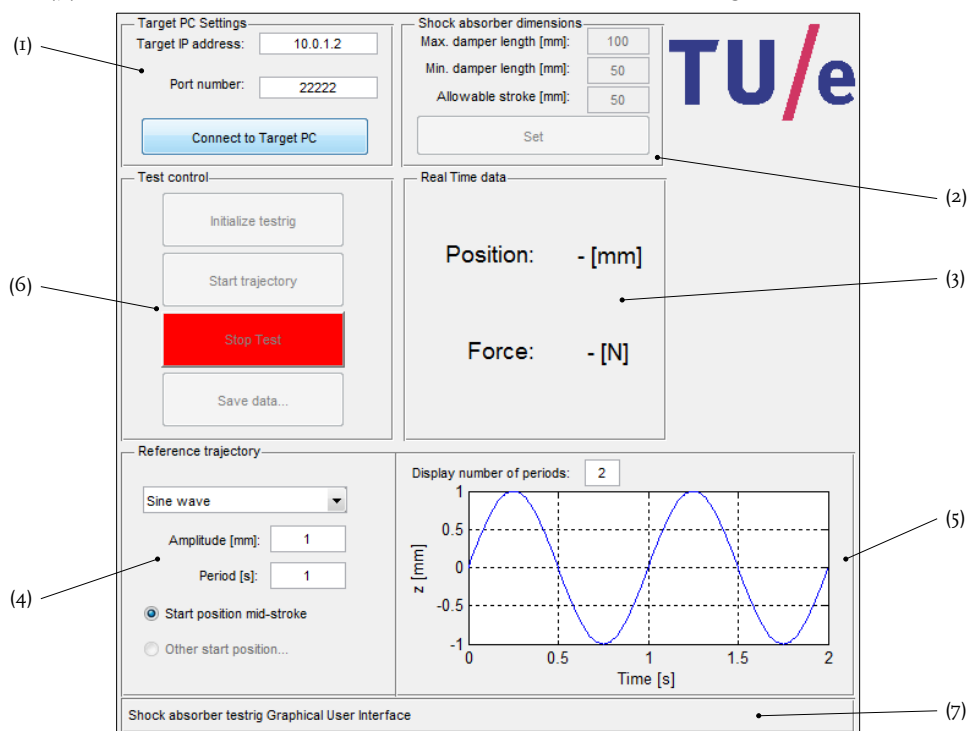
Figure 3.4: Graphical User Interface (GUI) to control the shock absorber test rig

3.3   Operating and safety procedures

This section briefly describes the procedure that should be followed when measuring a damping force time history $F_d(t)$ or damping force characteristics $F_d(x)$ and $F_d(\dot{x})$. The test details, such as frequencies and amplitudes, should be considered before executing the test by taking the maximum permissible stroke of the damper into account. The excitation velocity can be changed by varying both frequency and amplitude of the reference signal. The actual test proceeds as follows:

1. Measure the extreme positions that limit the damper motion, the stroke may now be calculated from $S = L_{max} - L_{min}$ where:

   - S is the damper stroke

   - L_{max} the maximum damper length

   - L_{min} the minimum damper length

   The stroke of the damper needs to be specified when initializing the test later on

2. Set, check and record the adjustable damper settings

3. Enter the target PC settings that can be read from the target PC display. Accept the settings by selecting *Connect to Target PC*

4. Enter the maximum and minimum length of the damper in millimetres and check the pre-calculated permissible stroke as obtained under 1. Accept the damper dimensions by selecting *Set*

5. Select *Initialize test rig*. The host PC will prompt the user to start the aggregate and switch on the bypass valve

6. After the by-pass valve is switched on, the hydraulic ram will move to its lowest position. Once it has reached this position, the user is asked whether a shock absorber should be installed in the test rig.

    6.1. To install a shock absorber or adjust its adjustable settings, such as the position of the bleed needle, select *Yes*. In the case that a shock absorber is already fitted in the test rig, or the adjustable settings of the damper should not be changed, select *No* and move on to 7

    6.2. The host PC will prompt the user to switch off the bypass valve and aggregate. Strictly follow this sequence as installing a shock absorber in the test rig can be dangerous

    6.3. After the aggregate is switched off, a new shock absorber can be installed or its adjustable damper settings can be changed. To install a shock absorber, first mount the upper clamp. Adjust the height of the upper clamping block with the two hand position control to accurately align the damper connection with the lower clamping block on the hydraulic ram

    6.4. Mount the damper in the lower clamping block. Slightly compress the damper by lowering the upper clamping block 3 millimetres by means of the two hand position control to avoid damper rupture when extending the damper during a test

    6.5. Once the damper is adjusted and installed, take manual action on the host PC and start the aggregate and switch the bypass valve on

7. The hydraulic ram will move to the pre-defined start position, which initially is set to mid-stroke. Specify the reference trajectory by means of trajectory type, amplitude and frequency. Start the test by selecting *Start trajectory*

8. To stop the test, select *Stop Test*. The user is prompted to manually switch off the bypass valve and aggregate. Only after both the bypass valve and aggregate are switched off, the test is stopped

9. Data can be saved by selecting *Save data...* To immediately restart the test select *Initialize test rig* and repeat the process from step 5

Stopping the test can be done at any moment by pressing the red *Stop Test* button, prompting the user to manually switch off the bypass valve and aggregate. The two emergency stop buttons can be pressed at any time when operating the test rig. Pressing these buttons will immediately switch off the hydraulic aggregate.

3.4 Measurement noise reduction

The load cell, which is attached to the upper clamping block of the test rig, measures the force generated by the damper. Feijen [1] does not elaborate on processing the measurement data, nor describes methods to reduce high-frequent measurement noise contaminating the force measurement data. This section describes a strategy to reduce this measurement noise by means of a low-pass filter and a time-domain averaging method.

3.4.1   Low-pass filter

A common way to reduce high frequent measurement noise from a time series is applying a zero-phase low-pass Butterworth filter. Selecting the appropriate cut-off frequency for such filters is described by Winter [17] and is known as *cut-off frequency residual analysis*. This residuals based method measures the RMS deviation between an unfiltered signal X and this same signal filtered over a wide range of cut-off frequencies, with signal X containing N data points in time. The RMS residual yields:

$$R\left(f_{co}\right) = \sqrt{\frac{1}{N}\sum_{i=1}^{N}\left(X_i - \hat{X}_i\left(f_{co}\right)\right)^2} \tag{3.1}$$

with $R\left(f_{co}\right)$ is the RMS deviation as function of the cut-off frequency f_{co} and $\hat{X}_i$ the ith filtered data sample.

If the data would only be noise, and thus no signal, the residual plot would be a straight line decreasing from an intercept at 0 Hz to an intercept on the frequency-axis at the Nyquist frequency, i.e. half the sample frequency. The dashed blue line in Figure 3.5 represents an estimate of this noise residual, intercepting the 0 Hz axis at the estimated RMS-value of the measurement noise: $R\left(f_{co} = 0\right) = \sqrt{\frac{1}{N}\sum X_i^2}$. The frequency axis is intercepted at the Nyquist frequency: $R\left(f_{co} = \frac{1}{2}f_s\right) = 0$ as the filtered and unfiltered data are equal at this cut-off frequency.

When the measurement data is a noise contaminated signal, thus being a signal of interest combined with noise, the residual will rise above the straight dashed line when reducing the cut-off frequency. This rise above the dashed line represents signal distortion taking place as the cut-off frequency is reduced, see Figure 3.5. The final decision is to select the appropriate cut-off frequency such that a compromise is made between the amount of signal distortion taking place and the amount of noise that is passed through the filter, which both should be as low as possible.

Figure 3.5 shows the previously described residual analysis plot as function of increasing Butterworth cut-off frequency and filter order. The unfiltered signal X in (3.1) is the unfiltered damper force measured by the load cell. The filtered time signal $\hat{X}$ is this same measured damper force, however, it is filtered with a Butterworth filter at varying cut-off frequency and filter order. The data has been gathered by exciting TFX Suspension Technology's mono-tube damper over its maximum stroke at a frequency of 2 Hz. Figure 3.5 shows a signal distortion RMS-value of 3.2 Newton when filtering the measurement with a 220 Hz second order Butterworth filter. Noise that passes through the filter measures 3.5 Newton at this filter settings. This seems to be a good compromise between signal distortion and noise passing through the filter. A method to further reduce measurement noise that passes through the filter is described in the next subsection.

3.4.2   Time domain cycle averaging

A zero-phase second order Butterworth low-pass filter with a cut-off frequency of 220 Hz has been selected in the previous subsection which, due to the compromise between noise reduction and signal distortion, will still pass through some noise that will affect the measurements. This effect can be further reduced by applying a time-domain averaging method described by Wismer [18]. This type of post-processing is commonly used in the industry for machinery that perform repetitive cycles, such as combustion engines and pumps and can therefore also
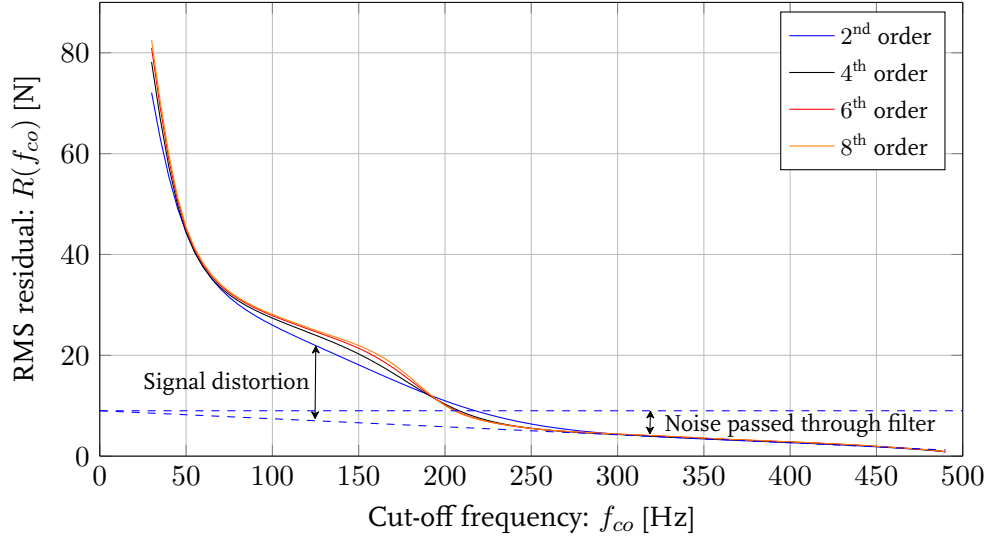
Figure 3.5: Residual between a zero-phase Butterworth filtered and an unfiltered signal as function of the filter cut-off frequency and filter order

be applied on TU/e's hydraulically actuated test rig when performing for example sinusoidal tests. The theory of time domain averaging is briefly described in this subsection.

Consider a time signal X, its power spectrum is G_{XX}. Time signal X is a combination of a signal of interest A and noise N: $X(t) = A(t) + N(t)$, its power spectrum is the combination of the power spectra of the signal of interest and noise: $G_{XX} = G_{AA} + G_{NN}$. If X is a repetitive signal, its noise component can be reduced by time domain averaging of the signal X, yielding the averaged signal $\bar{X}$. Its power spectrum yields:

$$G_{\bar{X}\bar{X}} = G_{AA} + \frac{1}{N_{avg}} G_{NN} \tag{3.2}$$

and contains some power spectrum of interest G_{AA} and a noise spectrum G_{NN}. N_{avg} is the number of cycle averages. Equation (3.2) shows that noise power G_{NN} decreases as the number of cycle averages N_{avg} increases. Explicitly, increasing the number of averages in tenfold reduces the noise component with 10 dB:

$$\text{Reduction} = 10 \log \left(N_{avg} \right) \quad \text{[dB]} \tag{3.3}$$

The final decision is to select the appropriate amount of cycle averages: too few cycles may not sufficiently reduce noise power, too many cycles averages may warm up the shock absorber when testing, which in its turn might affect the damper force. The RMS deviation of a single cycle and some number of cycle averages over N data points in time is defined as:

$$R \left(N_{avg} \right) = \sqrt{\frac{1}{N} \sum_{i=1}^{N} \left(X_i - \bar{X}_i \left(N_{avg} \right) \right)^2} \tag{3.4}$$

Figure 3.6 shows the residuals plot of the damper force as function of cycle averages. The damper force has been measured by exciting TFX Suspension Technology's mono-tube damper at 2 Hz over its maximum stroke. If only one cycle is used, and thus no averaging is taking

place, the RMS deviation is zero as the signals X_i and $\bar{X}_i$ are equal. Increasing the number of averages yields smoother signals, thus increasing the RMS deviation, as confirmed by Figure 3.6. From this figure it can be seen that the RMS deviation tends to increase linearly beyond 30 cycle averages. Further increasing this number is questionable as it might warm up the damper. Furthermore, Figure 3.7 displays time history damper force for varying numbers of cycle averages, showing that curve smoothness does not significantly improve after 30 cycle averages, hence 30 cycle averages are performed when measuring damper forces.
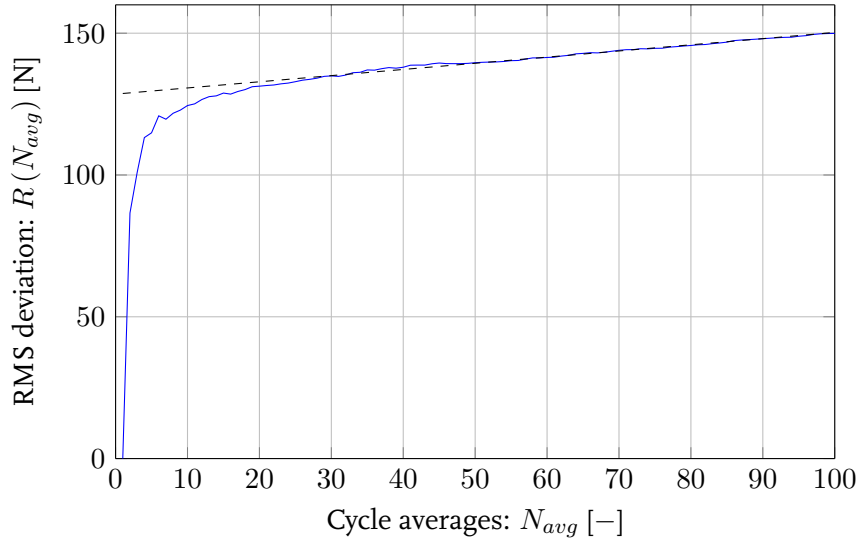
Figure 3.6: RMS deviation between a single- and N_{avg} cycle averaged measurement

3.5 Summary

Section 3.1 provides a brief summary of the work by Feijen [1] that converted a material tester to a functional shock absorber test rig. Although the rig was functional, it lacked user-friendliness and clarity on operation- and safety procedures that both might lead to dangerous situations when operating the test rig.

The implementation of a Graphical User Interface (GUI), presented in Section 3.2, enhances user-friendliness. Clarity on operation procedures and safety measures is presented in Section 3.3.

The study by Feijen does not conduct any form of data processing, Section 3.4 presents an approach to reduce high-frequent measurement noise from the load cell that measures damper force. A 2nd order zero-phase low-pass Butterworth filter with a cut-off frequency of 220 Hz seems appropriate to reduce noise as a first stage, time-domain averaging reduces noise that passes through the Butterworth filter as a second stage, 30 cycle averages seems appropriate.
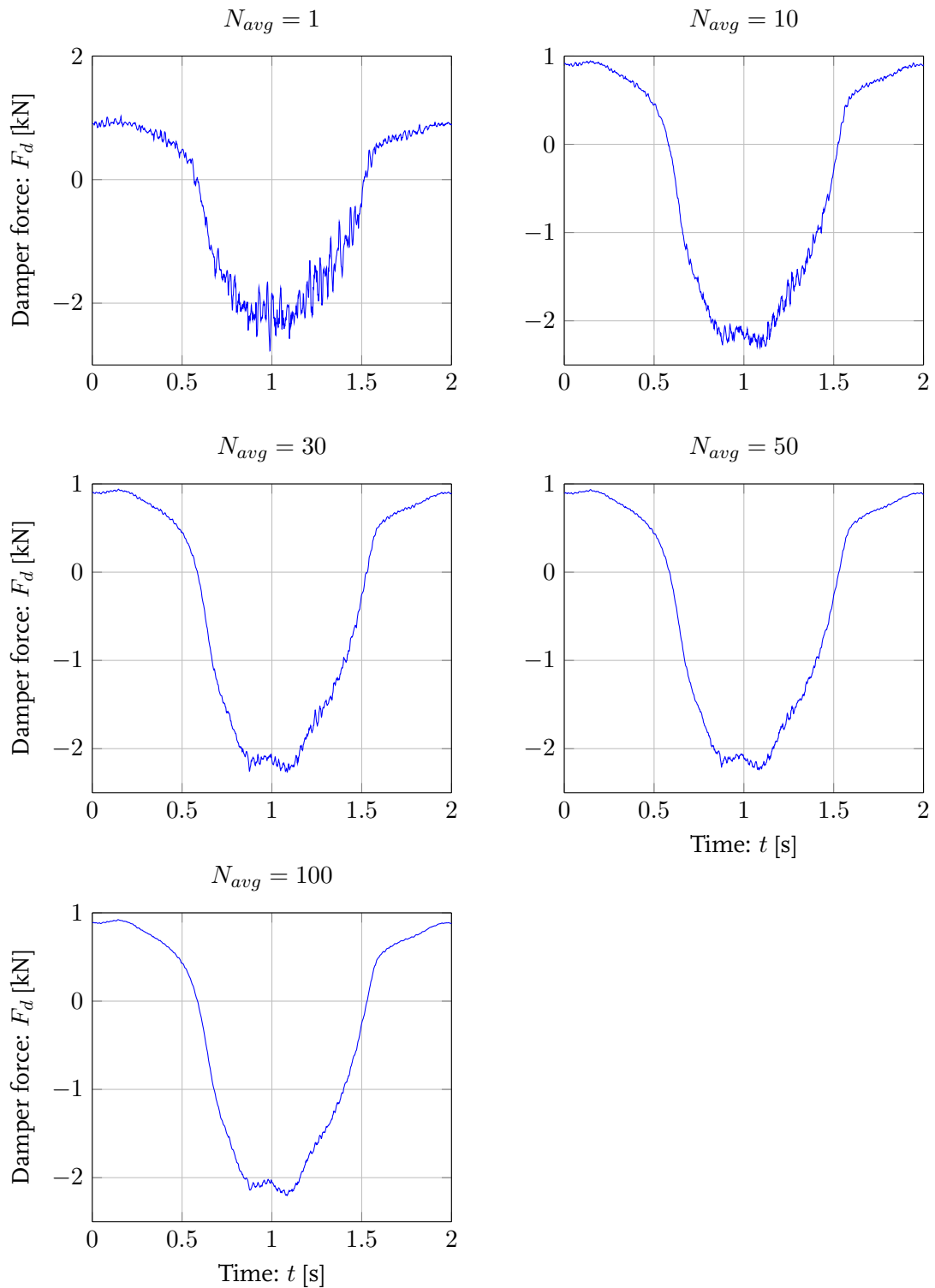
Figure 3.7: Damper force time history for different number of cycle averages. The measurements are obtained from TFX Suspension Technology's mono-tube damper, sinusoidally excited with 2 Hz over its maximum stroke. Measurements are filtered with a zero-phase second order Butterworth filter with a cut-off frequency of 220 Hz as discussed in Section 3.4.1

Chapter 4

Mono-tube shock absorber model

This chapter aims to derive a simulation model that can be used to predict damping forces generated by the mono-tube damper provided by TFX Suspension Technology. It starts with a description of the damper, a force model relating the damping forces to the internal pressures is discussed afterwards. Sections 4.3 to 4.6 introduce the flow model that describes mechanisms affecting fluid pressures in the system.

4.1   System description

The mono-tube damper provided by TFX Suspension Technology that is used as a baseline in modelling, testing and validating the physical damper model during this study is depicted in Figure 1.1a. Figure 4.1 on page 25 presents a schematic representation of this damper. The damper fits a BMW R1200 GS Adventure motorcycle and has a length of 410 mm when uncompressed, its maximum stroke is 78 mm. TFX equips this type of damper with some degree of external adjustment, as will be discussed later.

The mono-tube damper has two oil filled chambers separated by a piston assembly that controls the flow of oil from one chamber to the other. One chamber decreases in volume during damper compression. This chamber is referred to as the compression chamber and is denoted with subscript 'c'. The other chamber experiences increase of volume when compressing the damper, this is the rebound chamber and denoted by subscript 'r'. Compression- and rebound chamber pressures are denoted with p_c and p_r respectively.

The piston that separates the compression- from the rebound chamber is connected to a piston rod. To account for the insertion of the piston rod in the damper, a third gas-filled chamber, referred to with subscript 'gas', is present inside the damper. TFX Suspension Technology pre-charges this gas chamber with nitrogen gas. Its initial absolute pre-load pressure is denoted with $p_{gas,0}$, its initial chamber height is $L_{gas,0}$. Although some mono-tube dampers are equipped with a free-floating separation piston preventing oil and gas to mix, TFX's gas chamber has an open interface with the oil-filled compression chamber. This makes the fluid inside the compression- and rebound chamber a mixture of nitrogen gas and oil, which has a significant effect on the bulk modulus of the fluid as discussed in more detail in Appendix A. Audenino and Belingardi [9] state that volume fractions up to 10% nitrogen gas dissolved in the mixture are possible, this study assumes volumetric fractions of $f_v = 5\%$, which corresponds to a constant mass fraction of $f_m = 7.4 \cdot 10^{-3}\%$ at atmospheric pressure.

Two rod eyes serve to install the damper on a motorcycle. For the purpose of this study, rubber mountings are removed from these rod eyes and replaced by spherical bearings to eliminate contributions of these rubbers to damping force. A rubber bump-stop avoiding the piston to reach its end-stroke is also removed from the system. Its contributions in terms of force to damping force are therefore disregarded. Damper excitation is described in terms of piston rod position x, velocity $\dot{x}$ and acceleration $\ddot{x}$. The fully extended damper is denoted with $x = 0$, other relevant geometries are displayed in Figure 4.1 and are listed in Table E.3.

The piston assembly consists of a parallel combination of two valves that serve to control the flow of oil from one chamber to the other. The first valve is a needle valve located in the hollow centre of the piston rod, this valve is in the damper industry also known as the bleed valve. External adjustment of this needle valve allows to adjust throttle area of this valve, hereby controlling the overall damping characteristics of the shock absorber. The second valve is a stack of several thin circular plates, known as shims, laying on top of a series of orifices through the piston. This type of valve is in the damper industry known as the shim stack valve. Its working principle approximates a blow-off valve: it will open above some threshold pressure. The piston is equipped with two shim stack valves: one controlling the flow during damper compression, known as the compression shim stack valve, and one controlling the flow during damper extension, known as the rebound shim stack valve. Changing the composition of these shim stacks, in terms of shim thickness and outer radius, allows for adapting flow behaviour through these valves. The piston has 3 orifices to allow oil flow during rebound- and 6 orifices to allow oil flow during compression motion. The latter is schematically presented in Figure 4.1. The following sections derive models that relate changes in fluid pressure, chamber volumes and fluid mass to forces generated by the mono-tube damper.

4.2 Damper force model

Figure 4.1 shows all forces and pressures acting on the mono-tube damper. Four pressures can be distinguished:

- Gas chamber pressure: p_{gas}
- Compression chamber pressure: p_c
- Rebound chamber pressure: p_r
- Ambient pressure: p_0

and are all assumed to be constant within their respective volumes. Additional friction forces act between:

- piston and mono-tube body
- piston-rod and piston-rod seal

The sum of these friction forces is denoted with F_f. Applying Newton's second law and taking into account that the top end of the damper is fixed, yields two expressions that relate forces and pressures acting on the system to the resistant damping force:

$$
\begin{aligned}
F_{d1} &= p_r A_r + p_0 A_{rod} - m_{wp} \left(\ddot{x} + g \right) - p_c A_c - \text{sign} \left(\dot{x} \right) F_f \qquad (4.1)\\
F_{d2} &= p_r A_r + p_0 A_c + m_t g - p_{gas} A_{gas} - p_0 A_r - \text{sign} \left(\dot{x} \right) F_f \qquad (4.2)
\end{aligned}
$$

with F_{d1} the damping force on the piston rod and F_{d2} the damping force at the top end of the
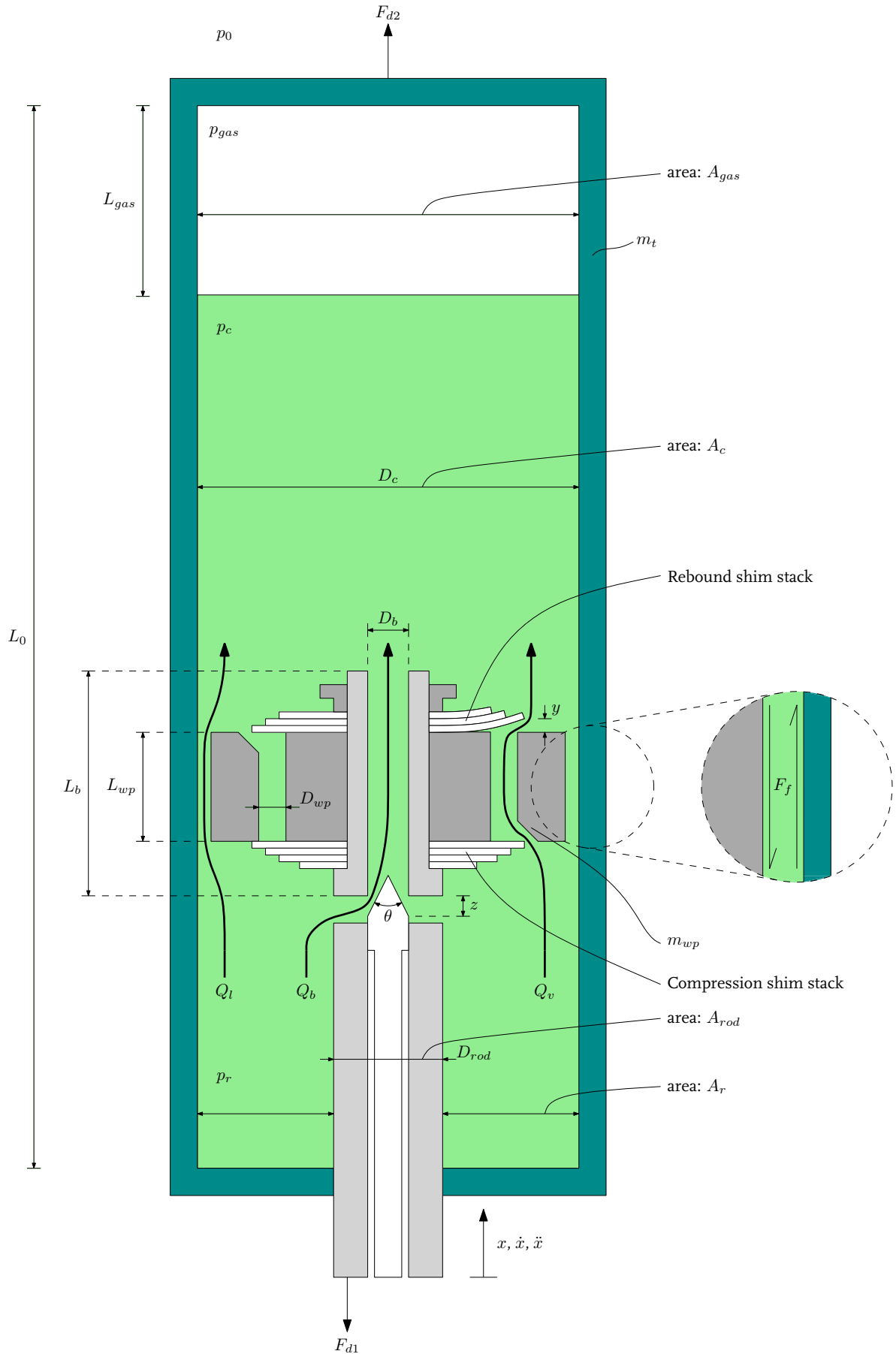
Figure 4.1: Schematic representation of the mono-tube damper. Rebound motion opens the rebound shim stack

mono-tube damper. The sum of piston rod- and piston assembly masses is denoted with m_{wp}, mass of the mono-tube body is denoted with m_t. The cross-sectional areas of the piston-rod and gas-, compression- and rebound-chambers are referred to as A_{rod}, A_{gas}, A_c and A_r respectively. Due to geometrical considerations these are related by:

$$A_c = A_{gas} = A_r + A_{rod} \tag{4.3}$$

The test rig that is used to validate the model derived during this study measures damping force with a load cell attached to the fixed mono-tube body's top end, hence (4.2) will be used for comparing calculated damper forces to measurements.

Some mono-tube dampers are equipped with a free-floating piston that separate the compression chamber from the gas chamber, preventing oil and gas to mix. The pressure difference over such a separating gas piston follows from:

$$m_{gp}\ddot{x}_{gp} = p_c A_c - p_{gas} A_{gas} - \text{sign}\left(\dot{x}_{gp}\right) F_{f,gp} - m_{gp}g \tag{4.4}$$

that describes the equation of motion of the gas piston. Eq. (4.4) relates gas chamber pressure to compression chamber pressure and was first derived by Talbott and Starkey [10]. The gas-piston mass is denoted with m_{gp}, $\ddot{x}_{gp}$ refers to gas-piston acceleration. Friction forces acting between the free-floating gas piston and mono-tube body are denoted with $F_{f,gp}$. The mono-tube damper provided by TFX Suspension Technology is not supplied with such a separation piston, hence (4.4) is disregarded and gas chamber pressure and compression chamber pressures are assumed to be equal and constant within their respective volumes: $p_c = p_{gas}$.

Literature found that friction forces are small compared to damping forces when stroking the damper at low velocities [4, 10, 11] and are therefore neglected. Substituting (4.3) in (4.2) and recall $p_c = p_{gas}$ yields an expression to solve for the damping force:

$$F_{d2} = p_r A_r - p_c A_c + p_0 A_{rod} + m_t g \tag{4.5}$$

which demonstrates that damper force directly relates to pressures in the rebound- and compression chambers. Models must now be derived for describing these pressures.

4.3 Flow model

As introduced in Section 2.1, two modes of operation in a damper exist: compression and rebound. Rebound flow from the rebound- to the compression chamber only occurs if $p_r > p_c$. This flow differs from the flow from the compression- to the rebound chamber, mainly due to differences in cross-sectional areas of the flow orifices, as will be introduced in Section 4.6. This requires the definition of two different oil flows: Q_{rc} and Q_{cr}, where subscripts refer to the chamber names between which the flow occurs, e.g. flow rate Q_{rc} refers to oil flow from the rebound- to the compression chamber.

Derivation of the flow model starts with the general expression of mass conservation in integral form:

$$\frac{\partial}{\partial t} \int_V \rho \, dV + \int_A \rho \left(\mathbf{v} \cdot \mathbf{n}\right) dA = 0 \tag{4.6}$$

with $\mathbf{n}$ the outwardly directed normal vector on a system's boundary and $\mathbf{v}$ the fluid-velocity vector crossing the system's boundary. Evaluating (4.6) over the compression chamber yields an equation that describes the change of mixture mass in the compression chamber:

$$\frac{\partial}{\partial t} \left[\rho_c V_c \right] + \rho_c Q_{cr} - \rho_r Q_{rc} = 0 \tag{4.7}$$

Evaluating (4.6) over the rebound chamber yields an equation that describes the change of mixture mass in the rebound chamber:

$$\frac{\partial}{\partial t} \left[\rho_r V_r \right] + \rho_r Q_{rc} - \rho_c Q_{cr} = 0 \tag{4.8}$$

$\rho_c Q_{cr}$ is the flow of mixture mass leaving the compression chamber entering the rebound chamber. $\rho_r Q_{rc}$ is the flow of mixture mass leaving the rebound chamber and thus entering the compression chamber. The first term on the left hand side of (4.7) and (4.8) describe the change in mixture mass due to chamber expansion or change in mixture density. ρ_r and ρ_c are the densities of the liquid-gas mixture in the rebound- and compression chamber respectively. V_r and V_c are the rebound- and compression chamber volumes.

Conservation of mass requires oil leaving the compression chamber to enter the rebound chamber:

$$\dot{m}_c = -\dot{m}_r \tag{4.9}$$

with $\dot{m}_c$ and $\dot{m}_r$ the increase of mass in the two chambers related to the mixture densities and flows Q_{rc} and Q_{cr}:

$$\begin{aligned} \dot{m}_c &= -\dot{m}_r \\ &= \rho_r Q_{rc} - \rho_c Q_{cr} \end{aligned} \tag{4.10}$$

Combining (4.7) and (4.10) and substituting $\frac{\partial \rho_c}{\partial t} = \frac{\partial \rho_c}{\partial p_c} \frac{\partial p_c}{\partial t}$ yields an equation relating the change in fluid pressure in the compression chamber to changes in mixture mass and chamber volume in this chamber:

$$\frac{\partial p_c}{\partial t} = \frac{\rho_c}{V_c} \frac{\partial p_c}{\partial \rho_c} \left[\frac{\dot{m}_c}{\rho_c} - \frac{\partial V_c}{\partial t} \right] \tag{4.11}$$

Combining (4.8) and (4.10) and substituting $\frac{\partial \rho_r}{\partial t} = \frac{\partial \rho_r}{\partial p_r} \frac{\partial p_r}{\partial t}$ yields an equation relating the change in fluid pressure in the rebound chamber to changes in mixture mass and chamber volume in this chamber:

$$\frac{\partial p_r}{\partial t} = \frac{\rho_r}{V_r} \frac{\partial p_r}{\partial \rho_r} \left[\frac{\dot{m}_r}{\rho_r} - \frac{\partial V_r}{\partial t} \right] \tag{4.12}$$

Introducing the effective bulk modulus

$$\beta = \rho \left(\frac{\partial p}{\partial \rho} \right) \tag{4.13}$$

27

that describes the resistance of a substance to compression [19] and derived in Appendix A yields:

$$\dot{p}_r = \frac{\beta_r}{V_r} \left[\frac{\dot{m}_r}{\rho_r} - \dot{V}_r \right] \tag{4.14}$$

$$\dot{p}_c = \frac{\beta_c}{V_c} \left[\frac{\dot{m}_c}{\rho_c} - \dot{V}_c \right] \tag{4.15}$$

The effective bulk moduli $\beta_r = \rho_r \frac{\partial p_r}{\partial \rho_r}$ and $\beta_c = \rho_c \frac{\partial p_c}{\partial \rho_c}$ refer to the effective bulk modulus of the mixtures in the rebound and compression chamber respectively. Rebound chamber volume and its derivative with respect to time are directly related to the piston position x and velocity $\dot{x}$:

$$V_r = A_r x \tag{4.16}$$

$$\dot{V}_r = A_r \dot{x} \tag{4.17}$$

Compression chamber volume follows from the total damper volume V_0 minus the sum of rebound chamber-, gas chamber- and piston-rod insertion volumes:

$$V_c = V_0 - V_r - V_{gas} - A_{rod} x \tag{4.18}$$

Its time derivative equals:

$$\dot{V}_c = -\dot{V}_r - \dot{V}_{gas} - A_{rod} \dot{x} \tag{4.19}$$

The gas chamber is filled with nitrogen gas that satisfies a polytropic relation:

$$p_{gas} V_{gas}^{\kappa} = p_{gas,0} V_{gas,0}^{\kappa} \tag{4.20}$$

with $\kappa = 1.4$ the polytropic coefficient for nitrogen gas [20]. Subscript '0' refers to initial gas chamber pressure and -volume. Recall that the pressure in the compression chamber equals the pressure in the gas chamber as no separating piston is present in the damper. Equation (4.20) can be differentiated to obtain the derivative of gas chamber volume with respect to time:

$$\dot{V}_{gas} = -\dot{p}_c V_{gas,0} \left(\frac{p_{gas,0}^{\frac{1}{\kappa}}}{\kappa p_c^{\frac{1}{\kappa}+1}} \right) \tag{4.21}$$

Substituting (4.17) in (4.14) yields finally an equation that describes the change of mixture pressure in the rebound chamber:

$$\dot{p}_r = \frac{\beta_r}{V_r} \left[\frac{\dot{m}_r}{\rho_r} - A_r \dot{x} \right] \tag{4.22}$$

Substituting (4.19) and (4.21) in (4.15) yields finally an equation that describes the change of mixture pressure in the compression chamber:

$$\dot{p}_c = \frac{\kappa \beta_c p_c^{\frac{1}{\kappa}+1}}{\kappa V_c p_c^{\frac{1}{\kappa}+1} + \beta_c V_{gas,0} p_{gas,0}^{\frac{1}{\kappa}}} \left[\frac{\dot{m}_c}{\rho_c} + A_c \dot{x} \right] \tag{4.23}$$

The latter two equations describe a system of two ordinary differential equations and relate changes in mixture pressure to mass flow and chamber expansion. Equation (4.22) demonstrates that compressing the shock absorber will decrease rebound chamber pressure. In contrast, (4.23) shows that damper compression will rise compression chamber pressure. Furthermore, mass influx increases fluid pressures, mass outflux decreases fluid pressures.

The density of the gas and oil mixture in both the rebound- and compression chamber are related to the pressures in these chambers. The densities of these mixtures are derived in Appendix A and equal:

$$\rho_{mix} = \left(\frac{f_m}{\rho_{gas}} + \frac{1 - f_m}{\rho_l} \right)^{-1} \tag{4.24}$$

with f_m the constant mass fraction of nitrogen gas in the mixture. The densities of the individual gas and liquid at pressure p are denoted with ρ_{gas} and ρ_l are derived in Appendix A and equal:

$$\rho_{gas} = \rho_{gas,0} \left(\frac{p}{p_0} \right)^{\frac{1}{\kappa}} \tag{4.25}$$

$$\rho_l = \rho_{l,0} \left[1 + \beta_l^{-1} (p - p_0) \right] \tag{4.26}$$

The density of nitrogen gas and hydraulic liquid at atmospheric pressure p_0 are denoted with $\rho_{gas,0}$ and $\rho_{l,0}$ respectively. The bulk modulus of the liquid is denoted with β_l and is provided by the supplier of the oil. The effective bulk modulus of the mixtures in the compression- and rebound chamber, β_c and β_r respectively, is described by (4.13). Substituting (4.25) and (4.26) in (4.24) yields finally an expression for the mixture density. Deriving with respect to the pressure p yields finally an expression for the effective bulk modulus of the liquid-gas mixture:

$$\beta_{mix} = \rho_{mix} \left(\frac{\partial \rho_{mix}}{\partial p} \right)^{-1} = \frac{\dfrac{f_m}{\rho_{gas,0} \left(\frac{p}{p_0} \right)^{\frac{1}{\kappa}}} + \dfrac{1 - f_m}{\rho_{l,0} \left(1 + \beta_l^{-1}(p - p_0) \right)}}{\dfrac{f_m}{\kappa p \rho_{gas,0} \left(\frac{p}{p_0} \right)^{\frac{1}{\kappa}}} + \dfrac{\beta_l (1 - f_m)}{\rho_{l,0} (\beta_l + (p - p_0))^2}} \tag{4.27}$$

This equation relates the effective bulk modulus in the compression and rebound chamber to the fraction of nitrogen gas dissolved in the liquid and the pressure in these chambers.

Equation (4.10) describes mass flow between the two chambers. The total flow of oil, both during rebound- and compression operation, potentially comprises from three separate flow paths:

1. bleed flow through the centre of the piston rod: Q_b

2. valve flow through the piston passing the shim stack valves: Q_v

3. leak flow bypassing the piston: Q_l

Figure 4.1 presents a schematic overview of these three potential oil flows during a rebound stroke. A tight seal prevents oil to leak from the compression- to the rebound chamber and vice-versa. Leak flow is therefore disregarded, making the total flow a sum of bleed- and valve flow:

$$
\begin{aligned}
Q_{rc} &= Q_{v,r} + Q_{b,r} \\
Q_{cr} &= Q_{v,c} + Q_{b,c}
\end{aligned}
\tag{4.28}
$$

Subscripts 'r' and 'c' are used to indicate valve- and bleed flow during rebound motion and compression motion respectively. The following sections relate pressure losses to these two flows.

4.4 Hydraulic pressure loss

Several components are known to affect hydraulic system pressure, examples of such components are valves, changes in cross-sectional area, bends and branches. Furthermore, viscous friction between fluid and pipeline will also affect the hydraulic pressure. This section aims to relate these viscous friction and component losses to flow of fluid through a system of pipelines.

4.4.1 Pipe friction pressure loss

Pressure losses in a pipeline as a result from viscous friction between the hydraulic fluid and pipe walls is dependent on a number of factors, the most important are:

- flow velocity (e.g. volume flow and pipe dimensions)

- surface conditions of the pipe line

- liquid properties such as density and viscosity

A complete derivation of pressure loss depending on these factors is described by Nakayama and Boucher [21] and can be summarized as:

$$
\Delta p = f \frac{L}{D_h} \frac{1}{2} \rho \bar{v}^2
\tag{4.29}
$$

Pressure loss Δp relates to the average flow velocity $\bar{v}$, pipe length L and a Darcy friction factor f. The hydraulic diameter is defined as $D_h = \frac{4A}{P}$, with A the cross-sectional area of the pipeline and P the wetted perimeter. The hydraulic diameter reduces to the inner diameter of a pipe for circular pipes. The Darcy friction factor for smooth pipes is related to the Reynolds number: $f = k\frac{64}{Re}$, with correction factor k. The Reynold number relates inertial fluid forces to viscous friction forces for some given flow condition:

$$
Re = \frac{\rho \bar{v} D_h}{\mu}
\tag{4.30}
$$

with μ the dynamic viscosity of the hydraulic fluid. Although values for the correction factor k are tabulated in literature, this study aims to find a value for this correction factor by means of a parameter estimation method described in Section 5.2.
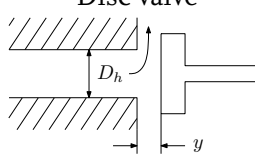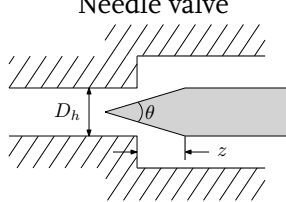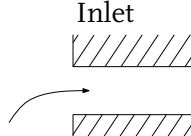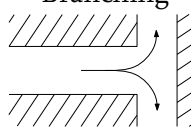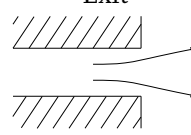
4.4.2 Component pressure loss

In addition to the previously described pipe frictional loss, losses may also occur through components such as changes in cross-sectional area, changes in flow direction, branching or valving. Pressure loss for such cases is generally expressed as:

$$\Delta p = K \frac{1}{2} \rho \bar{v}^2 \tag{4.31}$$

again relating pressure loss Δp over the component to the mean upstream flow velocity $\bar{v}$ and loss coefficient K. Several studies aimed to quantify these loss coefficients for different type of components [21–23], most important coefficients for components included in the mono-tube damper are tabulated in Table 4.1.

Table 4.1: Loss coefficients for various components [21–23]

Component type	Loss coefficient estimate
Disc valve	Throttle area $a_{t,v} = \pi D_h y$ Valve seat cross section $a_v = \pi \frac{D_h^2}{4}$ Loss coefficient $K \approx c_1 + c_2 \left(\frac{a_v}{a_{t,v}} \right)^2$
Needle valve	Throttle area $a_{t,b} = \pi \left(D_h z \tan \frac{\theta}{2} - z^2 \tan^2 \frac{\theta}{2} \right)$ Valve seat cross section $a_b = \pi \frac{D_h^2}{4}$ Loss coefficient $K \approx c_1 + c_2 \left(\frac{a_b}{a_{t,b}} \right)^2$
Inlet	Loss coefficient $K \approx 0.05$ - 3 (shape dependent)
Branching	Loss coefficient $K \approx 0.69$
Exit	Loss coefficient $K \approx 1$

4.4.3 Total loss along a pipeline

Pressure losses due to pipe friction and components have been described previously, the total pressure loss from pipe entrance to exit is the sum of the two individual losses:

$$\Delta p = \left(k \frac{64}{Re} \frac{L}{D_h} + \sum K \right) \frac{1}{2} \rho \bar{v}^2 \tag{4.32}$$

The first term on the right hand side expresses pressure loss by viscous wall friction, while $\rho \bar{v}^2 \sum K$ represents the sum of pressure loss due to flow entrance or exit, valves or bending of flow direction. For long pipelines, such that $k \frac{64}{Re} \frac{L}{D_h} \gg \sum K$, losses other than viscous losses may be neglected. In contradiction, short pipelines that include considerable friction components such that $\sum K \gg k \frac{64}{Re} \frac{L}{D_h}$, viscous losses may be neglected. Rewriting (4.32) and recall $Q = a\bar{v}$ with $a = \pi \frac{D_h^2}{4}$ the cross section, yields an expression that relates volumetric flow-rate to pressure loss:

$$Q = a\zeta \sqrt{\frac{2}{\rho}} \sqrt{\Delta p} \tag{4.33}$$

with flow resistance coefficient $\zeta = \left(k \frac{64}{Re} \frac{L}{D_h} + \sum_i K_i \right)^{-\frac{1}{2}}$.

4.5 Bleed flow

An orifice through the centre of the piston rod allows oil to bypass the shim stack valves, thus allowing oil to flow from one chamber to the other. This oil flow is referred to as bleed flow Q_b and relates to the pressure difference over this orifice: $p_r - p_c$. A needle valve is included in the flow path, enabling the adjustment of the overall damping behaviour. The setting of this needle valve can be externally adjusted, see Figure 4.1. The position of the bleed needle is adjusted by screwing the threaded needle into the hollow piston rod. A mechanism clicks every 30 degrees to indicate the position of the needle. The number of clicks n_c indicate the position of the bleed needle. $n_c = 0$ refers to a closed bleed orifice, thus forcing all oil to flow via the shim stack valves. $n_c = 43$ is a fully opened bleed orifice, thus allowing oil to flow via both the bleed- and shim stack valves. The pitch of the threaded needle is known, the model accounts for the variability in needle valve setting.

The flow through the bleed orifice relates to the pressure loss over the bleed orifice as derived in Section 4.4:

$$\begin{aligned} Q_{b,r} &= a_b \zeta_{b,r} \sqrt{\frac{2}{\rho_r}} \sqrt{p_r - p_c} \quad \text{if} \quad p_r > p_c \\ Q_{b,c} &= a_b \zeta_{b,c} \sqrt{\frac{2}{\rho_c}} \sqrt{p_c - p_r} \quad \text{if} \quad p_c > p_r \end{aligned} \tag{4.34}$$

with subscripts 'r' and 'c' referring to flow during rebound- and compression flow respectively. $a_b = \pi \frac{D_b^2}{4}$ equals the cross-sectional area of the bleed orifice. The complex geometry of the piston requires the definition of two different loss factors $\zeta_{b,r}$ and $\zeta_{b,c}$, that relate to the sum of the viscous pipe friction ($k \frac{64}{Re} \frac{L_b}{D_b}$) and the summed component losses ($\sum K_i$) as derived in Section 4.4:

$$\zeta_b^{-2} = k \frac{64}{Re} \frac{L_b}{D_b} + \sum_i K_i \tag{4.35}$$

L_b and D_b are the length and hydraulic diameter of the bleed orifice respectively. Nakayama and Boucher [21] and Janna [22] propose estimates for individual component losses as listed in Table 4.1. The bleed flow in TFX Suspension Technology's hydraulic damper include a flow entrance ($K_i \approx 1.5$), a needle valve ($K_i \approx c_1 + c_2 \left(\frac{a_b}{a_{t,b}} \right)^2$), a branching flow ($K_i \approx 0.69$) and a pipe exit ($K_i \approx 1$). Summation of the latter allows expressing the sum of component losses as:

$$\sum_i K_i = C_1 + C_2 \left(\frac{a_b}{a_{t,b}} \right)^2 \tag{4.36}$$

with bleed throttle area $a_{t,b} = \pi \left(D_b z \tan \frac{\theta}{2} - z^2 \tan^2 \frac{\theta}{2} \right)$ see Figure 4.1. The unknown parameters C_1 and C_2 in (4.36) and k in (4.35) should be obtained from parameter estimations as will be discussed in Section 5.2.

4.6 Valve flow

Figure 4.1 shows the piston assembly during rebound motion. The rebound shim stack opens and controls valve flow during rebound motion. The other shim stack remains closed and only opens during compression and is referred to as the compression shim stack. Flow through the valve Q_v relate to the pressure difference across the piston. The pressure difference acting on the shim that is closest to the piston generates a force deflecting the shim stack. The model accounts for variability in shim stack opening as derived in Appendix B.

Pressure loss over the shim stack valve relates to the flow rate through this valve as derived in Section 4.4:

$$
\begin{aligned}
Q_{v,r} &= a_v \zeta_{v,r} \sqrt{\frac{2}{\rho_r}} \sqrt{p_r - p_c} \quad \text{if} \quad p_r > p_c \\
Q_{v,c} &= a_v \zeta_{v,c} \sqrt{\frac{2}{\rho_c}} \sqrt{p_c - p_r} \quad \text{if} \quad p_c > p_r
\end{aligned}
\tag{4.37}
$$

a_v equals the summed cross-section of the valve orifices: $a_v = n\pi \frac{D_{wp}^2}{4}$. n is the number of orifices during rebound- $n = 3$ and compression flow $n = 6$. The complex geometry of the piston again requires the definition of two individual resistance coefficients $\zeta_{v,r}$ and $\zeta_{v,c}$. Similar to the loss factor during bleed flow, the loss factor ζ_v relates to viscous pipe friction and component losses:

$$\zeta_v^{-2} = k \frac{64}{Re} \frac{L_{wp}}{D_{wp}} + \sum_i K_i \tag{4.38}$$

with L_{wp} the height of the piston and D_{wp} the hydraulic diameter of the piston orifices for valve flow. References [21,22] aim to describe the individual component losses that are present in the flow path of valve flow as listed in Table 4.1. This flow path include a flow entrance ($K_i \approx 1.5$), a shim stack valve ($K_i \approx c_1 + c_2 \left(\frac{a_v}{a_{t,v}} \right)^2$) and a flow exit ($K_i \approx 1$). Summation of the latter allows expressing the sum of component losses over the shim stack valve as:

$$\sum_i K_i = C_1 + C_2 \left(\frac{a_v}{a_{t,v}} \right)^2 \tag{4.39}$$

Throttle area $a_{t,v}$ relates to tip deflection y of the shim laying directly on top of the piston and perimeter πD_v. D_v is the diameter of this shim. The complex geometry of the piston makes it necessary to introduce two parameters that describe the throttle area of the valve flow: one parameter that describes the compression flow throttle area and one parameter that describes the rebound flow throttle area. The piston that separates the rebound chamber from the compression chamber has three orifices to allow rebound flow, but has six orifices to allow compression valve flow. The throttle areas are therefore corrected with a factor $\frac{3}{9}$ and $\frac{6}{9}$ for rebound and compression valve flow throttle area respectively, yielding:

$$a_{t,v,c} = \frac{2}{3} \pi D_v y$$
$$a_{t,v,r} = \frac{1}{3} \pi D_v y \tag{4.40}$$

with $a_{t,v,c}$ and $a_{t,v,r}$ referring to throttle area during compression- and rebound motion respectively. The valve seat area a_v in (4.39) is the sum of valve orifices cross-sectional areas:

$$a_{v,c} = 6\pi \frac{D_{wp}^2}{4}$$
$$a_{v,r} = 3\pi \frac{D_{wp}^2}{4} \tag{4.41}$$

The unknown parameters C_1 and C_2 in (4.39) and k in (4.38) are obtained from parameter estimations presented in Section 5.2. A model that determines the tip deflection of the bottom shim y is presented in Appendix B.

4.7 Summary

This chapter introduces a model capable of calculating damping forces of a mono-tube damper as function of an arbitrary excitation signal. It starts with a general system description of the mono-tube damper. The mono-tube damper consists of two oil-filled chambers that are separated by a piston and one gas chamber having an open interface with the compression chamber. Homogeneous pressure distributions are assumed in all three chambers. The nitrogen gas is assumed to satisfy a polytropic relation. All media in the mono-tube are assumed to behave isothermally. Contributions of the bump stop and friction forces are disregarded.

Oil is able to flow from one oil-filled chamber to the other via a parallel combination of two valves, hereby creating damping force. Leakage of oil from one chamber to the other is disregarded. The model that relates changes in fluid pressure to changes in fluid volume and -mass follows from the general expression of mass conservation in integral form, yielding a system of two non-linear ordinary differential equations described by (4.22) and (4.23).

The first valve is an orifice in the centre of the piston rod, its throttle area can be adjusted by a needle valve. Flow through this valve is referred to as bleed flow and is described by (4.34). The other valve is a composition of small circular plates, known as shims, stacked on top of the piston. Flow through this valve is referred to as valve flow and is described by (4.37). Changing the composition of the so-called shim stack in terms of shim thickness and outer radius allows for adapting the valve flow behaviour. Appendix B describes a model to calculate

opening of the shim stack based on the linearised equations for bending of circular plates from Young and Budynas [24] as function of pressure differences over the piston.

Chapter 5

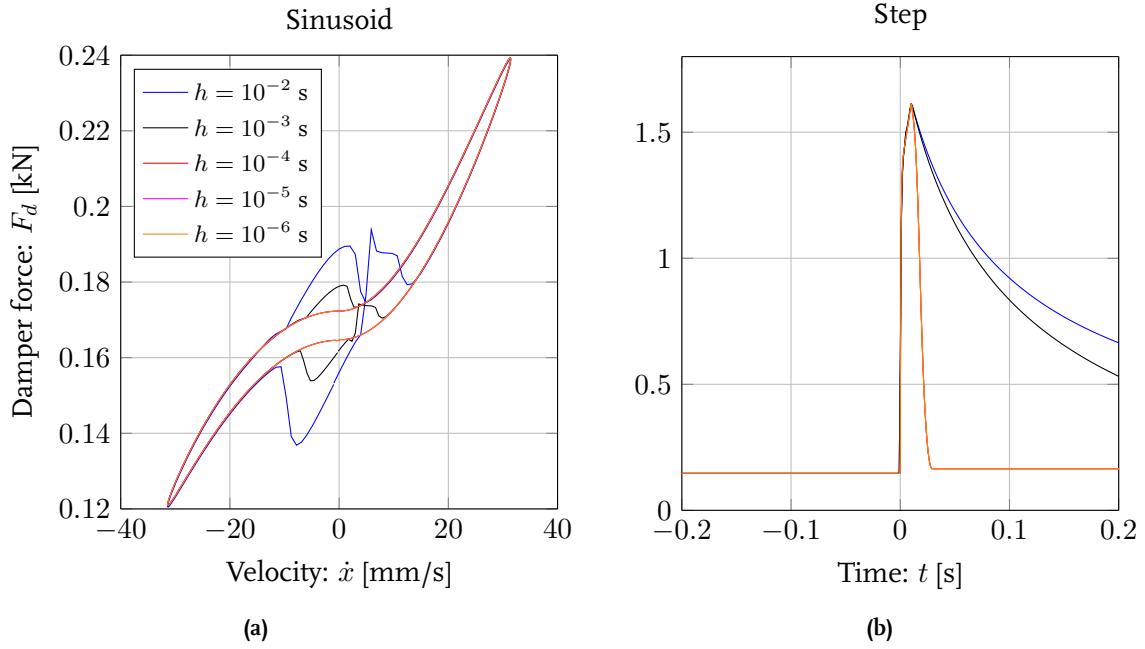# Model parametrization and accuracy

The previous chapter derives a model capable of calculating the damping response of TFX Suspension Technology's mono-tube damper. A system of non-linear ordinary differential equations is derived that relates changes in mass and chamber volume to changes in fluid pressure. Furthermore, volumetric flow rates through the valves are related to pressure differences over these valves. Section 5.1 describes the integration with respect to time of the system of non-linear differential equations. All parameters that describe the model are known from data provided by TFX Suspension Technology, except for four flow resistance coefficients. These coefficients relate volumetric flow rate through the valves to pressure differences over these valves: $\zeta_{b,r}$, $\zeta_{b,c}$, $\zeta_{v,r}$ and $\zeta_{v,c}$. Section 5.2 presents a constrained optimization algorithm to estimate these flow resistance coefficients with the help of test rig measurements on the mono-tube damper. Section 5.3 provides a measure that describes the mono-tube model's predictive quality. This chapter concludes with a description of damper operation.

5.1 Numerical integration algorithm

The model that has been derived in Chapter 4 relates changes in fluid pressure in the rebound- and compression chamber to changes in fluid-volume and -mass. A fourth order Runge-Kutta scheme, as described by Heath [25], is used to solve the system of non-linear differential equations that calculates the pressures inside the damper and the resulting damper force as function of damper excitation. The Ordinary Differential Equation (ODE) that should be solved is provided in Appendix C. A proper fixed stepsize should be selected to solve the system, this can be done by selecting an initial stepsize and decrease this step size until the solution converges.

Figure 5.1a shows solutions of the fourth order Runge-Kutta scheme for different values of stepsize h, varying logarithmically equidistant from $h = 10^{-3}$ to $h = 10^{-6}$ seconds. The damper is sinusoidally excited with excitation frequency $f = 1$ Hz. As observed from this figure, the solution seems to converge at stepsize $h = 10^{-4}$ s as this stepsize yields the same solution as $h = 10^{-5}$ s and $h = 10^{-6}$ s. Figure 5.1b shows the solutions of the Runge-Kutta scheme for a step excited damper by using the same logarithmically equidistant stepsizes. Similar to the sinusoidal excited damper, the solution seems to converge at stepsize $h = 10^{-4}$ s as this stepsize yields the same solution as $h = 10^{-5}$ s and $h = 10^{-6}$ s. Although these observations do not prove that the solution is converged at this stepsize, it is assumed that a stepsize of $h = 10^{-4}$ seconds is appropriate. Further decreasing the stepsize does not improve

the solution, but will only increase computational costs.

Figure 5.1: Solutions of the fourth order Runge-Kutta scheme to predict damping force as function of **(a)** sinusoidal excitation and **(b)** step excitation for different step sizes

5.2 Model parametrization

Almost all parameters that describe the mono-tube model that has been derived in Chapter 4 are provided by TFX Suspension Technology with the exception of four flow resistance coefficients that relate volumetric flow rate through the bleed- and shim stack valve to pressure differences over these valves: $\zeta_{b,r}$, $\zeta_{b,c}$, $\zeta_{v,r}$ and $\zeta_{v,c}$. Exact values for these coefficients should be obtained by means of a parameter estimation algorithm using measurements. This algorithm is described in this section.

Parameter estimation for a model using a single (or a series of) measurement(s) is commonly done by minimizing a squared error function. This function is the difference between an observed value, in this study the measured damper force $\bar{F}_d$, and a predicted value, in this study the predicted damper force $\hat{F}_d$. The error function is also known as a cost function. As introduced previously, the parameters $\mathbf{x}$ that should be estimated are the four flow resistance coefficients relating the volumetric flow rate to pressure differences over the valves. The algorithm that describes this parameter estimation algorithm summarizes as:

$$\begin{aligned} \underset{\mathbf{x}}{\text{Minimize}} \quad & f(\mathbf{x}) \\ \text{subject to} \quad & \mathbf{x} \in \mathcal{X} \subseteq \mathbb{R}^+ \end{aligned} \tag{5.1}$$

with $\mathbf{x} = \begin{bmatrix} \zeta_{b,r} & \zeta_{b,c} & \zeta_{v,r} & \zeta_{v,c} \end{bmatrix}^T$ the column of variables and $f(\mathbf{x})$ the cost function that should be minimized:

$$f(\mathbf{x}) = \sum_i \left(\hat{F}_i(\mathbf{x}) - \bar{F}_i \right)^2 \tag{5.2}$$

with $\bar{F}_i$ the measured damper force at some ith data point and $\hat{F}_i(\mathbf{x})$ the damper force calculated by the mono-tube model as derived in Chapter 4 at the same ith data point.

As there is mutual interaction between valve flow and bleed flow, making it difficult to assess them individually, it would be most ideal to estimate both sets of flow resistance coefficients independent from each other. To do so, two types of dampers should be available. One damper should have a closed bleed orifice forcing all oil to flow through the valves from one chamber to the other. This damper would allow to isolate the pressure loss due to valve flow from the pressure loss due to bleed flow. This allows estimation of valve flow resistance coefficients independent from the bleed valve. A second damper equipped with a closed piston would force all oil to flow through the bleed valve, isolating bleed flow from valve flow. This damper would allow estimation of the bleed valve resistance coefficients independent from the shim stack valves. Unfortunately, TFX Suspension Technology is not able to deliver this set of dampers, forcing the estimation of bleed valve resistance coefficients by taking the mutual interaction between valve flow and bleed flow into account. The parameter estimation algorithm is therefore subdivided in two steps:

1. Estimation of the valve flow resistance coefficients based on measurements with a closed bleed orifice, thus forcing all oil to flow through the shim stack valves

2. Estimation of the bleed valve resistance coefficients by using the shim stack valve resistance coefficients obtained in step one for different settings of the bleed needle

Measurements on the mono-tube damper show that stroking the damper at constant velocity generates near constant damping forces as depicted in Figure 5.2. Equation (4.5) demonstrates that constant damper forces only occurs when the pressure difference over the piston is constant:

$$F_{d2} = p_r A_r - p_c A_c + p_0 A_{rod} + m_t g \qquad (4.5)$$

which in it's turn ensures a constant shim stack deflection. The previously described parameter estimation algorithm is therefore performed by stroking the damper at constant velocity, as this also yields constant Reynolds numbers. This allows a better approximation of the shim stack- and bleed valve flow resistance coefficients. Results of the parameter estimation algorithm are discussed in the next subsections.
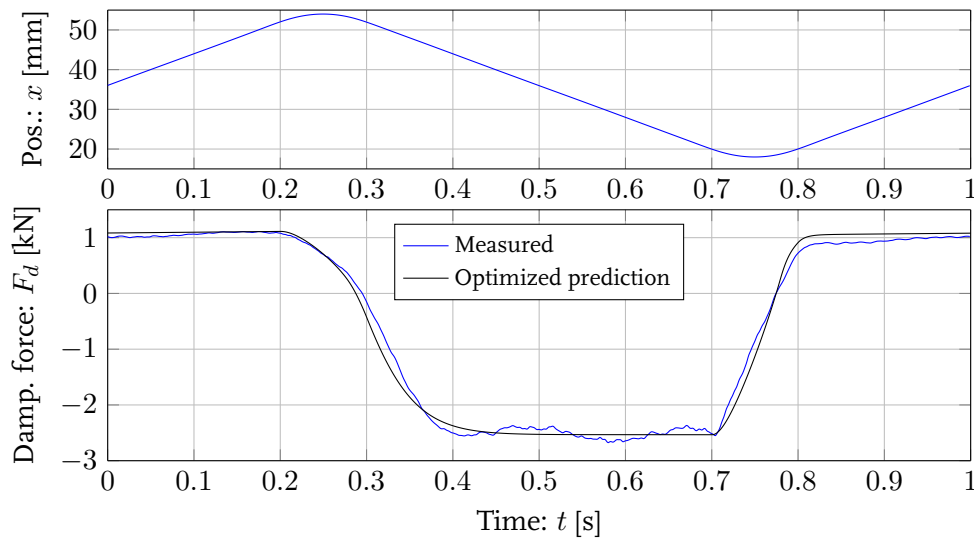
Figure 5.2: Approximate constant damper force (blue) when exciting the damper with constant velocity by means of a smoothed triangular wave. The optimization result is depicted in black

39

5.2.1 Valve flow resistance coefficient estimation

Section 4.6 introduced the flow resistance coefficient relating flow rate through a valve to the pressure difference across the valve. The flow resistance coefficient is derived in Section 4.4 and equals the inverted square root of the sum of viscous pipe friction and component losses. The previously described optimization algorithm estimates quantities for these flow resistance coefficients.

The mono-tube damper is provided with a basic shim stack composition listed in Table E.1 to estimate the valve flow resistance coefficients. A different shim stack composition will be used to quantify the model's predictive quality later on. The bleed needle is closed, i.e. $n_c = 0$, when performing valve flow resistance coefficient estimation measurements to isolate valve flow from bleed flow. Several measurements are performed by varying the excitation speed, measuring both damper force and piston position. The parameter estimation algorithm uses these two time-history measurements to estimate the flow resistance coefficients. Reynolds numbers and shim stack deflection are calculated by the mono-tube model, yielding valve flow resistance coefficient optima presented in Figure 5.3. The latter allows to make estimates for the unknown constants C_1, C_2 and k that describe the valve flow resistance coefficients $\zeta_{v,c}$ and $\zeta_{v,r}$ by means of a least-squares curve-fitting algorithm:

$$\zeta_{v,c}^{-2} = 1.48 \frac{64}{Re} \frac{L_{wp}}{D_{wp}} + 12.35 + 0.138 \left(\frac{a_{v,c}}{a_{t,v,c}} \right)^2 \tag{5.3}$$

$$\zeta_{v,r}^{-2} = \underbrace{1.11 \frac{64}{Re} \frac{L_{wp}}{D_{wp}}}_{k \frac{64}{Re} \frac{L_{wp}}{D_{wp}}} + \underbrace{3.01 + 1.56 \cdot 10^{-3} \left(\frac{a_{v,r}}{a_{t,v,r}} \right)^2}_{\sum K} \tag{5.4}$$

The coefficients of determination, also known as R-squared, for these fits are $R^2 = 0.8082$ and $R^2 = 0.6608$ for compression valve flow and rebound valve flow respectively.

5.2.2 Bleed flow resistance coefficient estimation

Estimation of the bleed flow resistance coefficients uses the shim stack valve resistance coefficients obtained in the previous subsection. Several measurements are performed by varying both bleed needle setting $n_c = 10$, 20, 30 and 40 clicks and excitation speed, again measuring both damping force and piston position. The parameter estimation algorithm uses these two time-history measurements to estimate flow resistance coefficients. Reynolds numbers are calculated by the mono-tube model. Optimum bleed flow resistance coefficients are presented in Figures 5.4 and 5.5, allowing to make estimates for C_1 and C_2 and k that describes the bleed flow resistance coefficients $\zeta_{b,c}$ and $\zeta_{b,r}$ by means of a least-squares curve-fitting algorithm:

$$\zeta_{b,c}^{-2} = 8.92 \frac{64}{Re} \frac{L_b}{D_b} + 2.646 + 0.485 \left(\frac{a_b}{a_{t,b}} \right)^2 \tag{5.5}$$

$$\zeta_{b,r}^{-2} = \underbrace{4.64 \frac{64}{Re} \frac{L_b}{D_b}}_{k \frac{64}{Re} \frac{L_b}{D_b}} + \underbrace{3.153 + 0.436 \left(\frac{a_b}{a_{t,b}} \right)^2}_{\sum K} \tag{5.6}$$

The coefficients of determination for these fits are $R^2 = 0.9385$ and $R^2 = 0.9435$ for compression- and rebound bleed flow respectively.

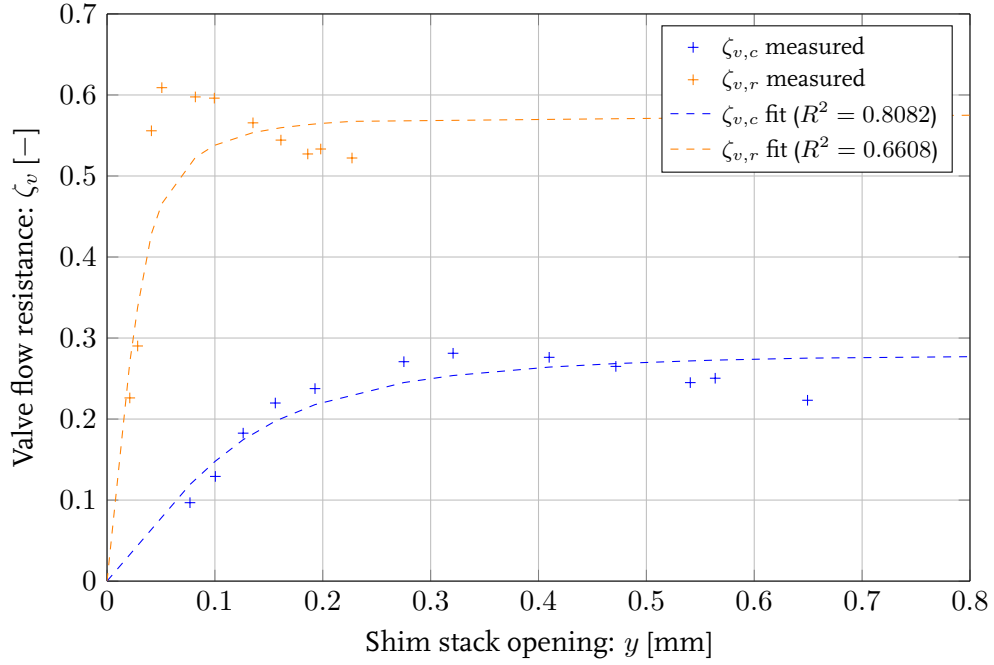**Figure 5.3:** Optimized valve flow resistance coefficients for compression (blue) and rebound (orange)

Fit: $\zeta_{b,c} = \left(8.92 \frac{64}{Re} \frac{L_b}{D_b} + 2.646 + 0.4853 \left(\frac{a_b}{a_{t,b}} \right)^2 \right)^{-\frac{1}{2}}$
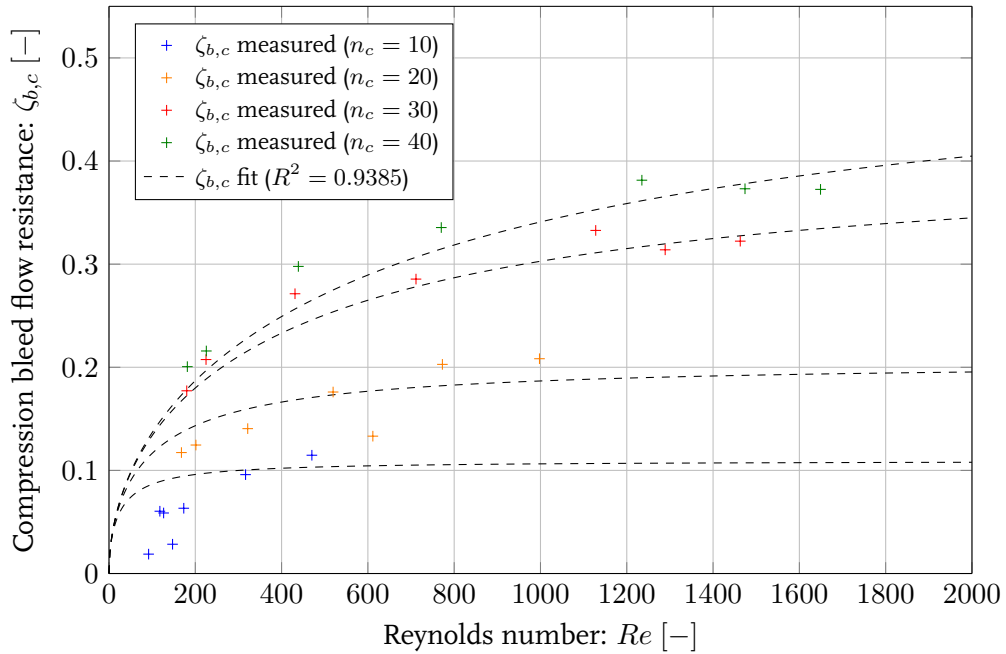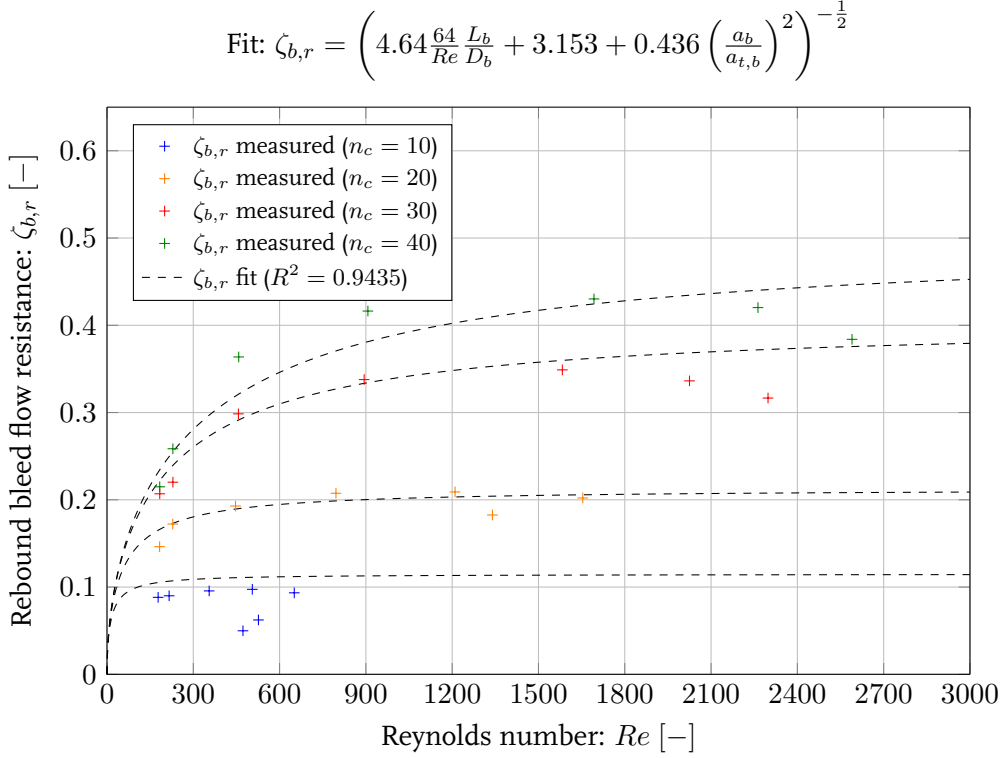

Figure 5.4: Optimized bleed flow resistance coefficients during compression stroke for different settings of the bleed needle and a least-squares fit (dashed)

$$\text{Fit: } \zeta_{b,r} = \left(4.64 \frac{64}{Re} \frac{L_b}{D_b} + 3.153 + 0.436 \left(\frac{a_b}{a_{t,b}} \right)^2 \right)^{-\frac{1}{2}}$$

Figure 5.5: Optimized bleed flow resistance coefficients during rebound stroke for different settings of the bleed needle and a least-squares fit (dashed)

5.3 Model predictive quality

This section aims to provide an insight in the predictive quality of the physical shock absorber model that has been derived in Chapter 4 and has been parametrized in the previous section. To do so, both the predictive quality with respect to the baseline damper that has been used for model parametrization, as well as a modified damper are investigated. This modified damper has a shim stack as listed in Table E.2. Its initial nitrogen-gas pre-load charge an gas chamber height are modified to 11 bar and 65 mm respectively. Damper characteristics of both dampers are presented in Figure 5.6. Both dampers are sinusoidally stroked at varying excitation frequencies, positions of the bleed needle are varied as well. The dampers can only be stroked over their maximum permissible stroke up to frequencies of 4 Hz due to test rig limitations. Exciting the dampers with frequencies over 4 Hz is done by reducing the amplitude to 5 millimetres.

A normalized RMS model error E_{NRMS} is suggested to indicate the predictive quality of the model and is defined as the fraction of the RMS error over the range of measured data:

$$E_{NRMS} = \frac{E_{RMS}}{\bar{F}_{d,max} - \bar{F}_{d,min}} \tag{5.7}$$

with $\bar{F}_{d,max} - \bar{F}_{d,min}$ the range of measured data and E_{RMS} the RMS model error defined as:

$$E_{RMS} = \sqrt{\frac{1}{n} \sum_{i=1}^{n} \left(\bar{F}_{d,i} - \hat{F}_{d,i} \right)^2} \tag{5.8}$$
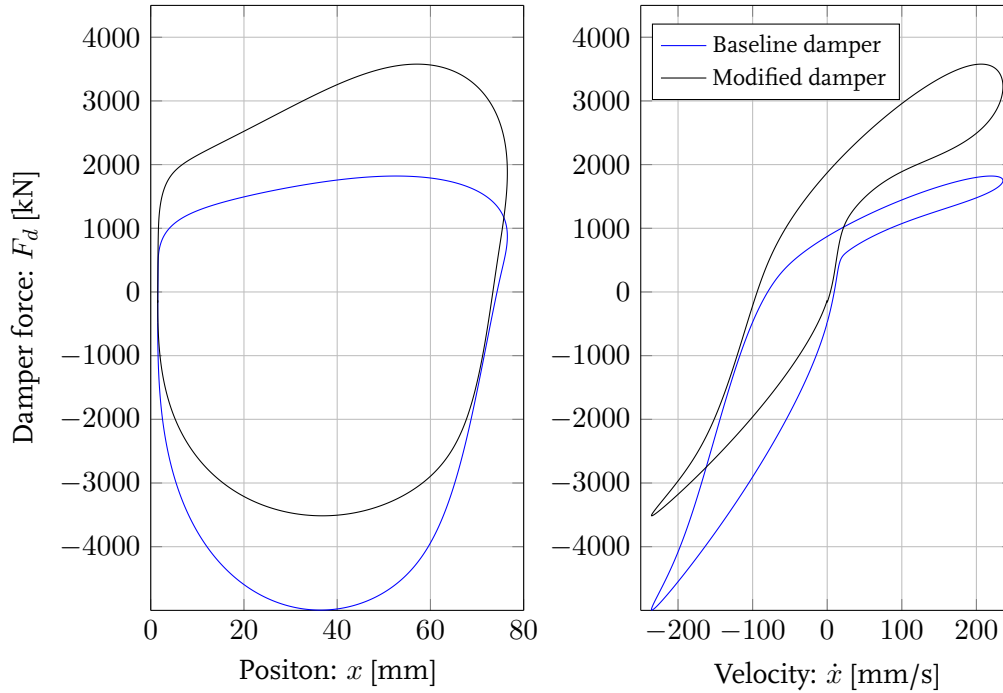
Figure 5.6: Damping characteristics of TFX Suspension Technology's mono-tube baseline damper (blue) and modified damper (black) to quantify the physical damper model's predictive quality

with $\bar{F}_{d,i}$ the measured damping force at time instance i and $\hat{F}_{d,i}$ the damping force calculated by the mono-tube model at the same i-th time instance.

Figure 5.7a displays the E_{NRMS} versus excitation frequency f for the baseline damper that has been used to obtain the model parameters in Section 5.2, Figure 5.7b displays this predictive quality measure for the modified damper. The first figure shows that the predictive model is capable of predicting damping forces within 6 percent accuracy for the baseline model over the main part of frequencies. The second figure shows that the predictive model is capable of predicting the damping force of the modified damper within 7 percent accuracy over the main part of frequencies.

Both figures show an increasing E_{NRMS}, i.e. a decreasing model predictive quality, for low frequencies at $f = 0.1$ Hz. This corresponds to an excitation velocity of $\dot{x} = 0.02$ m/s. The decreasing model predictive quality is explained by the fact that friction forces become more dominant at low velocities, which has also been stated by [4, 10, 11]. No friction model is included in the damper model that is derived in this study, which therefore yields larger predictive errors in this range. Including a friction model will enhance the predictive quality at low velocities.

For an example of the predictive quality with respect to calculating a damping characteristic of a shock absorber is referred to Figure 5.8. This figure shows the damper characteristics for the modified mono-tube damper, excited with 1 Hz for different settings of the bleed needle. The dashed lines indicate the damping force calculated by the physical model, the solid lines indicate the damping force measured with TU/e's damper test rig.

To further increase model predictive quality, Figure 5.2 should be considered. This figure shows that the measurement has a kind of sinusoidal wave running over the optimized prediction from $t = 0.25$ to $t = 0.7$ seconds that is not captured by the physical damper model. This sinusoidal wave has a frequency of approximately 5 Hz, indicating that some physical
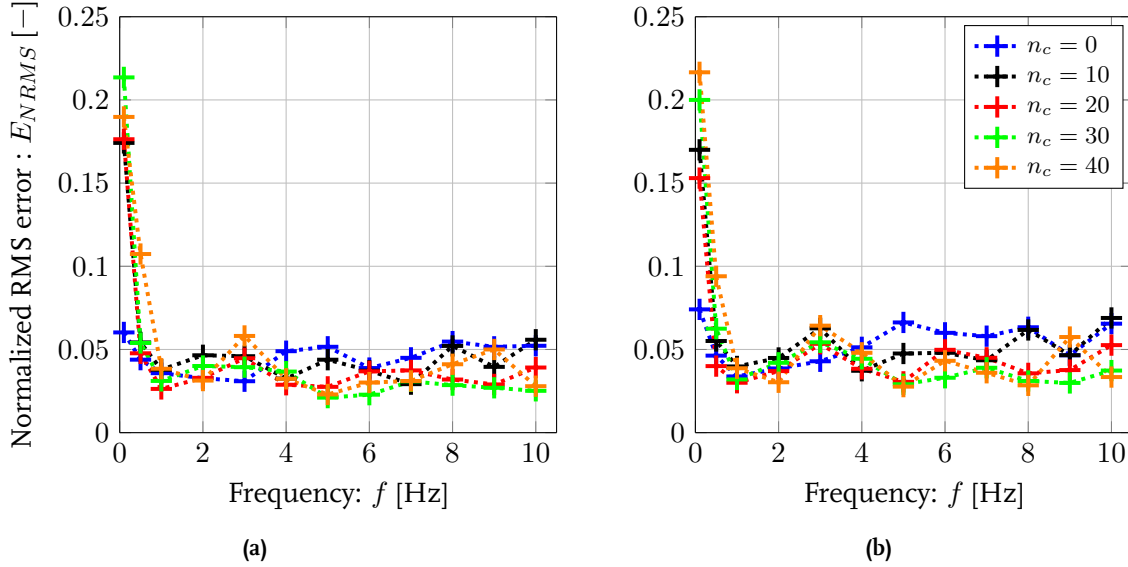
Figure 5.7: Normalized Root Mean Square error E_{NRMS} of the predictive damper model as function of excitation frequency f for **(a)** the shim stack used for model correlation **(b)** a modified shim stack, see Appendix E

phenomenon may have been omitted in the damper model. Research suggests that this phenomenon may be related to three possible causes, and are:

1. Water hammer effect described by Joukowsky's equation [26]:

$$\frac{\partial p}{\partial t} = \rho c \frac{\partial v}{\partial t} \tag{5.9}$$

2. A vibrational mode of the mono-tube cylinder [27]

3. Dynamics of the test rig affecting the measurement data

The first two causes relate to omitted behaviour in the damper model, the third possibility is caused by measurement disturbances caused by the dynamic behaviour of the test rig.

The water hammer effect, described by the Joukowsky equation (5.9), is caused when a valve is instantly closed downstream, i.e. at the outlet of the flow. Oil is still moving due to inertia, therefore building up pressure and a resulting shock wave. This shock wave is often observed in domestic plumbing where a loud banging or hammering noise is observed when quickly closing for instance a water tap. The pressure profile of this hammer pulse is described by Joukowsky's equation (5.9) with c the speed of sound in the fluid and v the fluid velocity. For instantaneously closing valves, the magnitude of the water hammer pulse reduces to $\Delta p = \rho c \Delta v$ propagating with a frequency $f = \frac{4L}{c}$ with L equal to the pipe length. Although the amplitude can be related to the missing phenomenon in Figure 5.2, the frequency of 1800 Hz for the mono-tube damper indicates that water hammer is not the cause for the missing effect.

A vibrational mode of the mono-tube shell may expand the compression- and rebound chamber, eventually causing the phenomenon observed from Figure 5.2. Leissa and Jinyoung [27] studied natural vibrational modes of such thin walled circular cylinders, stating that the vibrational modes for these type of thin-walled shells start above approximately 540 Hz. This disregards cylinder expansion as a cause for the missing effect.

A third cause for the existing wave may be found in the test rig that is used for measuring the damping behaviour of the mono-tube damper. An eigenfrequency of the rig might affect
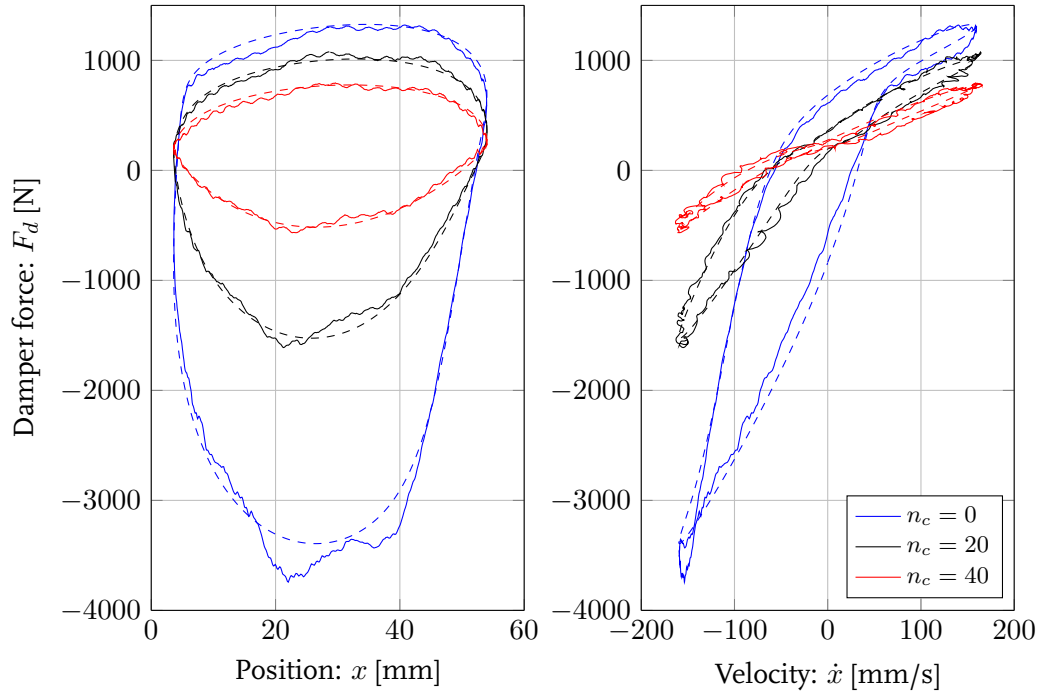
Figure 5.8: Damping characteristic of TFX Suspension Technology's mono-tube damper predicted with the physical damper model (dashed lines) and measured with TU/e's damper test rig (solid lines) for different settings of the bleed needle

measurement data. It is advised to measure these natural vibrational modes, for instance by exciting the set-up with a pulse hammer and measure its natural response. Other causes may be found in the control loop that actuate the test rig, or the hydraulics inside the test rig. The exact cause for these oscillations remain unclear.

5.4 Damper operation

The primary focus of this thesis is the derivation of a physical model that calculates the damper behaviour of TFX Suspension Technology's mono-tube damper. The model has been derived in Chapter 4, it relates the pressures in the rebound and compression chambers to the damper force. Subsequently, these pressures relate to the flow of oil between the two chambers, which in its turn relate to the opening of both the shim stack and bleed needle valves. The model takes all these phenomena into account and can be graphically displayed as function of damper excitation. To understand the working of the damper, all the previously described phenomena are calculated by the physical damper model and are graphically displayed in Figure 5.9. The damper is sinusoidally excited with 1 Hz, a closed bleed needle valve $n_c = 0$ and opened bleed needle valve are investigated. Calculations with the closed bleed needle are depicted with the solid lines, calculations with the open bleed needle valve $n_c = 40$ are depicted with dashed lines. The figure shows the pressures in the rebound and compression chamber, opening of the rebound and compression shim stacks, valve flow during compression and rebound and bleed flow during compression and rebound.

The most important observation is the upper left subplot that presents the pressures in the rebound and compression chambers. It shows that the pressure in the compression chamber is almost constant. On the other hand, the rebound chamber pressure varies significantly, and it is therefore the pressure in the rebound chamber that controls the damping force.

45

Furthermore, note that the rebound pressure drops significantly from 4.8 MPa to 0.4 MPa for a closed bleed orifice. If the initial gas charge $p_{gas,0}$ would be lower, pressure in the rebound chamber will approach zero.

Furthermore, note the large difference in rebound chamber pressures for a closed (solid line) and opened (dashed line) needle valve. These pressures significantly differ during rebound motion, thus negative velocities. Rebound chamber pressure during compression motion is less affected by the position of the bleed needle. Again, note that the pressure in the compression chamber is almost unaffected by the position of the bleed needle. Opening the bleed needle valve allows flow of fluid through this valve, in its turn reducing the flow of fluid through the shim stack valve. Note that a closed bleed bleed needle does not allow flow through the bleed orifices, but a fully open bleed needle still allows oil to flow through the shim stack valve.

The plots presented in Figure 5.9 are very suitable for TFX Suspension Technology to design a desired damping characteristic. The parameters in the model, such as initial nitrogen pre-load charge, gas chamber height, density of the hydraulic fluid and other dimensions such as orifice area's can be easily entered as input to the damper model. Figure 5.9 can be used to investigate the influences of modifying these parameters to damper behaviour.

5.5 Summary

A fourth order fixed-step Runge-Kutta scheme is used to solve the system of non-linear ordinary differential equations that describes the system to calculate damping response of the mono-tube damper. Variation of the stepsize and visually checking solution convergences yields a maximum stepsize of $h = 10^{-4}$ seconds to accurately solve the equations.

All parameters that describe the mono-tube damper model are provided by TFX Suspension Technology, except for four flow resistance coefficients that describe the flow of oil through the shim stack- and bleed needle valves during compression and rebound motion. A least-squares constrained parameter optimization algorithm has been introduced to estimate these four parameters. The optimization algorithm relates valve flow resistances to the Reynolds number of the flow through the piston orifices and opening of the shim stack. Bleed flow resistance relate to the Reynolds number through the bleed orifice and settings of the bleed needle valve.

The parameter optimization algorithm is divided in two stages. The first stage estimates the valve flow resistance coefficients based on measurements with a closed bleed needle, forcing al oil to flow through the shim stack valves. The standard shim stack is used to find the flow resistance coefficients.

The second parameter optimization stage determines the bleed flow resistance coefficients by taking the valve flow resistance coefficients obtained in stage one into account. Different settings of the bleed needle are evaluated in order to relate bleed flow resistance to the bleed needle position.

Section 5.3 presents an accuracy measure for the predictive quality of the mono-tube damper model. Predictive quality is represented as a normalized RMS error measure versus excitation frequency, indicating that the mono-tube model is capable of predicting damping forces within 7% accuracy in excess of 0.5 Hz. Frequencies below 0.5 Hz tend to show increasing errors, which is contributed to the fact that the damper model does not include a friction model. Friction forces tend to become more important when decreasing the excitation velocity, it is therefore recommended to include a friction model in the physical damper model to enhance model accuracy in this lower frequency range.

Damping behaviour tends to show oscillations when stroking the damper at constant ve-

locities. The physical damper model derived in Chapter 4 is not capable of predicting these oscillations, which may indicate that some phenomenon is disregarded during modelling of the damping behaviour. Three possible causes may be identified, which are the water hammer effect, described by the Joukowsky equation, vibrations of the mono-tube cylinder or vibrations of the test rig affecting the measurement data. The first two causes are proved to be invalid as natural frequencies do not match the behaviour observed in Figure 5.2, vibrational modes of the damper test rigs are unknown and it is recommended to measure these modes to verify whether these vibrations affect the measurement data.

Section 5.4 presents the basic operation of TFX Suspension Technology's damper. It shows that the pressure in the compression chamber is almost constant and is hardly affected by the setting of the bleed needle valve. In contradiction to the compression chamber pressure, the pressure in the rebound chamber varies significantly, from which is concluded that damper force is controlled by the pressure in the rebound chamber.
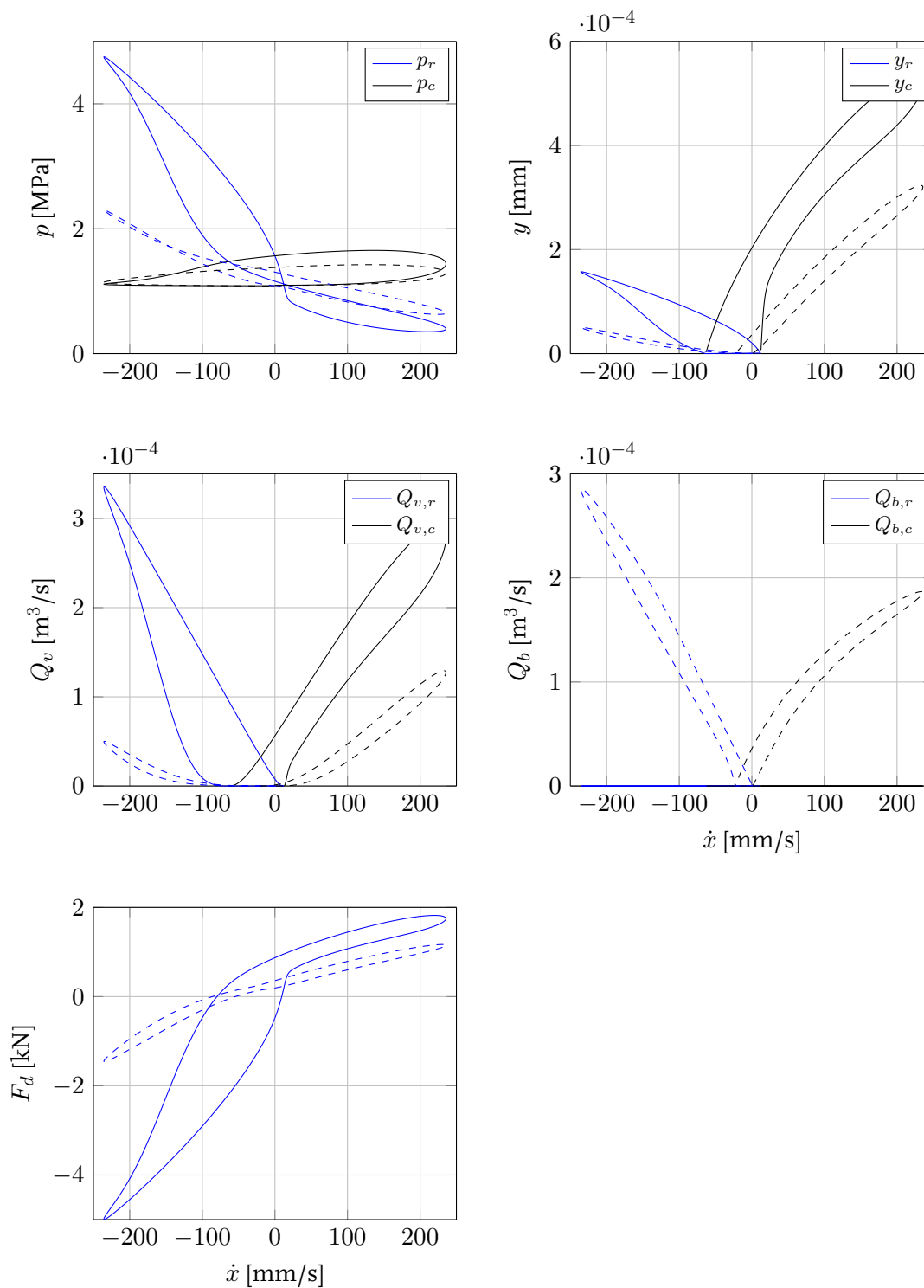
Figure 5.9: Pressures, shim stack tip deflection, shim stack valve flow, bleed needle valve flow and damper force predicted by the physical damper model for a closed $n_c = 0$ bleed needle valve (solid lines) and an opened $n_c = 40$ bleed needle valve (dashed line)

Chapter 6

Half motorbike application

A physical damper model to calculate damping forces has been derived in Chapter 4 and has been parametrized in Chapter 5. This section aims to evaluate the effects of using this damper model in comparison to traditional damper models, such as a linear- or look-up table damper. A half motorbike model, similar to the quarter car model, is introduced to predict a motorbike's vertical dynamics in Section 6.2. This section proceeds with a mathematical description of road conditions, damper models for vehicle simulations and performance measures to evaluate these damper models are introduced as well. Section 6.3 discusses the simulation results.

6.1   BMW R1200 GS Adventure

The hydraulic damper that has been provided by TFX Suspension Technology fits a BMW R1200 GS Adventure [28], which is one of the two configurations in the BMW GS family. The GS is an abbreviation of Gëlande/Straße (German: off-road/road), which refers to the fact that the BMW GS family is designed as a dual-application motorcycle: it can be used for both on-road as off-road touring. The GS motorcycles can be distinguished from other types by their longer suspension travel, its upright riding position and larger front wheel (typically 19 or 21 inch). The weight distribution is known to be $40/60$, the maximum permitted mass is specified to be 450 kg. TFX Suspension Technology's hydraulic damper is customized to provide a high level of comfort and road handling, both during poor off-road as well as smooth-asphalt on-road conditions and is delivered with a parallel linear spring. The hydraulic damper is discussed in detail in this thesis, the linear spring constant is in the order of 150 kN/m. Other technical data for the BMW R1200 GS Adventure is listed in Table 6.1.

6.2   Equations of motion of the half motorbike model

A common approach to study vertical dynamics is by analysing quarter car models. These type of models can be considered as representative for the vertical dynamic behaviour of cars, for instance to asses vertical accelerations observed by the driver or tire compression to assess road holding. The installation ratio that BMW uses in their para-lever swing-arm rear suspension yields much stiffer dampers than dampers that are typically used in car suspensions, for instance in wishbone suspension configurations. It is therefore not appropriate to use a quarter car model. A half motorbike model, similar to a quarter car model, is therefore derived.

Figure 6.1: BMW R1200 GS Adventure (2015 model)

Table 6.1: Data of the BMW R1200 GS Adventure motorcycle

Parameter	Value	Unit
Dry vehicle mass	223	[kg]
Permitted total mass	450	[kg]
Rear unsprung mass	23.3	[kg]
Front unsprung mass	16.2	[kg]
Weight distribution (front-rear)	$40 - 60$	$[-]$
Rear spring stiffness	150	[kN/m]
Maximum suspension stroke (front)	176	[mm]
Maximum suspension stroke (rear)	78	[mm]

The half motorbike model represents, as its name suggests, one half of a motorbike and is used to address vertical dynamic behaviour of motorcycles. The BMW GS family makes use of BMW's para-lever rear-suspension, see Figure 6.2. The hinge point of the para-lever suspension is not in the centre of the wheel, as depicted in the schematic representation in Figure 6.3a. This introduces some additional difficulties when modelling the vertical suspension, hence a simplistic swing-arm is used to model the BMW R1200 GS. This yields the schematic representation of the half motorbike as depicted in Figure 6.3b.

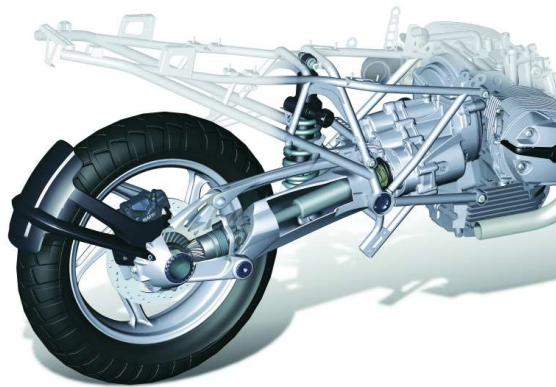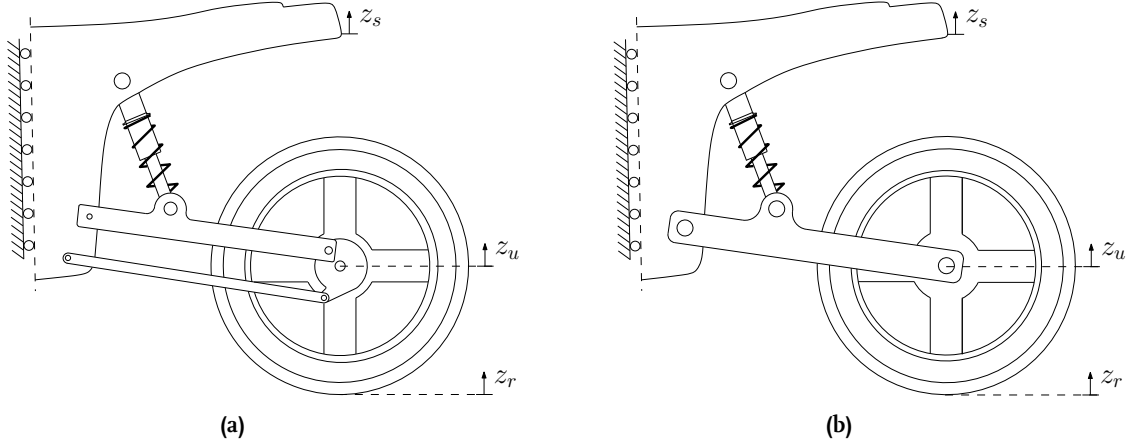**Figure 6.2:** BMW's R1200 GS para-lever rear suspension

Figure 6.4 shows the half motorbike model. It includes the unsprung mass m_u, which represents the sum of tire-, rim- and part of the suspension mass such as the swing-arm, and sprung mass m_s, which represents approximately half of the total motorbike mass minus unsprung masses. Tire and suspension stiffness are represented with k_t and k_s respectively.

Figure 6.3: Schematic representation of BMW's R1200 GS para-lever rear suspension (left) and a simplistic swing-arm model (right)
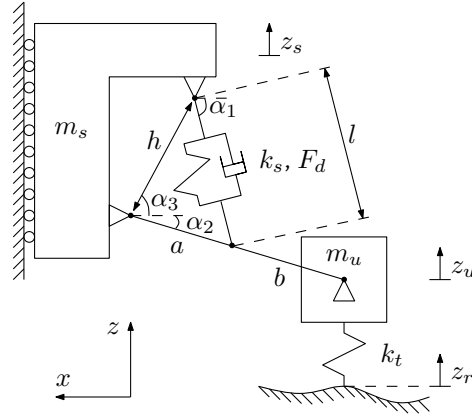
Figure 6.4: Half motorbike model to address vertical dynamic behaviour of motorcycles

The damping force is denoted with F_d which, for a linear damper with damping constant d_s, is substituted by $F_d = -d_s \dot{l}$, with damper length l. The road displacement z_r is prescribed, displacements of the sprung and unsprung mass, denoted with z_s and z_u respectively, are the two degrees of freedom. The equations of motion are derived using Lagrange's equations of motion [29]:

$$\frac{d}{dt}\left(T_{,\dot{q}}\right) - T_{,q} + V_{,q} = \left(Q^{nc}\right)^T \tag{6.1}$$

Equation (6.1) constitutes a set of scalar equations that describe the motion of a system as a function of the independent generalized coordinates q. T and V are the kinetic and potential energy of the system, Q^{nc} is the column of non-conservative forces, such as damping forces. The notation $T_{,q}$ is used to indicate the derivative of kinetic energy with respect to the generalized coordinates: $T_{,q} = \begin{bmatrix} \frac{dT}{dq_1} & \frac{dT}{dq_2} & \cdots & \frac{dT}{dq_{n-1}} & \frac{dT}{dq_n} \end{bmatrix}$.

There is only one choice for the generalized coordinates q to describe the whole system, which is the vertical displacement of the unsprung mass and the angle of the swing-arm, yielding: $q = \begin{bmatrix} q_1 & q_2 \end{bmatrix} = \begin{bmatrix} z_u & \alpha_2 \end{bmatrix}$. The kinetic energy T of the system becomes:

$$T = \frac{1}{2}m_u \dot{z}_u^2 + \frac{1}{2}m_s \left(\dot{z}_u + \dot{\alpha}_2 \left(a + b\right)\cos\left(\alpha_2\right)\right)^2 + \frac{1}{2}m_s \left(-\left(a + b\right)\dot{\alpha}_2 \sin\left(\alpha_2\right)\right)^2 \tag{6.2}$$

from which the horizontal and vertical velocity of the sprung mass, $\dot{x}_s = -\dot{\alpha}_2 (a + b) \sin(\alpha_2)$ and $\dot{z}_s = \dot{z}_u + \dot{\alpha}_2 (a + b) \cos(\alpha_2)$ respectively, are recognized. The potential energy V of the system becomes:

$$V = \frac{1}{2}k_t (z_r - z_u)^2 + \frac{1}{2}k_s (l_0 - l)^2 \tag{6.3}$$

Substituting $l = \sqrt{a^2 + h^2 - 2ah \cos(\alpha_2 + \alpha_3)}$ in the potential energy function yields:

$$V = \frac{1}{2}k_t (z_r - z_u)^2 + \frac{1}{2}k_s \left(l_0 - \sqrt{a^2 + h^2 - 2ah \cos(\alpha_2 + \alpha_3)}\right)^2 \tag{6.4}$$

The derivatives of the kinetic- and potential energy function with respect to the column of generalized coordinates yield:

$$T_{,\underline{q}} = \begin{bmatrix} 0 \\ -m_s \dot{z}_u \dot{\alpha}_2 (a + b) \sin(\alpha_2) \end{bmatrix}^T \tag{6.5}$$

$$T_{,\dot{\underline{q}}} = \begin{bmatrix} (m_u + m_s) \dot{z}_u + m_s \dot{\alpha}_2 (a + b) \cos(\alpha_2) \\ m_s (a + b)^2 \dot{\alpha}_2 + m_s \dot{z}_u (a + b) \cos(\alpha_2) \end{bmatrix}^T \tag{6.6}$$

$$\frac{d}{dt}\left(T_{,\dot{\underline{q}}}\right) = \begin{bmatrix} (m_u + m_s) \ddot{z}_u + m_s \ddot{\alpha}_2 (a + b) \cos(\alpha_2) - m_s \dot{\alpha}_2^2 (a + b) \sin(\alpha_2) \\ m_s (a + b)^2 \ddot{\alpha}_2 + m_s \ddot{z}_u (a + b) \cos(\alpha_2) - m_s \dot{z}_u \dot{\alpha}_2 (a + b) \sin(\alpha_2) \end{bmatrix}^T \tag{6.7}$$

$$V_{,\underline{q}} = \begin{bmatrix} -k_t (z_r - z_u) \\ -\frac{ahk_s \sin(\alpha_2 + \alpha_3)(l_0 - l)}{l} \end{bmatrix}^T \tag{6.8}$$

The column of non-conservative forces ($\underline{Q}^{nc}$) follows from the principle of virtual work of non-conservative forces:

$$\underline{Q}^{nc} = \sum_{i=1}^{n} \left(\underline{r}_{i,\underline{q}}\right)^T \underline{F}_i^{nc} \tag{6.9}$$

with n the number of non-conservative forces and $\underline{r}_i$ the vector of the point at which the non-conservative force $\underline{F}_i^{nc}$ is exerted. Two non-conservative forces act in the system of Figure 6.4, which are the two damping forces: one exerted at the sprung mass and one exerted at the swing arm, denoted with F_{d1} and F_{d2} respectively:

$$F_{d1} = -F_{d2} = \begin{bmatrix} F_d \cos(\alpha_1) \\ 0 \\ F_d \sin(\alpha_1) \end{bmatrix} \tag{6.10}$$

with $\alpha_1 = \alpha_2 + \arcsin\left(\frac{h}{l}\sin(\alpha_2 + \alpha_3)\right)$. The position vectors of these damping forces are:

$$\underline{r}_{d1} = \begin{bmatrix} (a + b) \cos(\alpha_2) - h \cos(\alpha_3) \\ 0 \\ z_u + (a + b) \sin(\alpha_2) + h \sin(\alpha_3) \end{bmatrix} \tag{6.11}$$

and

$$\underline{r}_{d2} = \begin{bmatrix} b\cos\alpha_2 \\ 0 \\ zu + b\sin(\alpha_2) \end{bmatrix} \tag{6.12}$$

The derivatives of these position vectors with respect to the column of generalized coordinates yield:

$$\underline{r}_{d1,\underline{q}} = \begin{bmatrix} 0 & -(a+b)\sin(\alpha_2) \\ 0 & 0 \\ 1 & (a+b)\cos(\alpha_2) \end{bmatrix} \tag{6.13}$$

and

$$\underline{r}_{d2,\underline{q}} = \begin{bmatrix} 0 & -b\sin(\alpha_2) \\ 0 & 0 \\ 1 & b\cos(\alpha_2) \end{bmatrix} \tag{6.14}$$

Substituting (6.10), (6.13) and (6.14) in (6.9) yields the column of generalized non-conservative forces:

$$\underline{Q}^{nc} = \begin{bmatrix} 0 \\ aF_d\sin(\alpha_1 - \alpha_2) \end{bmatrix} \tag{6.15}$$

Combining (6.1), (6.5), (6.7), (6.8) and (6.15) yield two scalar equations describing the non-linear dynamics of the half motorbike model:

$$(m_u + m_s)\ddot{z}_u + m_s\ddot{\alpha}_2(a+b)\cos(\alpha_2) - m_s\dot{\alpha}_2^2(a+b)\sin(\alpha_2) - k_t(z_r - z_u) = 0 \tag{6.16}$$

$$m_s\ddot{\alpha}_2(a+b)^2 + m_s\ddot{z}_u(a+b)\cos(\alpha_2) = \\ \frac{ahk_s\sin(\alpha_2 + \alpha_3)(l_0 - l)}{l} + aF_d\sin(\alpha_1 - \alpha_2) \tag{6.17}$$

The sprung mass acceleration follows from:

$$\ddot{z}_s = \ddot{z}_u + \ddot{\alpha}_2(a+b)\cos(\alpha_2) - \dot{\alpha}_2^2(a+b)\sin(\alpha_2) \tag{6.18}$$

The parameters of a BMW R1200 are used in the model and are listed in Table 6.2. The vertical tyre-stiffness is obtained from a Delft-Tyre motorcycle tyre property file as the vertical tyre stiffness for this particular motorcycle is unknown. The next subsections introduce road disturbances, performance measures to quantify the different damper models and commonly used damper models to describe damper behaviour.

Table 6.2: Suspension variables of the BMW R1200 GS Adventure motorcycle

Parameter	Value	Unit
a	225	[mm]
b	365	[mm]
h	281	[mm]
$\alpha_{2,0}$	15	[deg.]
α_3	80	[deg.]
k_s	150	[kN/m]
k_t	170	[kN/m]
m_s	246.7	[kg]
m_u	23.3	[kg]

6.2.1 Road disturbances

A vehicle is subjected to road irregularities while driving and two types of irregularities can be identified: stochastic (random) irregularities and deterministic disturbances. Stochastic irregularities describe normal driving conditions, such as continuous random vibrations due to road profile irregularities and can be regarded as having a long or even infinite duration. Deterministic disturbances are mostly related to single events of short duration such as speed bumps, rail road crossings and potholes. This study assumes a speed bump deterministic disturbance as depicted in Figure 6.5.
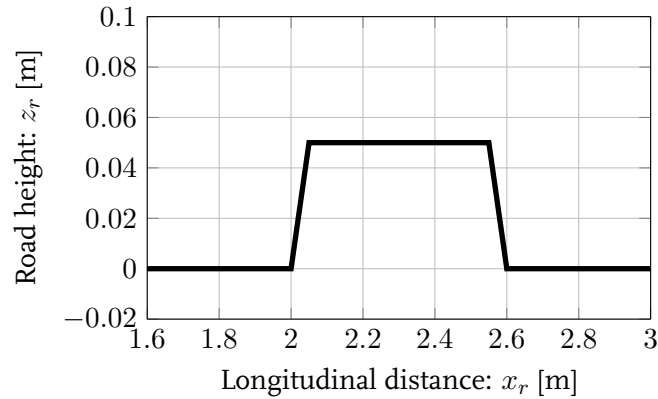
Figure 6.5: Deterministic road disturbance

A representation of stochastic road irregularities is required in order to predict vehicle responses to road excitation. Random noise can be integrated to create a synthetic road profile. Besselink [30] proposed a simple method to create a random road profile. The discretized road profile describes road height z_r at point i at longitudinal distance x_r at the same point i, referred to as $z_r(i)$ and $x_r(i)$ respectively. The road height at point $i + 1$ follows from

$$z_r(i + 1) = z_r(i) + Z \cdot \text{rand}(-1, 1) \tag{6.19}$$

with $\text{rand}(-1, 1)$ a random number function generating uniformly distributed numbers between -1 and 1. This method is schematically depicted in Figure 6.6. Amplitude Z depends on road surface type and longitudinal increment $\Delta x_r = 0.01$ meter. Road classification ISO 8608 [31] describes these road surface types and proposes an expression to represent road classification by means of road displacement power spectral density, see Figure 6.7. Road

class A is classified as a very good and smooth road, road class E is a very poor road and road class H is classified as even poorer.
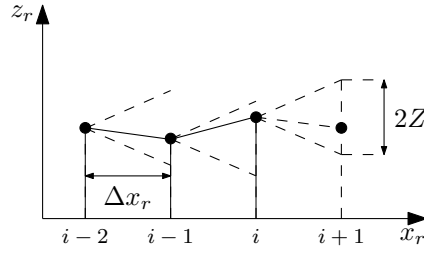
Figure 6.6: Mathematical description of stochastic synthetic road profile by Besselink [30]
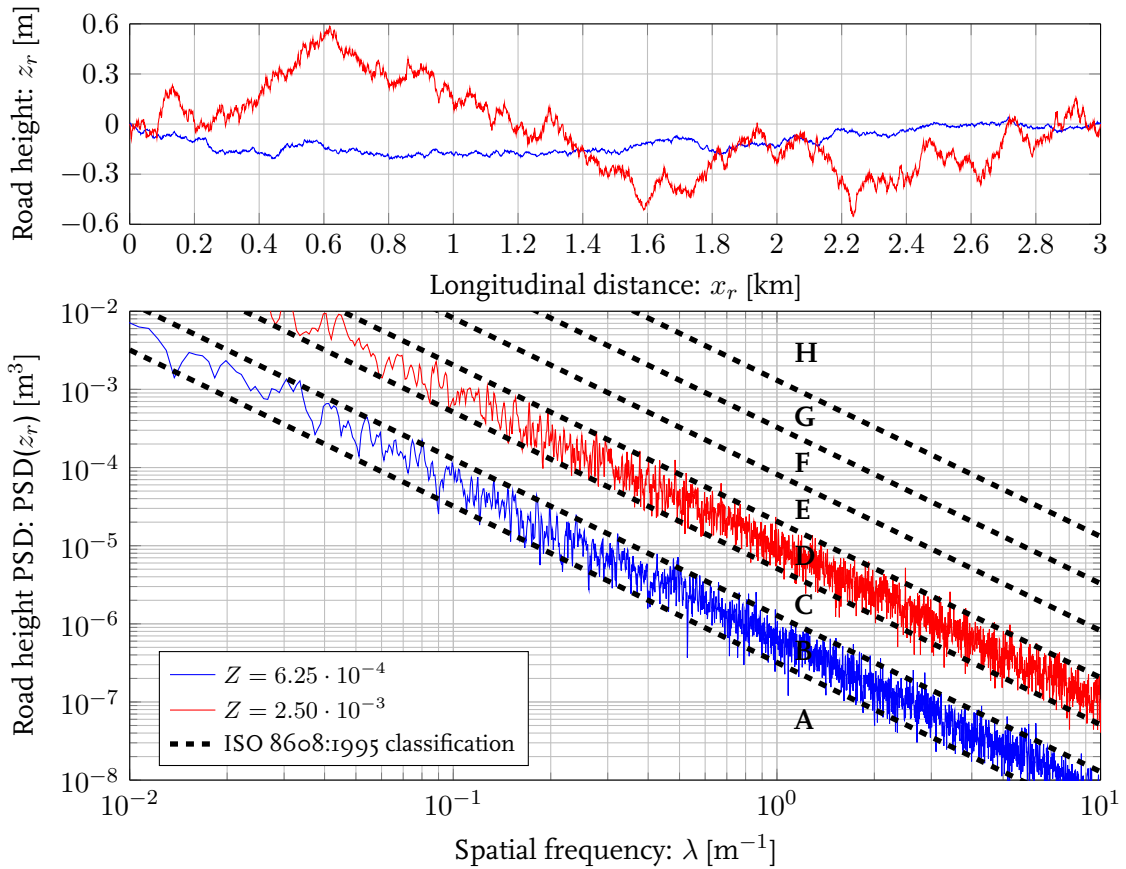
Figure 6.7: Power spectral densities of the ISO 8608:1995 road classes and the stochastic B-class (blue, good road) and D-class (red, poor road) road profile

6.2.2 Damper models for vehicle simulations

Two different damper models are commonly used when evaluating vertical dynamics of a vehicle and in this case thus the half motorbike model. The first model uses of a look-up table that links damping force to shock absorber compression- and rebound velocity. This look-up table will be generated from simulations with the physical damper model as discussed earlier, where the shock absorber is sinusoidally excited over its maximum allowable stroke. Different excitation velocities are obtained by varying the excitation frequency in the range from 0.1 to 2.5 Hz. The damping force is extracted at the peak velocities. This method is known as PVP damper-curve reconstruction and is described in Section 2.2.2. The resulting PVP-curve is presented in Figure 6.8.

A second commonly used damper model is the linear damper model. This model makes use of an equivalent linear damping constant that is derived from the damper's dissipated energy. The dissipated energy W follows from the integral of measured damper force F_d during a measurement over damper extension dl:

$$W = \int F_d dl \qquad (6.20)$$

Introducing the equivalent linear damping constant that relates damper compression velocity to damper force $F_d = d_s \dot{l}$ and recalling $dl = \dot{l} dt$ yields:

$$W = d_s \int \dot{l}^2 dt \qquad (6.21)$$

from which the damping constant d_s is obtained. For the purpose of this study it is decided to asses the dissipated energy from simulations with the physical damper model on a B-class road, which yields the equivalent damping constant $d_s = 4.34$ [kN·s/m], see Figure 6.8.
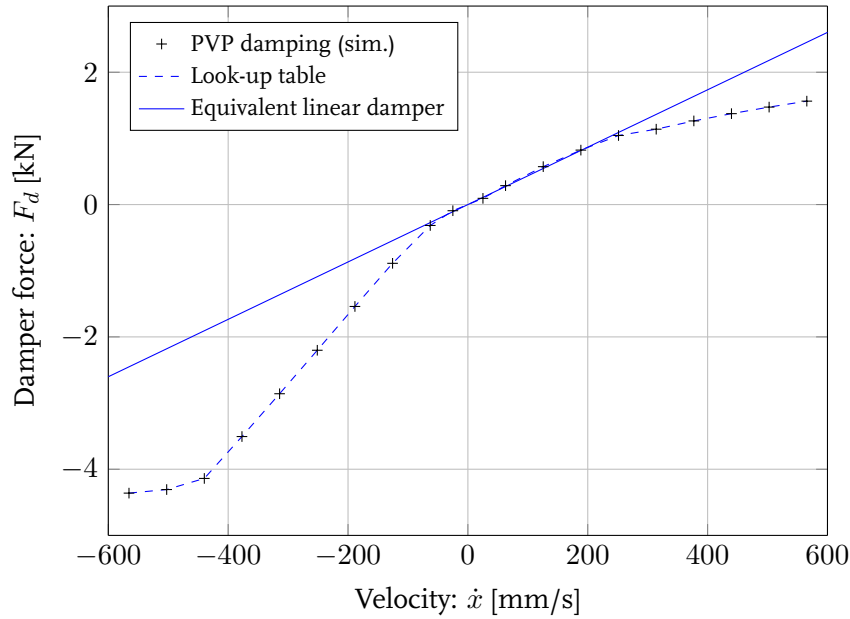
Figure 6.8: Look-up table damping constructed from PVP simulations (blue-dashed) and equivalent linear damper from B-class road simulations (blue-solid, $d_s = 4.34$ [kN·s/m])

6.2.3 Performance measures

An equivalent linear damper and velocity dependent non-linear look-up table damper have been introduced in Section 6.2.2. Measures to evaluate these models are introduced in this subsection. The vertical acceleration of the sprung mass $\ddot{z}_s$ is a good indicator to quantify ride comfort. Humans are more sensitive for vertical accelerations between 4 and 10 Hz, hence the ISO 2631-1 weighting criterion [32] is taken into account. Figure 6.9 shows this weighting criterion as function of the vertical acceleration frequency, which indicate the sensitiveness in the 4 to 10 Hz range and its fast decreasing sensitivity outside this range. Zuo et al. [33] converted the ISO 2631-1 weighting criterion to a fifth-order continuous time transfer function as displayed in Figure 6.9. This fifth-order fit is used to approximate the ISO 2631-1 weighting

criterion to obtain the weighted sprung acceleration $\ddot{z}_{sw}(s) = W_{\ddot{z}_s}(s)\ddot{z}_s(s)$ and is expressed as:

$$W_{\ddot{z}_s}(s) = \frac{87.72s^4 + 1138s^3 + 11336s^2 + 5453s + 5509}{s^5 + 92.69s^4 + 2549.83s^3 + 25969s^2 + 81057s + 79783} \tag{6.22}$$
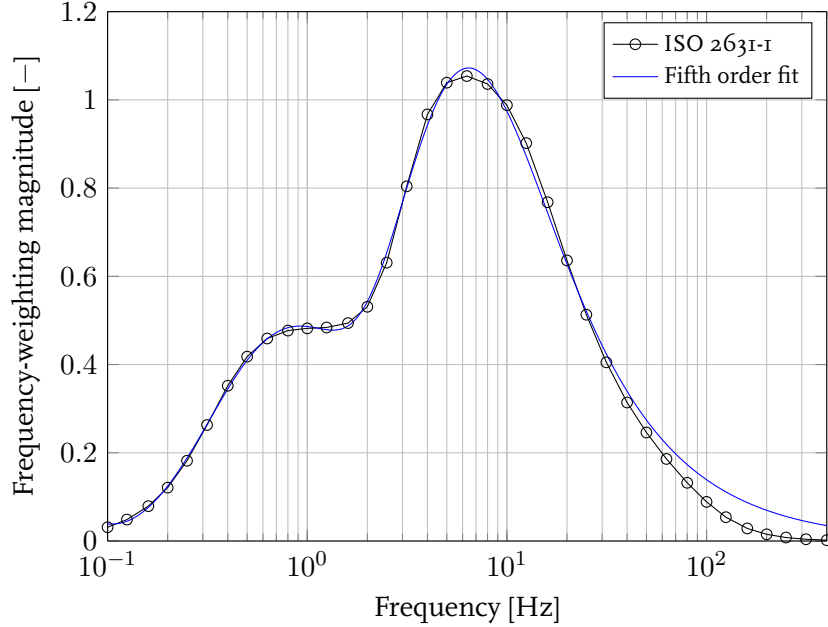

Figure 6.9: Continuous time fit of the ISO 2631-1 vertical acceleration weighting criterion by Zuo [33]

Tire compression variations are a good indicator to quantify the vehicle's road holding. Tyre compression equals the difference between road displacement and unsprung mass-displacement: $z_t = z_r - z_u$. The suspension stroke provides necessary space for the suspension system, and equals the difference between the maximum and minimum damper length: $\Delta l = l_{max} - l_{min}$.

6.2.4 Solution algorithm

The non-linear system described by (6.16) and (6.17) describe the vertical dynamics of the half motorbike model. A fourth order Runge-Kutta scheme described by Heath [25] is used to solve the system of differential equations. Selecting the fixed stepsize is done by visually checking the solution to converge, as previously described in Section 5.1. A stepsize of $h = 10^{-3}$ seconds seems appropriate to solve look-up table- and linear damped simulations. However, Section 5.1 demonstrates that this stepsize does not yield converged solutions when calculating damping force with the mono-tube physical model. A solution is found in decreasing the stepsize from $h = 10^{-3}$ to $h = 10^{-4}$ seconds when performing simulations with the physical damper model, which unfortunately increases computational costs.

6.3 Simulation results

A BMW R1200 GS Adventure motorbike is used to parametrize the half motorbike model derived in Section 6.2, two different methods that are commonly used to model dampers are introduced in Section 6.2.2, in addition the physical model will be evaluated. The influence of these different damper models on the simulations results is discussed in this section. Stochastic road disturbances are first discussed, followed by deterministic disturbances.

6.3.1   Stochastic road disturbances

Tables 6.3 and 6.4 show the RMS sprung accelerations $\ddot{z}_s$, RMS weighted sprung accelerations $\ddot{z}_{sw}$, maximum suspension stroke Δl and RMS tyre compression z_t of the half motorbike model under random road excitation of a B-class good road and D-class poor road for three damper models. Both tables show the same tendency: the physics based damper model predicts lower weighted sprung accelerations, suspension stroke and tire compression compared to the look-up table or linear damper model, both during good road - as well as poor road conditions. Furthermore, the look-up table model shows better correspondence to the physical model with respect to the unweighted sprung acceleration, suspension stroke and tire compression in comparison to the linear damper model. This tendency may be explained by the fact that the look-up table provides a more accurate description of damping behaviour than a linear damper does.

In contradiction to this, when evaluating the RMS weighted sprung accelerations in Tables 6.3 and 6.4, it is observed that linear dampers match the physics based predictions closer in comparison to look-up damper models. This is remarkable since the look-up table show better resemblance to the physical model with respect to unweighted accelerations. This observation can only be contributed to the influence of the ISO 2631-1 weighting filter, apparently having a significant weighting factor in these ranges where the linear damper results correspond better to the physical damper results, thus disregarding the ranges where look-up tables resemble to the physical model.

Furthermore, the weighted sprung accelerations of the physics based model differ up to thirteen percent in comparison to the commonly used look-up table damping models on a poor road. Taking into account that humans can sense differences of approximately five percent weighted sprung acceleration, makes implementation of a physics based damper model essential when predicting comfort levels.

Figure 6.10 shows the power spectral densities of the three performance criteria. The suspension bounce resonance frequency for the linear model and look-up table damper model are 1.1 Hz, the resonance frequency for the physical damper model is 1.3 Hz. Note the differences in magnitude at these resonance frequencies for the three different damper models. A second resonance peak at 13.7 Hz results from the wheel hop frequency, again yielding different magnitudes for the three damper models at this frequency.

Concerning weighted sprung mass accelerations, note the higher power spectral density of the physics based model compared to linear and look-up table damping in the very low 0.1 to 0.3 Hz and 1.3 to 10 frequency range. This indicates that the physics based model predicts higher sprung mass accelerations in this range. In contradiction to this, the physics based model clearly shows lower weighted sprung mass acceleration PSD compared to the other two models in the 0.3 to 1.3 Hz and 10 to 100 Hz frequency range, indicating that this model predicts lower sprung mass accelerations in this frequency range.

The suspension travel PSD of the physics based model has, similar to weighted sprung mass accelerations, a higher magnitude in the very low 0.1 to 0.3 Hz frequency range. This indicates that the physics based model is less damped for very low velocities compared to the other two damper models. From 0.3 Hz to the first resonance frequency at 1.3 Hz, the physical model predicts less suspension travel in comparison to the other models. The three models closely match in the remaining frequency range, except for the wheel hop frequency at 13.7 Hz.

Similar to the weighted sprung mass acceleration, the physical damper model predicts more tire compression in the very low 0.1 to 0.2 Hz and 1.3 to 10 Hz frequency range. It closely matches the other two damper models at remaining frequencies.

Table 6.3: Simulation results of the B-class good road, $V_x = 50$ [km/h]

Parameter	Linear damper	Look-up table	Physical model
RMS sprung acceleration: $\text{RMS}(\ddot{z}_s)$ [m/s²]	0.52	0.53	0.56
RMS weighted sprung acceleration: $\text{RMS}(\ddot{z}_{sw})$ [m/s²]	0.34	0.35	0.33
Maximum suspension stroke: Δl [mm]	16.95	15.79	15.58
RMS tire compression: $\text{RMS}(z_t)$ [mm]	2.29	2.13	2.09
Calculation time [s]	880	926	958

Table 6.4: Simulation results of the D-class poor road, $V_x = 30$ [km/h]

Parameter	Linear damper	Look-up table	Physical model
RMS sprung acceleration: $\text{RMS}(\ddot{z}_s)$ [m/s²]	1.61	1.59	1.44
RMS weighted sprung acceleration: $\text{RMS}(\ddot{z}_{sw})$ [m/s²]	1.03	1.13	1.00
Maximum suspension stroke: Δl [mm]	54.71	46.55	41.66
RMS tire compression: $\text{RMS}(z_t)$ [mm]	7.59	6.16	5.92

6.3.2 Deterministic road disturbances

Figure 6.11 shows the sprung mass acceleration and damper force of the half motorbike model driving over a speed bump as introduced in Section 6.2.1 and illustrated by Figure 6.5. Tire enveloping behaviour is not taken into account for simplicity reasons. Figure 6.11 shows that during damper compression from $t = 1$ to $t = 1.5$ seconds, the linear damper is a better resemblance to the physical damper model concerning sprung mass accelerations, which is also confirmed by the generated damping force depicted in the lower sub-plot. In contradiction to this, extending the damper starting at $t = 1.6$ seconds, the look-up table model gives better resemblances, although slightly phase-shifted, to sprung mass accelerations predicted by the physical damper model, which is also confirmed from the damping force plot. The latter observations may be explained from Figure 6.8, depicting the linear damper and look-up table damper, indicating that the linear damper is a good representation of look-up table measurements during compression, but differs significantly from the look-up table damper model during damper extension.

The phase-shift of the sprung mass accelerations is attributed to hysteric effects that are typical for hydraulic dampers. This hysteric effect is captured by the physical damper model, but is not captured by the linear- and look up table damper models.

6.4 Summary

This chapter evaluates the benefits of using the physical damper model that has been derived in Chapter 4 over using conventional damper models such as a look-up table or linear dampers. The hydraulic damper provided by TFX Suspension Technology fits a BMW motorbike. The swing-arm of the motorbike introduces a lever effect, making motorbike dampers much stiffer than dampers used in cars. A half motorbike model, similar to a quarter car model, is derived to predict the vertical dynamics of a motorbike.

Performance measures to evaluate the three damper models are selected. Tire compression is a good indicator to quantify road holding, suspension travel indicates the necessary suspension space. Vertical accelerations of the sprung mass are also considered in combination with the ISO 2631-1 human sensitivity filter. A deterministic speed bump disturbance and stochastic B-class good - and D-class poor roads are used as inputs to the model.

Simulation results with the half motorbike model show that the physical damper model

predicts less suspension travel and less RMS tire compression in comparison to linear- and look up table dampers for both the B-class and D-class road. The look-up table damper model shows a better resemblance to the physics based model. Although the RMS weighted sprung acceleration predicted by the linear damper approximates predictions resulting from the physical model, its predicted non-weighted accelerations differ significant. Moreover, the look-up table damper model show the better resemblance to the physical model prediction regarding the non-weighted accelerations.

The deterministic disturbance is a speed bump of 50 mm in height. Simulation results show that the linear damper is able to closely match to the physical damper model during compression stage, but fails to give an accurate representation during damper extension. It is the look-up table damper that closely matches physical damper simulation results during damper extension, however prediction results seem phase-shifted, which may be attributed to the hysteric effects that is typical for hydraulic dampers.

The most important conclusion of this chapter is the observation that weighted sprung mass accelerations predicted by the physical damper model differ up to thirteen percent in comparison to the commonly used look-up table damping models on a poor road. Humans can sense differences of approximately five percent weighted sprung acceleration, making the implementation of a physics based damper model essential when predicting comfort levels.
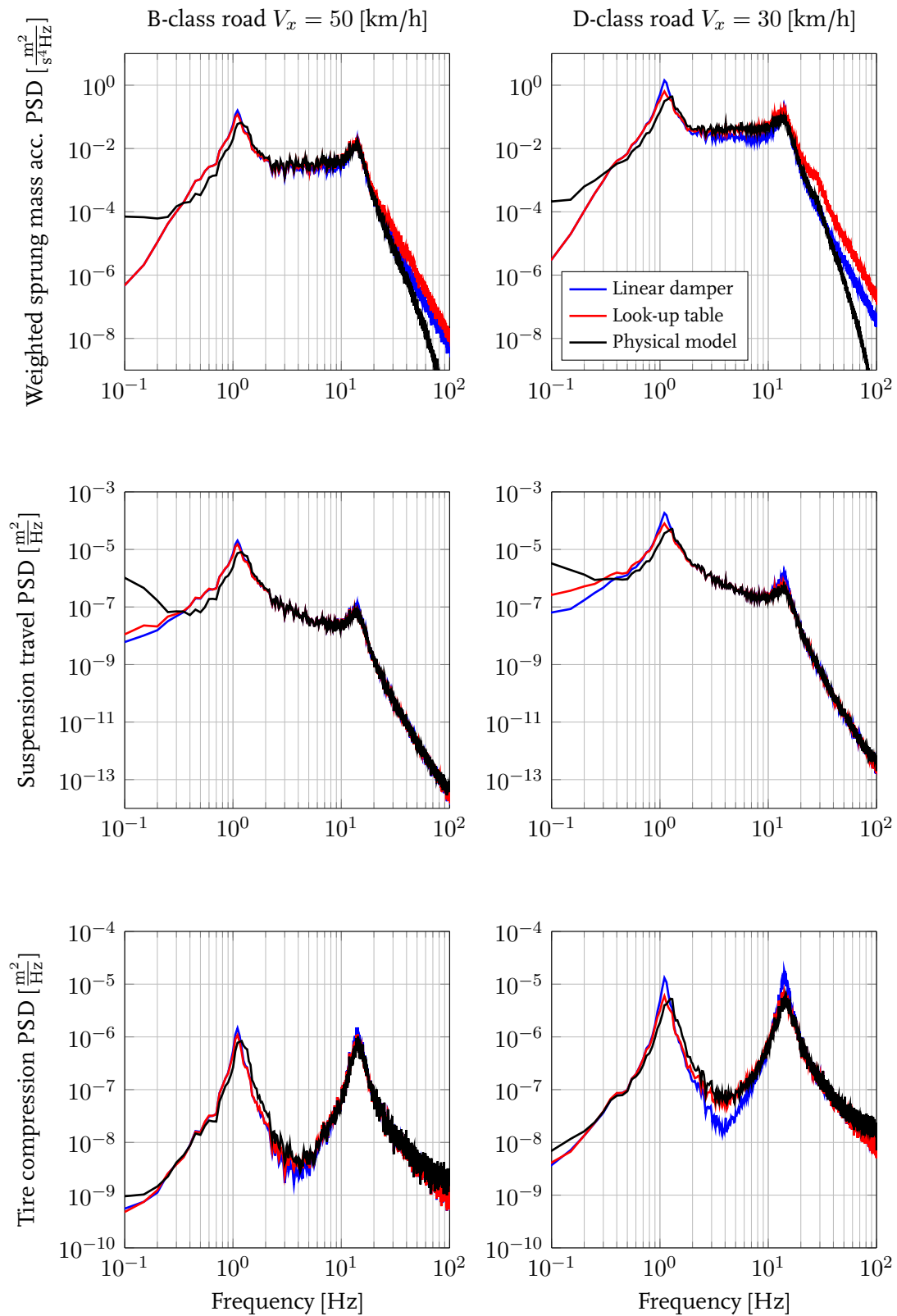
Figure 6.10: Power spectral densities of the sprung mass acceleration, suspension travel and tire compression for both a B-class and D-class road
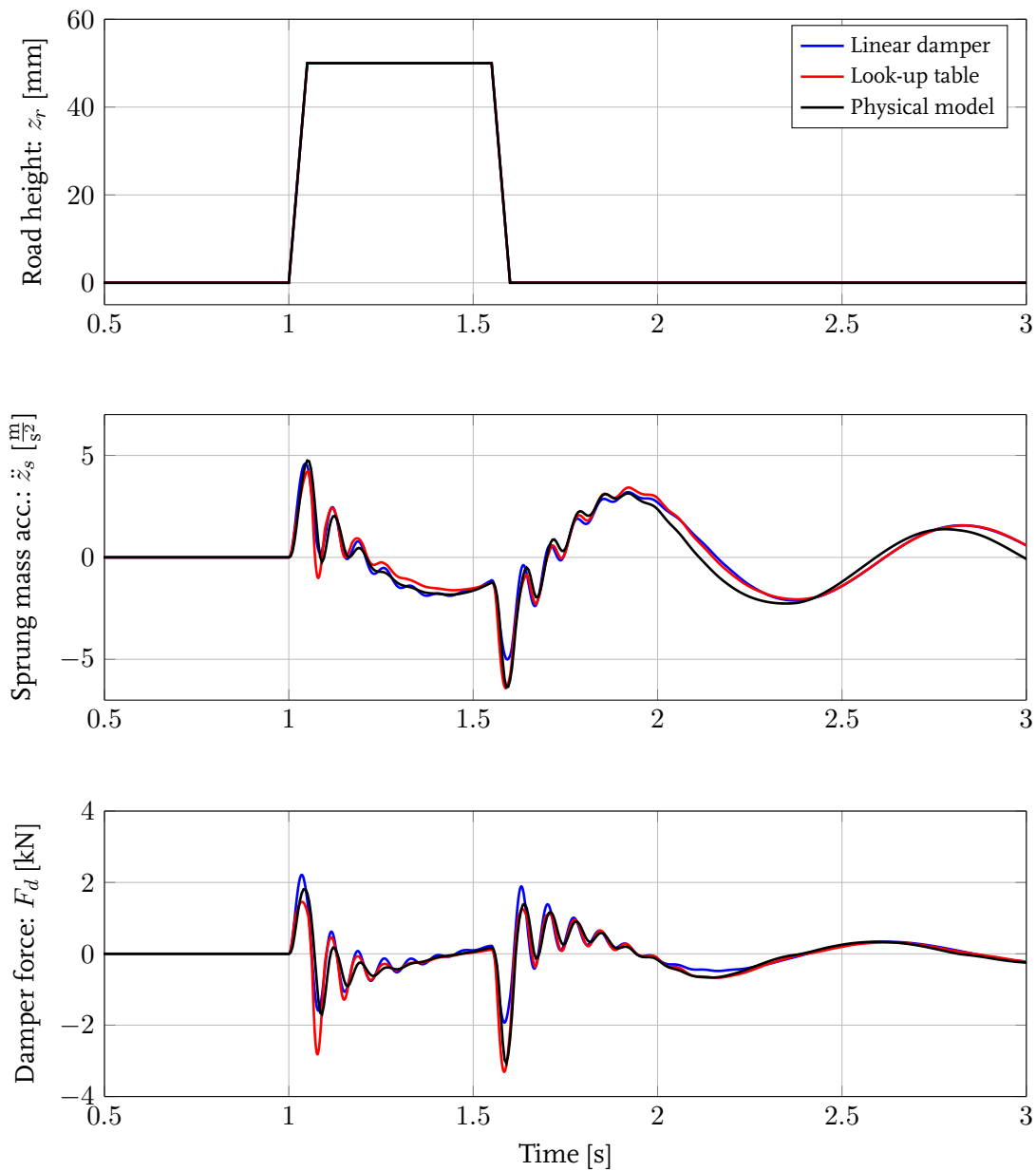
Figure 6.11: Results of the sprung mass acceleration and damping force for deterministic road disturbance simulations

Chapter 7

Conclusions and recommendations

This study discusses the derivation of a physical damper model of a mono-tube damper. The aim is to accurately measure damper characteristics with the help of TU/e's hydraulically actuated shock absorber test rig and to model this behaviour in terms of force as function of damper velocity and other factors that have an influence. This chapter draws conclusions from the conducted research and formulates recommendations for future research.

7.1 Conclusions

TU/e's hydraulically actuated damper test rig
A hydraulically actuated damper test rig has been developed to measure damping characteristics. In this study a Graphical User Interface (GUI) is designed to enhance user-friendliness of the test rig, additionally making the rig more suitable for 'production' work. Some automatic safety measures to prevent the operator from injuries while testing are implemented, as well as some checks to ensure correct test execution. Operation- and safety procedures are documented as well.

An approach to reduce high-frequent measurement noise from the load cell that measures damper force has been designed. This implies the design of a low-pass zero-phase Butterworth filter. Cut-off frequency residual analysis demonstrates that a cut-off frequency of 220 Hz is appropriate. Measurement noise that eventually passes through the Butterworth filter is reduced by a time-domain cycle averaging method. 30 cycle averages seems to be appropriate as more cycle averages does not significantly improve measurement results and additionally might warm up the damper which may affect the damper force.

Physical damper model
The aim of this thesis is to accurately model damping characteristics of TFX Suspension Technology's mono-tube damper. The main conclusion of this research is that a predictive damper model of a mono-tube damper has been developed, incorporating all major internal physical phenomena to accurately predict damping forces. The model assumes incompressible flow through the valve orifices, but compressible fluid in the chambers. Leakage across the piston is neglected, friction forces are not taken into account as literature state these are small compared to damper force. This claim turns out to be only valid above 0.5 Hz excitation frequency, a friction model should be included in the damper model during future research.

The model predicts damping characteristics as function of damper excitation, internal geome-

tries and specifications of the oil and nitrogen gas in the damper. Damper force is predicted within 7 percent accuracy for excitation frequencies in excess of 0.5 Hz. Friction forces tend to dominate damping force below 0.5 Hz, therefore yielding larger prediction errors below 0.5 Hz.

A force model relates pressures in the mono-tube damper to its resulting damper force. Derivation of a flow model, relating flow of oil to changes in chamber pressure and chamber volume, follows from the general expression of mass conservation in integral form. The model yields a system of two non-linear differential equations that describe the time derivatives of the two pressures acting in the two chambers inside the damper. A fourth-order Runge-Kutta scheme is used to solve the system of differential equations. Furthermore, the model calculates flow of oil through both the shim stack valve and bleed needle valve. It accounts from shim stack opening as function of shim stack composition, the externally adjustable bleed needle valve is taken into account as well. The model can be used to design a desired damper behaviour.

Most parameters that describe the model, such as dimensions and fluid properties, follow from data provided by TFX Suspension Technology. Four flow resistance coefficients that relate flow of fluid through the valves to pressure differences over these valve are obtained from a least-squares constrained parameter optimization algorithm. The model has been proved to cover a wide range damper settings, which include different shim stack compositions and externally adjustable bleed needle valve settings.

One insight from the physical damper model is that the pressure in the compression chamber is almost constant, damper force is therefore dominated by the pressure in the rebound chamber.

In this study a physical damper model has been developed, taking both compressibility of oil and a physical model to predict opening of shim stack valves into account. Furthermore, it is the first study in the field of damper modelling to the knowledge of the author, that relates flow resistance coefficients of orifices to viscous and component friction of the corresponding orifices.

Half motorbike application
The damper that is used as a baseline during this study fits a BMW R1200 GS motorbike. The installation ratio that BMW uses in their para-lever swing-arm configuration yields much stiffer dampers than dampers that are typically used in for instance wishbone suspension configurations in cars. A half motorbike model, similar to a quarter car model, is therefore derived to examine the benefits of using the physical damper model in comparison to existing models, such as look-up table or linear damper models. Performance measures are selected to be tire compression, suspension travel and ISO 2631-1 weighted sprung acceleration.

A deterministic speed bump and stochastic ISO 8608 B-class and D-class roads are used as inputs to the model. Simulation results show that the physical damper model tends to show less suspension travel, RMS tire compression and RMS weighted sprung acceleration in comparison to look-up table and linear damper models. A look-up table damper model is known to show better resemblance to real dampers and matches closer to physical damper results concerning RMS tire compression, suspension travel and un-weighted sprung acceleration. In contradiction, RMS weighted sprung acceleration predicted by the linear damper model gives better accordance to physical damper results, this observation is contributed to the influence of the ISO 2631-1 weighting filter. This filter apparently has a significant weighting factor in these frequency ranges where the look-up table does not resemble the physical damper.

The main conclusion concerning the half motorbike application is the fact that the weighted

sprung mass acceleration predicted by the physical damper model differs up to 13 % in comparison to the commonly used look-up table damping model on an ISO 2631-1 D-class poor road. Taking into account that humans can sense differences of approximately 5 % weighted sprung acceleration, makes the implementation of a physical damper model essential when predicting comfort levels.

To the knowledge of the author, this study is the first to perform vehicle simulations by implementing a physical damper model of a hydraulic mono-tube damper to predict damping forces. Furthermore, it is the first to compare simulation results with this physical damper model to simulation results with conventional used damper models such as a linear and look-up damper model.

7.2 Recommendations

Friction
The physical damper model is capable of predicting damping force within 7% accuracy for excitation frequencies in excess of 0.5 Hz. Friction forces tend to dominate damping forces below 0.5 Hz, therefore yielding larger prediction errors below 0.5 Hz. To enhance model accuracy in this lower frequency range it is recommended to include a friction model.

Force oscillations
Measurements show oscillating damper force behaviour that is not captured by the physical damper model. Some research has been conducted in the origin of these oscillations. The water hammer effect described by Joukouwky's equation and cylinder vibrations are investigated, but natural frequencies of these phenomena do not match the frequency observed from the measurement data. The exact cause for these oscillations remain unclear and may possibly be found in a vibrational mode of the damper test rig.

Large shim stack deflections
The physical damper model assumes linearised equations to predict bending of the shim stack valves. These equations are proved to be valid for deflections smaller than the shim thickness. Most dampers that are used by TFX Suspension Technology have stacks that never open more than one time this plate thickness, making these equations suitable to predict stack opening. However, it might be of interest to study large stack deflections and its resulting damping behaviour. This eventually might lead to extension of the shim stack equations to a non-linear model.

Numerical integration algorithm
The equations that are used to calculate the damping force describe a stiff system of non-linear ordinary differential equations. This study uses a fixed stepsize fourth order Runge-Kutta integration algorithm to integrate the system with respect to time. Although the solution converges for a small stepsize, it is recommended to introduce a variable stepsize solver to reduce calculation time. Furthermore, the half motorbike model that incorporates the physical damper model is a multi-timescale problem, thus having two time constants. The first time constant corresponds to the equations that describe the motion of the half motorbike model, the second time constant corresponds to the model that calculates the damper force of the physical damper model. This study uses a small stepsize to solve the whole system, however, a so-called time-subcycling method can be incorporated to reduce calculation time.

Modelling other damper types
All relevant equations that describe pressure drops and flow of fluid through valves and orifices are gathered in this thesis. Although one of the most simple type of dampers is used as

a baseline in modelling damping responses, this thesis can also be used as a starting point in modelling all types of dampers, such as mono-tube dampers that include free-floating separating pistons to separate gas and oil, or dual-tube dampers that have extra valve assemblies to control the flow of oil.

Optimum damper characteristics

The process of damper behaviour optimization is supported by test rigs that qualitatively measure the performance of a damper. A test engineer will always subjectively rate the performance of a damper on a track. To enhance the process of designing optimal damper characteristics, it is recommended to conduct research into the relation between the subjective ratings of a test engineer and the corresponding objective optimal damper.

Half motorbike model validation

A half motorbike simulation model has been derived to compare the physical damper model to conventional used damper models such as a linear- and look-up table damper model. Although quarter car models are known to be representative to calculate vertical accelerations of real cars, it is not known whether the half motorbike model is capable of accurately representing the vertical dynamic behaviour of real motorbikes. To validate the use of the half motorbike model it is recommended to do measurements on a motorbike and validate these measurements on a half motorbike test setup. Moreover, the half motorbike model is a simplification of a full motorbike, implying that it does not cover all dynamic aspects such as roll, pitch and yaw behaviour. Contributions of the front suspension to vertical dynamics are not taken into account, a more detailed model should incorporate all of these dynamics.

Car and truck application

The main conclusion concerning the half motorbike application is the fact that implementing a physical damper model is essential when predicting comfort levels, especially on ISO 2631-1 D-class poor roads. This conclusion is drawn from half motorbike simulations, but should be extended to car and truck applications. It is recommended to implement a physical damper model of a car and truck damper in a simulation application and compare it to linear and look-up table damper models.

Bibliography

[1] N.S.L. Feijen. Conversion of a tensile test bench into a fully functional shock absorber test rig. Master's thesis, Eindhoven University of Technology, 2015.

[2] TFX Suspension Technology. http://www.tfxsuspension.com. Weert, The Netherlands.

[3] STORM Eindhoven. https://www.storm-eindhoven.com. Online, 2016.

[4] J.C. Dixon. *The shock absorber handbook*. John Wiley & Sons Ltd, Second edition, 2007.

[5] Roehrig Engineering. www.roehrigengineering.com. Online, 2016.

[6] L. Segel and H.H. Lang. The mechanics of automotive hydraulic dampers at high stroking frequencies. *Vehicle System Dynamics*, 10(2-3):82–85, 1981.

[7] K. Reybrouck. A non linear parametric model of an automotive shock absorber. *SAE Technical Paper 940869*, 1994.

[8] S.W.R. Duym. Simulation tools, modelling and identification, for an automotive shock absorber in the context of vehicle dynamics. *Vehicle System Dynamics*, 33(4):261–285, 2000.

[9] A.L. Audenino and G. Belingardi. Modelling the dynamic behaviour of a motorcycle damper. *Proceedings of the Institution of Mechanical Engineers, part D: Journal of Automobile Engineering*, 209(4):249–262, 1995.

[10] M.S. Talbott and J. Starkey. An experimentally validated physical model of a high-performance mono-tube damper. *SAE Technical Paper 2002-01-3337*, 2002.

[11] U. Ferdek and J. Luczko. Modeling and analysis of a twin-tube hydraulic shock absorber. *Journal of Theoretical and Applied Mechanics*, 50(2):627–638, 2012.

[12] G. Belingardi and P. Campanile. Improvement of the shock absorber dynamic simulation by the restoring force mapping method. *Proceedings of the 15th International Seminar on Modal Analysis*, pages 441–454, 1990.

[13] R. Karadayi and G.Y. Masada. A nonlinear shock absorber model. *Proceedings of the Symposium on Simulation and Control of Ground Vehicles and Transportation Systems*, pages 149–165, 1986.

[14] F.H. Besinger, D. Cebon and D.J. Cole. Damper models for heavy vehicle ride dynamics. *Vehicle System Dynamics*, 24(1):35–64, 1995.

[15] V. Pracny, M. Meywerk and A. Lion. Hybrid neural network model for history-dependent automotive shock absorbers. *Vehicle System Dynamics*, 45(1):1–14, 2007.

[16] P. Sutter. Hydraulikschema der Prüfmaschine 1852. Technical report, ZWICK/REL Materialprüfsysteme AG, 1993.

[17] D.A. Winter. *Biomechanics and motor control of human movement.* John Wiley & Sons, 2009.

[18] N.J. Wismer. Time domain averaging combined with order tracking. Technical report, Bruel & Kjær (nd), 1997.

[19] H.E. Merrit. *Hydraulic control systems.* John Wiley & Sons, 1967.

[20] S.R. Turns. *Thermodynamics: concepts and applications.* Cambridge University Press, 2006.

[21] Y. Nakayama and R.F. Boucher. *Introduction to fluid mechanics.* Arnold, London, 1999.

[22] W. Janna. *Design of fluid thermal systems.* Cengage Learning, 2014.

[23] B.P.M. van Esch and H.P. van Kemenade. *Procestechnische constructies.* Eindhoven University of Technology, 2010.

[24] W.C. Young and R.G. Budynas. *Roark's Formulas for Stress and Strain.* McGraw-Hill, Seventh edition, 2002.

[25] M.T. Heath. *Scientific computing - an introductory survey.* McGraw-Hill, Second edition, 2002.

[26] A. Bergant, A.R. Simpson and A.S. Tijsseling. Water hammer with column separation: A historical review. *Journal of Fluids and Structures*, 22(2):135–171, 2006.

[27] A.W. Leissa and S. Jinyoung. Accurate vibration frequencies of circular cylinders from three-dimensional analysis. *The Journal of the Acoustical Society of America*, 98(4):2136–2141, 1995.

[28] BMW Motorrad International. *BMW R 1200 GS Adventure.* www.bmw-motorrad.com. Online, 2016.

[29] B. de Kraker. *Mechanical Vibrations.* Shaker Publishing, 2009.

[30] I.J.M. Besselink. *Vehicle Dynamics 4AT00, notes on Dynamic Systems, transfer functions and signal analysis.* Eindhoven University of Technology, 2015.

[31] ISO. ISO 8608:1995 Mechanical vibration - Road surface profiles - Reporting of measured data. Technical report, International Organization for Standardization, 1995.

[32] ISO. ISO 2631-1:1997 Mechanical vibration and shock - Evaluation of human exposure to whole body vibration. Technical report, International Organization for Standardization, 1997.

[33] L. Zuo, S.A. Nayfeh. Low order continuous-time filters for approximation of the ISO 2631-1 human vibration sensitivity weightings. *Journal of sound and vibration*, 265(2):459–465, 2003.

Appendix A

State equation for liquid-gas mixtures

Unlike gasses, the equation of state of a mixture can not be directly derived from physical laws. This appendix aims to relate changes in pressure to changes in mixture density. The density of a liquid is introduced first, the density of a liquid-gas mixture is derived afterwards.

Liquid density

Mass density of a liquid is known to be related to pressure and temperature: $\rho_l = \rho_l\,(p, T)$. Changes in liquid density as function of pressure and temperature are known to be small, which allows for approximating liquid density with a first order Taylor series expansion [19]:

$$\rho_l\,(p, T) = \rho_{l,0} + \left(\frac{\partial \rho_l}{\partial p}\right)_T (p - p_0) + \left(\frac{\partial \rho_l}{\partial T}\right)_p (T - T_0) \tag{A.1}$$

Definition of the isobaric- and isothermal bulk modulus of the liquid, denoted with α_l and β_l respectively, as:

$$\alpha_l = -\frac{1}{\rho_{l,0}} \left(\frac{\partial \rho_l}{\partial T}\right)_p = \frac{1}{V_0} \left(\frac{\partial V_0}{\partial T}\right)_p \tag{A.2}$$

$$\beta_l = \rho_{l,0} \left(\frac{\partial p}{\partial \rho_l}\right)_T = -V_0 \left(\frac{\partial p}{\partial V}\right)_T \tag{A.3}$$

yields an expression to approximate mass density of liquids:

$$\rho_l\,(p, T) = \rho_{l,0} \left[1 + \frac{1}{\beta_l} (p - p_0) - \alpha_l (T - T_0)\right] \tag{A.4}$$

Equation (A.4) demonstrates that an increase in pressure yields increasing liquid density. In contradiction, an increase in temperature yields decreasing mass density due to liquid expansion. This study assumes isothermal behaviour of the mono-tube damper, thus being constant in temperature, (A.4) therefore reduces to $\rho_l = \rho_l\,(p)$:

$$\rho_l\,(p) = \rho_{l,0} \left[1 + \beta_l^{-1} (p - p_0)\right] \tag{A.5}$$

69

The isothermal bulk modulus β_l is a property of the liquid and is provided by the supplier of the oil.

Nitrogen gas density

The density of nitrogen gas at atmospheric pressure is the fraction of nitrogen mass and -volume: $\rho_{gas,0} = \frac{m_{gas,0}}{V_{gas,0}}$. The mass of nitrogen gas in the system is constant, hence $m_{gas} = m_{gas,0}$. The density of the gas at some pressure p yields:

$$\rho_{gas} = \frac{m_{gas}}{V_{gas}} = \frac{m_{gas,0}}{V_{gas}} \tag{A.6}$$

Volume of the nitrogen gas V_{gas} decreases as pressure p increases and are related by a polytropic relation:

$$p_0 V_{gas,0}^{\kappa} = p V_{gas}^{\kappa}$$

$$V_{gas} = V_{gas,0} \left(\frac{p_0}{p} \right)^{\frac{1}{\kappa}} \tag{A.7}$$

Substituting (A.7) in (A.6) yields an equation that describes mass density of nitrogen gas as function of pressure:

$$
\begin{aligned}
\rho_{gas} &= \frac{m_{gas,0}}{V_{gas}} \\
&= \frac{m_{gas,0}}{V_{gas,0} \left(\frac{p_0}{p} \right)^{\frac{1}{\kappa}}} \\
&= \rho_{gas,0} \left(\frac{p}{p_0} \right)^{\frac{1}{\kappa}}
\end{aligned}
\tag{A.8}
$$

Mixture density

Density of a mixture is the fraction of mixture mass m_{mix} over mixture volume V_{mix}:

$$\rho_{mix} = \frac{m_{mix}}{V_{mix}} \tag{A.9}$$

The volume of the mixture is the sum of individual liquid volume V_l and gas volume V_{gas}:

$$V_{mix} = V_{gas} + V_l = \frac{m_{gas}}{\rho_{gas}} + \frac{m_l}{\rho_l} \tag{A.10}$$

with m_{gas} the mass of gas in the mixture and m_l the mass of the fluid in the mixture. Substituting (A.10) in (A.9) and introducing the mass fraction of gas in the mixture $f_m = \frac{m_{gas}}{m_{mix}}$ yields:

$$\frac{1}{\rho_{mix}} = \frac{f_m}{\rho_{gas}} + \frac{1 - f_m}{\rho_l} \tag{A.11}$$
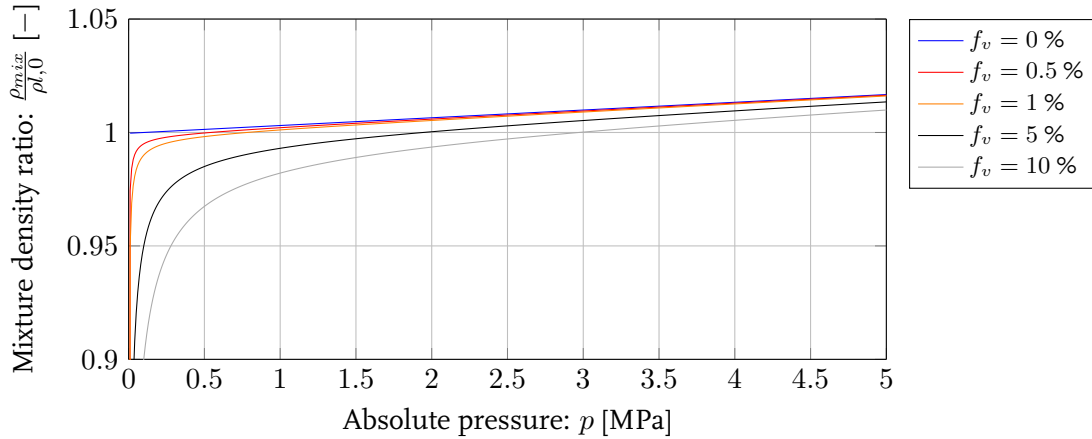
The relation between liquid density and pressure is provided by (A.5), (A.8) relates pressure to gas density. Substituting (A.5) and (A.8) in (A.11) yields a final expression that relates mixture density to mixture pressure:

$$\rho_{mix} = \left(\frac{f_m}{\rho_{gas,0} \left(\frac{p}{p_0} \right)^{\frac{1}{\kappa}}} + \frac{1 - f_m}{\rho_{l,0} \left[1 + \beta_l^{-1} (p - p_0) \right]} \right)^{-1} \tag{A.12}$$

Mass fraction f_m relates to volumetric fraction f_v by:

$$f_m = \frac{\rho_{gas} f_v}{\rho_{gas} f_v + \rho_l (1 - f_v)} \tag{A.13}$$

Figure A.1 shows the influences of different volumetric fractions of nitrogen gas dissolved in the hydraulic liquid at varying system pressure on mixture density. It shows the fraction of mixture density over de-aerated liquid density, i.e. the density of the hydraulic liquid at atmospheric pressure without nitrogen gas dissolved in it.

Figure A.1: Ratio of mixture density over liquid density ($\frac{\rho_{mix}}{\rho_{l,0}}$) for different fractions of nitrogen gas dissolved in the hydraulic liquid

As expected, a completely de-aerated oil ($f_v = 0$) yields a linear relation between liquid density and pressure, which is described by (A.5). The working pressure in TFX Suspension Technology's mono-tube damper is in the order of magnitude of ten bar (1 MPa). A small fraction of nitrogen dissolved in the liquid ($f_v = 0.5$ %) slightly decreases mixture density at this pressure. Larger fractions drastically lower the mixture density at this pressure. Mono-tube dampers that are not equipped with free-floating separation pistons to prevent oil and gas to mix are known to have volume fractions up to ten percent of gas dissolved in the hydraulic fluid. This is highly undesired to guarantee stable working of the shock absorber.

Effective bulk modulus

The effective bulk modulus β of a mixture is introduced in Section 4.3:

$$\beta_{mix} = \rho_{mix} \left(\frac{\partial p}{\partial \rho_{mix}} \right) \tag{A.14}$$

and relates the resistance of a substance to compression. An expression for the density of a liquid-gas mixture has been previously derived and is described by (A.12). Deriving this equation with respect to pressure p yields:

$$\frac{\partial \rho_{mix}}{\partial p} = \frac{\dfrac{f_m}{\kappa p \rho_{gas,0}\left(\frac{p}{p_0}\right)^{\frac{1}{\kappa}}} + \dfrac{\beta_l(1-f_m)}{\rho_{l,0}(\beta_l+(p-p_0))^2}}{\left(\dfrac{f_m}{\rho_{gas,0}\left(\frac{p}{p_0}\right)^{\frac{1}{\kappa}}} + \dfrac{(1-f_m)}{\rho_{l,0}\left(1+\beta_l^{-1}(p-p_0)\right)}\right)^2} \tag{A.15}$$

Substituting (A.12) and (A.15) in (A.14) yields a final expression for the effective bulk modulus of a liquid-gas mixture as function of pressure p and nitrogen mass fraction f_m:

$$\beta_{mix} = \rho_{mix}\left(\frac{\partial p}{\partial \rho_{mix}}\right) = \rho_{mix}\left(\frac{\partial \rho_{mix}}{\partial p}\right)^{-1}$$

$$= \frac{\dfrac{f_m}{\rho_{gas,0}\left(\frac{p}{p_0}\right)^{\frac{1}{\kappa}}} + \dfrac{1-f_m}{\rho_{l,0}\left(1+\beta_l^{-1}(p-p_0)\right)}}{\dfrac{f_m}{\kappa p \rho_{gas,0}\left(\frac{p}{p_0}\right)^{\frac{1}{\kappa}}} + \dfrac{\beta_l(1-f_m)}{\rho_{l,0}(\beta_l+(p-p_0))^2}} \tag{A.16}$$

Figure A.2 shows the influences of different volumetric fractions of nitrogen gas dissolved in the hydraulic liquid at varying system pressure. It shows the fraction of effective bulk modulus over de-aerated liquid bulk modulus, i.e. the bulk modulus of the hydraulic liquid without nitrogen dissolved in it. As expected, a completely de-aerated oil ($f_v = 0$) yields a constant effective bulk modulus which equals the bulk modulus of the liquid: $\beta_{mix} = \beta_l$. As stated previously, the working pressure in TFX Suspension Technology's mono-tube damper is in the order of magnitude of 1 MPa. A small fraction of nitrogen $f_v = 0.5$ % dissolved in the liquid will lower the effective bulk modulus with 17 % at this pressure. Larger fractions significantly lower the effective bulk modulus. Taking into account that volume fractions up to ten percent of gas can be dissolved in the liquid, shows that this significantly affects the bulk modulus at 10 MPa.
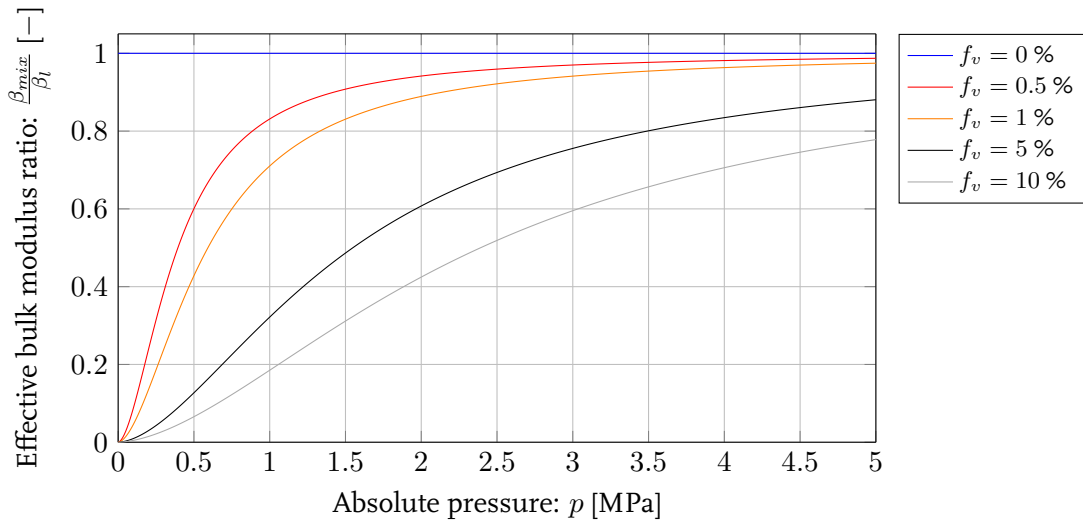

Figure A.2: Ratio of effective bulk modulus over the bulk modulus of the liquid ($\frac{\beta}{\beta_l}$) for different fractions of nitrogen gas dissolved in the hydraulic liquid

Appendix B

Shim stack model

The flow trough the piston assembly is controlled by the shim stack, allowing oil flow in one direction and blocking the oil to flow in the opposite direction. The shim stack is composed by stacking a number of small circular plates, known as shims, on top of each other. Varying the thickness and outer radii of the shims allows adjusting the stack opening behaviour, which in its turn controls flow of oil through the piston orifices. In order to model the oil flow through the piston, predictions should be done regarding the opening of the shim stack. A model that predicts opening of the shim stack was first derived by Talbott and Starkey [10] and is briefly summarized in this section. The model uses linearised equations for bending of circular plates of uniform thickness as derived by Young and Budynas [24]. These equations have been proven to be valid for tip deflections smaller than the plate thickness. The principle of superposition is allowed since the equations in Young and Budynas [24] are linearised.

The shim stack and its nomenclature are schematically presented in Figure B.1. The stack consists of 'k' shims, a single shim i is a circular plate with thickness t_i and outer radius r_i. All shims are clamped at radius b. The shim laying directly on top of the piston is shim k; the shim which is the furthest away from the piston is shim number 1. Tip deflection of shim i is indicated with y_i. Two consecutive shims contact each other at the outer radius of the shim with the smallest radius, resulting in a line load contact reaction force R_i at this outer radius. As the two consecutive shims contact each other at the outer radius of the shim with the smallest diameter, tip deflection y_i of one shim is equal to the intermediate deflection z_{i+1} of its subsequent shim:

$$y_i = z_{i+1} \tag{B.1}$$

Notation $y_i(R_i)$ means tip deflection of shim i resulting from line contact force R_i.

First shim:
The first shim only experiences one line load contact R_1. This line load contact results in tip deflection y_1. The first shim contacts shim 2 at radius r_1. z_2 is the deformation of shim 2 at this contact point and equals y_1:

$$\begin{aligned} y_1 &= y_1(R_1) \\ &= z_2(R_1) + z_2(R_2) \end{aligned} \tag{B.2}$$

Note that z_2 results from line load contacts R_1 and R_2.

Intermediate shims:
All intermediate shims ($i = 2, ..., k-1$) experience two line load contact forces R_i and R_{i-1}. These line load contact forces result in tip deflections y_i. Shim i contacts shim $i+1$ at radius r_i. z_{i+1} is the deformation of shim $i+1$ at radius r_i and equals y_i:

$$
\begin{aligned}
y_i &= y_i(R_i) + y_i(R_{i-1}) \\
&= z_{i+1}(R_i) + z_{i+1}(R_{i+1})
\end{aligned}
\tag{B.3}
$$

Bottom shim:
The bottom shim experiences a line load contact from the second-last shim and a distributed pressure Δp acting from radius r_p to outer radius r_k from below the piston. The intermediate deflection z_k at radius r_{k-1} is equal to tip deflection y_{k-1}:

$$y_k = y_k(\Delta p) + y_k(R_{k-1}) \tag{B.4}$$

$$z_k = z_k(\Delta p) + z_k(R_{k-1}) \tag{B.5}$$

For exact formulas of (B.2) to (B.5) is referred to pages 463 and 467 of Young and Budynas [24].

The previously described system results in a system of $3(k-2) + 4$ equations in which individual shim thickness and outer radii can be varied. An example of shim stack mid-plane deformations predicted by the previously described system is depicted in Figure B.2. Tip deflection of the bottom shim linearly relates to the pressure difference over the stack of shims:

$$y = \frac{\Delta p a_v}{k_s} \tag{B.6}$$

with k_s the stiffness of the shim stack and a_v the summed cross-sectional area of valve flow orifices. The latter is used to predict throttle area for valve flow (4.40).
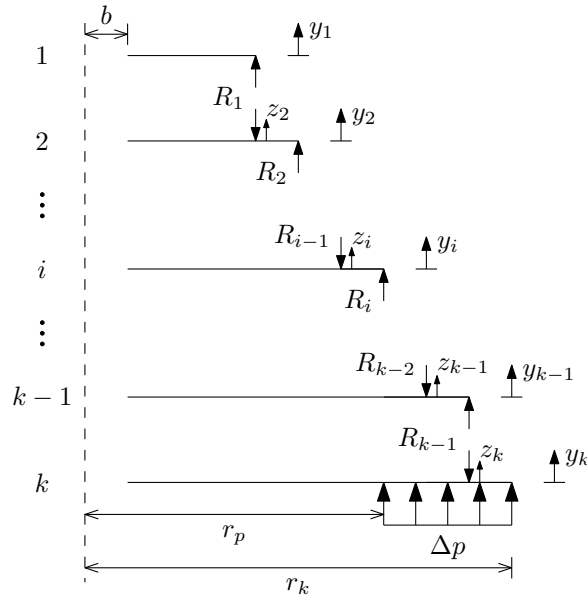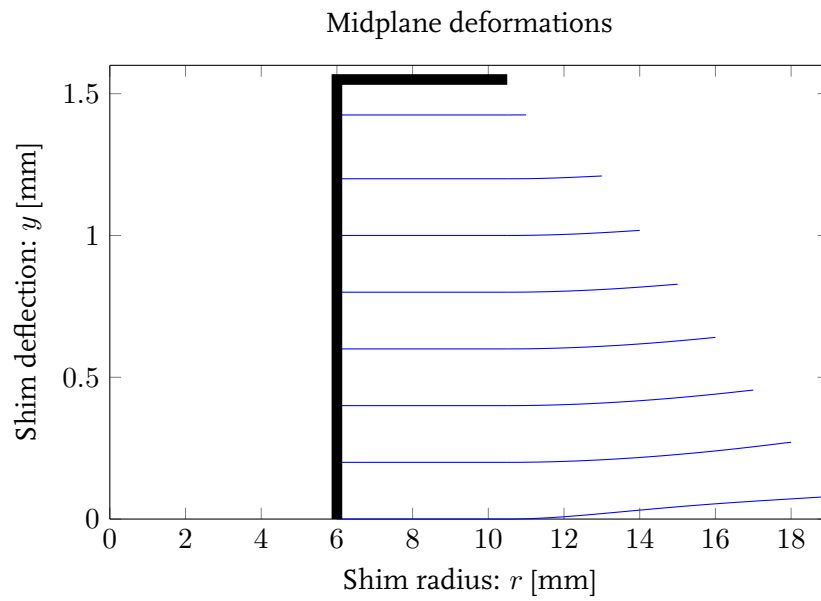

Figure B.1: Nomenclature for deriving shim stack deformations

Figure B.2: Example of a deformed shim stack composed from 8 shims and a resultant pressure difference $\Delta P = 1$ bar, the thick black line indicates the inner- and clamping radii of the shims

Mono-tube Ordinary Differential Equation

The system of non-linear differential equations that calculates the damping response of the mono-tube damper is described by (4.22) and (4.23). These two equations can be written as a Ordinary Differential Equation (ODE), yielding:

$$\dot{\mathbf{y}} = g(t, \mathbf{y}) \tag{C.1}$$

with $\mathbf{y} = \begin{bmatrix} p_r & p_c \end{bmatrix}^T$. ODE function $g(t, \mathbf{y})$ is evaluated by the Runge-Kutta numerical integration algorithm described in Section 5.1. The implementation of the ODE function is provided in this appendix. Function $g(t, \mathbf{y})$ uses the current pressures in the rebound- and compression chamber p_r and p_c, and the position $x(t)$ and velocity $\dot{x}(t)$ of the piston rod: $\dot{\mathbf{y}} = g(x(t), \dot{x}(t), \mathbf{y})$. The algorithm that describes the non-autonomous function $g(x(t), \dot{x}(t), \mathbf{y})$ is provided in Algorithm 1:

Algorithm 1 Differential equations function $\dot{\mathbf{y}} = g(x(t), \dot{x}(t), \mathbf{y})$

1: **function** $\dot{\mathbf{y}} = g(x(t), \dot{x}(t), \mathbf{y})$ $\triangleright\ \mathbf{y} = \begin{bmatrix} p_r & p_c \end{bmatrix}$

2:     $V_r = A_r x$ $\triangleright$ (4.16)

3:     $V_{gas} = V_{gas,0} \left(\dfrac{p_{gas,0}}{p_c} \right)^{\frac{1}{\kappa}}$ $\triangleright$ (4.20)

4:     $V_c = V_0 - V_r - V_{gas} - A_{rod} x$ $\triangleright$ (4.18)

5:     $\rho_r = \left(\dfrac{f_m}{\rho_{gas,0} \left(\frac{p_r}{p_0} \right)^{\frac{1}{\kappa}}} + \dfrac{1 - f_m}{\rho_{l,0} \left[1 + \beta_l^{-1}(p_r - p_0) \right]} \right)^{-1}$ $\triangleright$ (4.24)

6:     $\rho_c = \left(\dfrac{f_m}{\rho_{gas,0} \left(\frac{p_c}{p_0} \right)^{\frac{1}{\kappa}}} + \dfrac{1 - f_m}{\rho_{l,0} \left[1 + \beta_l^{-1}(p_c - p_0) \right]} \right)^{-1}$ $\triangleright$ (4.24)

7:     $\beta_r = \dfrac{\rho_r^{-1}}{\dfrac{f_m}{\kappa p_r \rho_{gas,0} \left(\frac{p_r}{p_0} \right)^{\frac{1}{\kappa}}} + \dfrac{\beta_l(1 - f_m)}{\rho_{l,0}[\beta_l + (p_r - p_0)]^2}}$ $\triangleright$ (4.27)

Algorithm continues on next page.

8:     $\beta_c = \dfrac{\rho_c^{-1}}{\dfrac{f_m}{\kappa p_c \rho_{gas,0}\left(\frac{p_c}{p_0}\right)^{\frac{1}{\kappa}}} + \dfrac{\beta_l(1-f_m)}{\rho_{l,0}[\beta_l+(p_c-p_0)]^2}}$ ▷ (4.27)

9:     **if** $p_c > p_r$ **then**   ▷ Compression stroke

10:      $y = \dfrac{(p_c-p_r)a_{v,c}}{k_{s,c}}$ ▷ (B.6)

11:      $a_{t,v,c} = \frac{2}{3}\pi D_v y$ ▷ (4.40)

12:      $\sum K = 12.35 + 0.138\left(\dfrac{a_{v,c}}{a_{t,v,c}}\right)^2$

13:      $Q_{v,c} = \dfrac{-1.48\frac{64a_{v,c}\mu}{\rho_c D_{wp}}\frac{L_{wp}}{D_{wp}}+\sqrt{\left(1.48\frac{64a_{v,c}\mu}{\rho_c D_{wp}}\frac{L_{wp}}{D_{wp}}\right)^2+4a_{v,c}^2\frac{2}{\rho_c}\sum K(p_c-p_r)}}{2\sum K}$ ▷ (4.37)

14:      **if** $n_c > 0$ **then**

15:        $\sum K = 2.646 + 0.485\left(\dfrac{a_b}{a_{t,b}}\right)^2$

16:        $Q_{b,c} = \dfrac{-8.92\frac{64a_b\mu}{\rho_c D_b}\frac{L_b}{D_b}+\sqrt{\left(8.92\frac{64a_b\mu}{\rho_c D_b}\frac{L_b}{D_b}\right)^2+4a_b^2\frac{2}{\rho_c}\sum K(p_c-p_r)}}{2\sum K}$ ▷ (4.34)

17:      **else**

18:        $Q_{b,c} = 0$

19:      **end if**

20:      $Q_{rc} = 0$ ▷ (4.28)

21:      $Q_{cr} = Q_{v,c} + Q_{b,c}$ ▷ (4.28)

22:     **else if** $p_r > p_c$ **then**   ▷ Rebound stroke

23:      $y = \dfrac{(p_r-p_c)a_{v,r}}{k_{s,r}}$ ▷ (B.6)

24:      $a_{t,v,r} = \frac{1}{3}\pi D_v y$ ▷ (4.40)

25:      $\sum K = 3.01 + 1.56\cdot 10^{-3}\left(\dfrac{a_{v,r}}{a_{t,v,r}}\right)^2$

26:      $Q_{v,r} = \dfrac{-1.11\frac{64a_{v,r}\mu}{\rho_r D_{wp}}\frac{L_{wp}}{D_{wp}}+\sqrt{\left(1.11\frac{64a_{v,r}\mu}{\rho_r D_{wp}}\frac{L_{wp}}{D_{wp}}\right)^2+4a_{v,r}^2\frac{2}{\rho_r}\sum K(p_r-p_c)}}{2\sum K}$ ▷ (4.37)

27:      **if** $n_c > 0$ **then**

28:        $\sum K = 3.153 + 0.436\left(\dfrac{a_b}{a_{t,b}}\right)^2$

29:        $Q_{b,r} = \dfrac{-4.64\frac{64a_b\mu}{\rho_r D_b}\frac{L_b}{D_b}+\sqrt{\left(4.64\frac{64a_b\mu}{\rho_r D_b}\frac{L_b}{D_b}\right)^2+4a_b^2\frac{2}{\rho_r}\sum K(p_r-p_c)}}{2\sum K}$ ▷ (4.34)

30:      **else**

31:        $Q_{b,r} = 0$

32:      **end if**

33:      $Q_{rc} = Q_{v,r} + Q_{b,r}$ ▷ (4.28)

34:      $Q_{cr} = 0$ ▷ (4.28)

35:     **else**

36:      $Q_{rc} = 0$ ▷ (4.28)

37:      $Q_{cr} = 0$ ▷ (4.28)

38:     **end if**

39:     $\dot{m}_c = \rho_r Q_{rc} - \rho_c Q_{cr}$ ▷ (4.10)

40:     $\dot{m}_r = \rho_c Q_{cr} - \rho_r Q_{rc}$ ▷ (4.10)

41:     $\dot{p}_r = \dfrac{\beta_r}{V_r}\left[\dfrac{\dot{m}_r}{\rho_r} - A_r \dot{x}\right]$ ▷ (4.22)

42:     $\dot{p}_c = \dfrac{\kappa\beta_c p_c^{\frac{1}{\kappa}+1}}{\kappa V_c p_c^{\frac{1}{\kappa}+1}+\beta_c V_{gas,0}p_{gas,0}^{\frac{1}{\kappa}}}\left[\dfrac{\dot{m}_c}{\rho_c} + A_c \dot{x}\right]$ ▷ (4.23)

43:     **return** $\dot{\mathbf{y}} = \begin{bmatrix} \dot{p}_r & \dot{p}_c \end{bmatrix}$

44: **end function**

Evaluating the latter function with a fourth order Runge-Kutta scheme yields the pressures p_r and p_c, the damper force is calculated from:

$$F_d = p_r A_r - p_c A_c + p_0 A_{rod} + m_t g$$

Appendix D

Half motorbike model verification

In Chapter 6 a half motorbike model is derived to simulate the vertical dynamic behaviour of a motorbike. The system of non-linear differential equations that predicts the vertical dynamics are derived from Lagrange's equation of motion and are described by (6.16) and (6.17). A *MATLAB SimMechanics*-model as visualized in Figure D.1 has been created to validate these equations. The unsprung mass is visualized in yellow, the swing-arm and sprung mass are depicted in red and blue respectively. Road height is depicted in black and can be prescribed. A step input of 50 mm is used to validate the model. The results from the *SimMechanics*-model are depicted in black in Figure D.2, results from the Lagrange dynamics are depicted in yellow. The Variance Account For (VAF) is a measure to quantify the difference between two signals and is defined as:

$$\text{VAF} = \left(1 - \frac{\text{var}\,(y - \hat{y})}{\text{var}\,(y)}\right) 100\% \tag{D.1}$$

with y in this case the output of the *SimMechanics* model, and $\hat{y}$ the output of the Lagrange equations of motion. Applying (D.1) on the sprung mass acceleration $\ddot{z}_s$ yields $\text{VAF}_{\ddot{z}_s} = 99.94\%$, from which is concluded that motions predicted by the Lagrange dynamics resemble the motions predicted by the *SimMechanics* model.
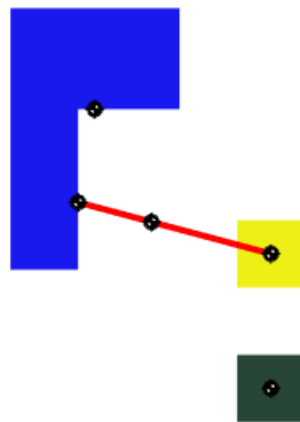
Figure D.1: MATLAB's SimMechanics visualization of the half motorcycle model with the sprung mass in blue, unsprung mass in yellow, road height in black and swing-arm in red. Tire spring and linear spring and damper are not visualized
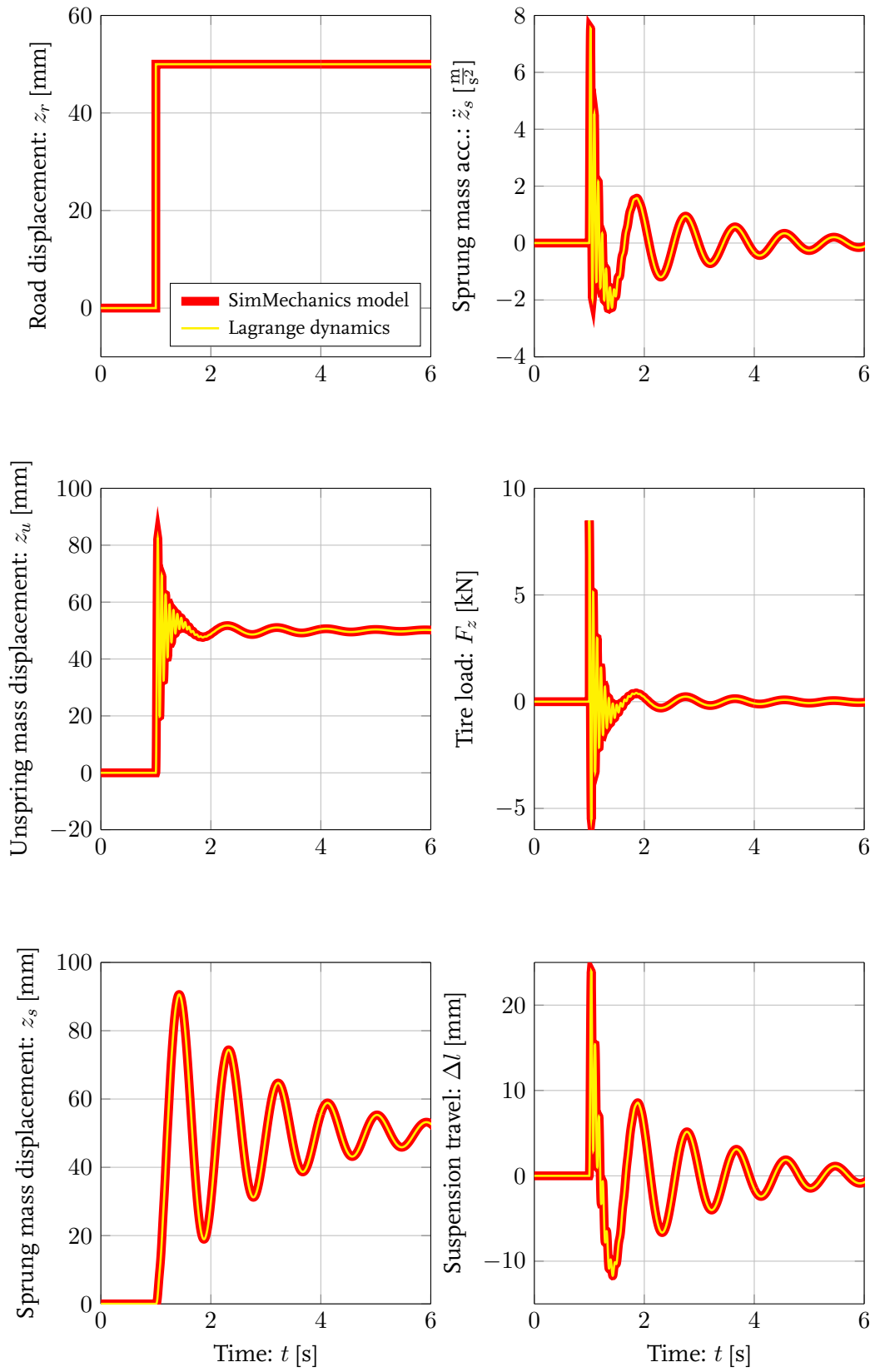
Figure D.2: Results of the half motorbike model predicted with the SimMechanics model and Equations of Motion derived from Lagrange dynamics

Appendix E

Damper dimensions

This appendix provides confidential information concerning dimensions of TFX Suspension Technology's mono-tube damper.

Shim stack compositions

Table E.1: Baseline shim stack composition $k_{s,c} = 0.848 \cdot 10^6$ [N/m] and $k_{s,r} = 2.781 \cdot 10^6$ [N/m]

Compression		Rebound	
Radius r_i [mm]	Thickness t_i [mm]	Radius r_i [mm]	Thickness t_i [mm]

This table has been intentionally left blank, data available upon request
Please contact: J. de Blok   `J.d.Blok@student.tue.nl`
                dr.ir. I.J.M. Besselink   `I.J.M.Besselink@tue.nl`

Table E.2: Shim stack composition to check model accuracy $k_{s,c} = 2.331 \cdot 10^6$ [N/m] and $k_{s,r} = 1.765 \cdot 10^6$ [N/m]

Compression		Rebound	
Radius r_i [mm]	Thickness t_i [mm]	Radius r_i [mm]	Thickness t_i [mm]

This table has been intentionally left blank, data available upon request
Please contact: J. de Blok   `J.d.Blok@student.tue.nl`
                dr.ir. I.J.M. Besselink   `I.J.M.Besselink@tue.nl`

Mono-tube damper geometries

Table E.3: Technical and geometric specifications of TFX Suspension Technology's mono-tube damper

Description	Parameter	Value	Unit
Compression chamber diameter	D_c		[mm]
Piston rod diameter	D_{rod}		[mm]
Piston orifice diameter	D_{wp}		[mm]
Bleed orifice diameter	D_b		[mm]
Damper height	L_0		[mm]
Piston height	L_{wp}		[mm]
Bleed orifice length	L_b		[mm]
Piston assembly mass	m_{wp}		[kg]
Mono-tube shell mass	m_t		[kg]
Maximum damper stroke	x_{max}		[mm]
Hydraulic fluid density (p_0)	$\rho_{l,0}$		[kg/m^3]
Bulk modulus hydraulic fluid	β_l		[MPa]
Dynamic viscosity	μ		[Ns/m^2]
Nitrogen gas density (p_0)	$\rho_{gas,0}$		[kg/m^3]
Nitrogen gas polytropic coefficient	κ		[−]
Absolute gas chamber pre-load pressure	$p_{gas,0}$		[bar]
Initial gas chamber height	$L_{gas,0}$		[mm]
Nitrogen volumetric fraction (p_0)	f_v		[%]
Nitrogen mass fraction	f_m		[%]
Bleed needle tip angle	θ		[deg]
Bleed needle pitch	P		[mm]
Bleed needle setting min-max	n_c		[−]

This column has been intentionally left blank (Value column)

Dependent variables

$$A_c = \pi \frac{D_c^2}{4}$$

$$A_{rod} = \pi \frac{D_{rod}^2}{4}$$

$$A_{gas} = A_c$$

$$A_r = A_c - A_{rod}$$

$$V_0 = A_c \left(L_0 - L_{wp} \right)$$

$$V_{gas,0} = L_{gas,0} A_{gas}$$

$$a_{v,c} = 6\pi \frac{D_{wp}^2}{4}$$

$$a_{v,r} = 3\pi \frac{D_{wp}^2}{4}$$

$$a_b = \pi \frac{D_b^2}{4}$$

$$z = \frac{n_c}{12} P$$

$$a_{t,b} = \pi \left(D_b z \tan \frac{\theta}{2} - z^2 \tan^2 \frac{\theta}{2} \right)$$

$$D_v = - \quad \text{[mm] rebound}$$
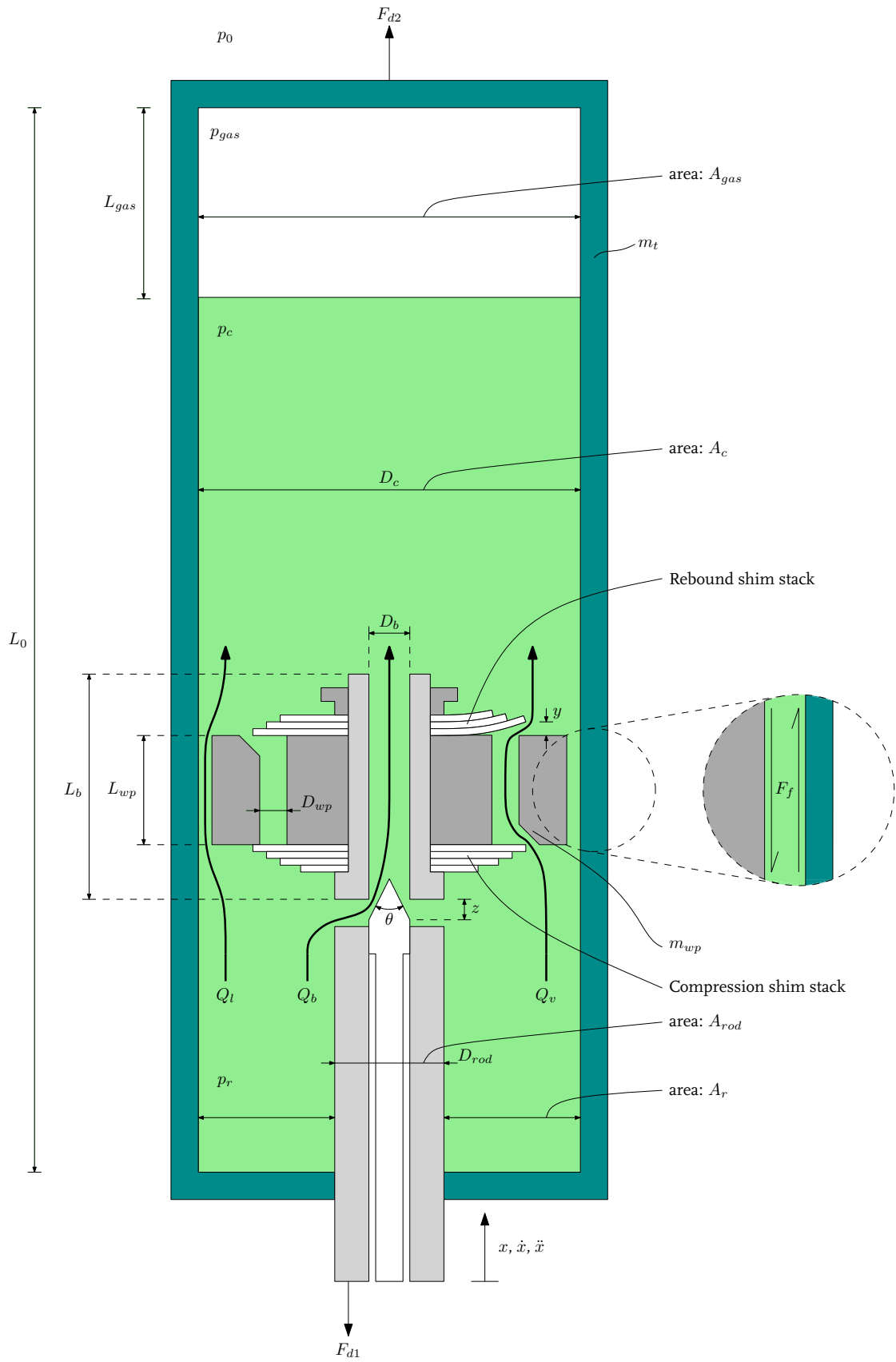
$$D_v = - \quad \text{[mm] compression}$$

Figure E.1: Schematic representation of the mono-tube damper. Rebound motion opens the rebound shim stack